Master Thesis

Simulating Open System Dynamics in the Spin-Boson Model on Quantum Computers

Simulation dissipativer Effekte im Spin-Boson Model auf Quanten Computern

Andreas Burger

Faculty of Physics
Ludwig-Maximilians-Universität München

Center for Quantum Technologies
National University Singapore

Science, Mathematics and Technology Cluster
Singapore University of Technology and Design

A Note of Thanks

Contents

List of Figures

Chapter 1

Introduction

1.1 Quantum Computing and Simulating Quantum Systems

Since the beginning of quantum computing, numerous applications have been proposed, but few algorithms proving a speedup over classical computers have emerged. The most prominent exceptions being the factoring of primes using inverse quantum Fourier transform (IQFT) by Shor [1], and Grover's search [2]. As both Shor's and Grover's algorithms rely on high-fidelity qubits, they are likely to remain intractable in the near future. The Deutsch–Jozsa algorithm, while one of the first examples of an provably exponentially faster quantum algorithm, is practically of little use [3, 4].

Simulating quantum systems was the original motivation for quantum computers and still is believed one of the first applications, where an advantage will be demonstrated. It was proposed by Feynman and others in reaction to the fact that simulations of general Hamiltonians tend to grow exponentially with respect to the system size, making the problem intractable on classical computers [5]. It was then Lloyd who showed that a quantum computer can act as a universal quantum simulator, giving the first explicit quantum algorithm for simulating the dynamics of local Hamiltonians [6]. The Hamiltonian simulation problem is known to be BQP-complete [7], which makes general efficient classical algorithms for this problem unlikely, as it would imply that there is an efficient classical algorithm for any efficient quantum algorithm, and no quantum speedup exists. Offering an exponential advantage in memory and time over classical methods, simulating quantum dynamics remains as one of the major research directions of quantum computers.

In reality, results achieved on quantum computers are still a far cry off the performance of classical methods. State of the art techniques in simulating

quantum systems include Tensor Networks, with powerful routines like DMRG [8, 9] and time-evolution algorithms [10], which can handle large many-body systems of $10^3 - 10^4$ particles.

In the realm of quantum computing, multiple quantum systems have emerged as underlying platforms, inluding photonics, neutral atoms, trapped ions, quantum dots and nuclear spins (NMR) [11]. One of the most mature and widely available technologies are superconducting circuits based on transmon qubits [12, 13]. A transmon (transmission-line shunted plasma oscillation qubit) is designed as an anharmonic quantum oscillator, such that the distances in the energy spectrum vary and the transition between two states can be selectively addressed. Physically it is built as a charge qubit, consisting of two Josephson junctions shunted with an additional capacitor.

While superconducting quantum computers already have hundreds of qubits, and are expected to reach a thousand by the end of 2023, the problem of noise puts a limit on the number of operations which can be performed. For example, to reach 60 high-fidelity qubits with current error correction algorithms, one would require over one million physical qubits [14]. This has led to the term of the Noisy-Intermediate Scale Quantum (NISQ) era [15, 16], characterized by a limited number of qubits, short decoherence times and low gate fidelities.

To overcome the need of deep quantum circuits, variational hybrid quantum-classical algorithms (VQA) have received a lot of attention [17, 18, 19]. These techniques split the workload between a quantum and a classical processor, to evaluate different quantities such as eigenstates [17], general quantum approximate optimization algorithms [20], off-diagonal elements of matrices [21] and more [16]. Importantly, error-mitigations approaches have also been put forward [22, 23, 24]. Similar to Machine Learning, the quantum circuit takes on the role of the Neural Network, with the circuit parameters as weights. This is also reminiscent of Tensor Networks, as the Tensor Network and the quantum circuit alike are optimized to represent a wavefunction. In hybrid approaches the loss function is calculated on the circuit, but the weights are updated using a classical optimizer. In that way the quantum computer can be leveraged to reduce the memory requirements for the classical system and to speed up the evaluation of the loss function. However it remains unclear if hybrid methods can offer any advantage over purely classical systems, as optimizing the parameters to minimize the cost function has been proven to be NP-hard [25].

The promise of a quantum speedup in simulating quantum systems on a quantum computer, combined with the current limitations of NISQ devices, motivates to study the feasibility in simulating toy problems on the already available hardware. In this thesis we want to tackle open system dynamics in the spin-boson model, and ask what results we achieve on state-of-the-art

hardware and on possibly improved devices in the future. We explore different implementations and study the impact of system parameters on the simulation fidelity in various regimes.

1.2 The Open Spin-Boson Model

Most scientific work so far has focused on fermionic systems, due to the natural correspondence with the prevalent qubit-based quantum devices, which are themselves two-level systems. Yet simulation of vibrational modes or light-matter interaction necessitates the inclusion of bosonic degrees of freedom. One important class of models to be studied is that of spin-boson problems, where one or more spins is coupled to one or more Harmonic Oscillators. These models have rich many-body physics and can model a plethora of phenomena, like particles in an optical cavity (cavity QED), superconducting circuits (circuit QED), and the coupling between electron transfer and protein motion [26, 27, 28, 29, 30, 31].

Similarly the use of unitary quantum circuits has led to research centered around closed systems governed by a unitary evolution [32, 33, 34, 35]. In practice, open quantum systems are far more common, as quantum systems are ultimately never perfectly shielded and interact with their environments. Their ubiquity in nature opens up a range of applications, from investigating the effects of noise on quantum technologies, to quantum chemistry and biology, and quantum thermodynamics.

1.3 Previous Literature

In the past a number of experiments have successfully tackled fermion-boson interactions through analog quantum simulation. While analog quantum simulators are not universal, i.e. cannot implement any unitary, they can be tuned to model systems which are governed by the same underlying physics as the simulator itself. The bosonic modes are represented by a physical system like vibrational modes in trapped ions [36, 37, 38, 39, 40], quantum inductor-resistor-capacitor (LRC) oscillators in superconducting qubits [41], nuclear magnetic resonance [42] or optical chips [43, 44]. The studied fermion-boson interactions include closed fermion-boson systems, as well as open fermion systems coupled to a bosonic bath.

On universal, or digital, quantum simulators the aforementioned VQA has been applied to spin-boson [45, 46, 47] and open systems alike. Application of VQA to open systems include approaches based on imaginary time evolution [48, 49], stochastic Schrödinger equation [50], variational quantum eigensolver

(VQE) to reach steady states [51, 52], and the quantum assisted simulator (QAS) which does not rely on a classical-quantum feedback loop [53].

Simulations of open quantum systems entirely on digital quantum computers has primarily focused on simple two-level systems. The amplitude damping channel specifically has been implemented using a unitary dilation of the Kraus operators [54], uniformly controlled gates [55, 56], and through what is known as the amplitude damping circuit [57, 58]. Larger systems have been realised using linear combination of unitaries (LCU) [59, 60] and modified stochastic Schrödinger equation methods [61].

The most closely related works we want to highlight include the first simulation of the (closed) spin-boson model on a quantum computer [35], and using Trotterization with frequent resets to reproduce open system dynamics [62], both published earlier this year.

1.4   Structure of the Thesis

Our aim is to simulate open system dynamics in the spin-boson model on a digital quantum computer. The model consists of a Harmonic Oscillator, one or two spins, coupled to a dissipative channel. Key questions in particular are how the level of noise in the hardware and the parameters of the system affect the accuracy of the simulation.

We replicate this by mapping the bosonic mode to qubits, Trotterizing the unitary evolution, and modeling the dissipation via collisions with a resetted auxiliary qubit. We repeat the evolution of unitary-dissipation-reset to realize the desired open system dynamics. We run our experiments on one of IBM's quantum computers, and build reduced-noise-models to replicate future devices with improved hardware.

The thesis is organized as follows. We begin by defining the problem in Sec. 2. In Sec. 3 we present the central idea of our implementation and lay out central techniques used in the later sections.

We present our theoretical and experimental results in Sec. 4, 5, and 6. First we treat the unitary and non-unitary parts separately in Sec. 4 and Sec. 5, before combining them to simulate the full open spin-boson system in Sec. 6.

In Sec. 7 we study a variation of the closed spin-boson model, the Jaynes-Cummings Hamiltonian, which conserves the excitation number. This conservation law allows us to use post-selection as an error mitigation technique to increase the simulation fidelity.

The results are summarized in chapter 8. Parts of this thesis have been published in [63] and submitted to a peer-reviewed journal.

Chapter 2

The Open Spin-Boson Model

In this chapter we define the problem of the open spin-boson model.

2.1 Spin-Boson Hamiltonian

We consider N_S non-interacting spins coupled to a single harmonic oscillator, as well as to a bath, see Fig. 2.1. The closed system is described by the Hamiltonian

$$\hat{H}_{SB} = \hbar\omega\hat{a}^\dagger\hat{a} + \sum_{k=1}^{N_S} \left(\frac{1}{2}(h\hat{S}_k^z + \epsilon\hat{\sigma}_k^x) + \lambda\hat{\sigma}_k^x \left(\hat{a}^\dagger + \hat{a}\right) \right) \tag{2.1}$$

$\hat{a}^\dagger$ and $\hat{a}$ respectively create and destroy one excitation in the harmonic oscillator and $\hat{\sigma}_k^x$ and $\hat{\sigma}_k^z = -\hat{S}_k^z$ are Pauli operators acting on the spin(s). h is the local magnetic field in the $z-$direction while ϵ is a field in the $x-$direction. λ is the magnitude of the coupling between the spins and the harmonic oscillator with frequency ω.

The interaction term in Eq. (2.1)

$$\hat{H}_{SB}^I = \sum_{k=1}^{N_S} \lambda \ \hat{\sigma}_k^x \left(\hat{a}^\dagger + \hat{a}\right) \tag{2.2}$$

$$= \sum_{k=1}^{N_S} \lambda \ (\hat{\sigma}_k^+ + \hat{\sigma}_k^-) \left(\hat{a}^\dagger + \hat{a}\right) \tag{2.3}$$

is known as the quantum Rabi Hamiltonian [64, 65, 66]. It describes light-matter interaction in the ultra-strong and deep-strong regime, where the usual rotating wave approximation (RWA) breaks down. In this regime the atomic transition frequency ω_a and the field mode frequency ω_f are of similar magnitude as the coupling λ and the counter-rotating term can no longer be neglected
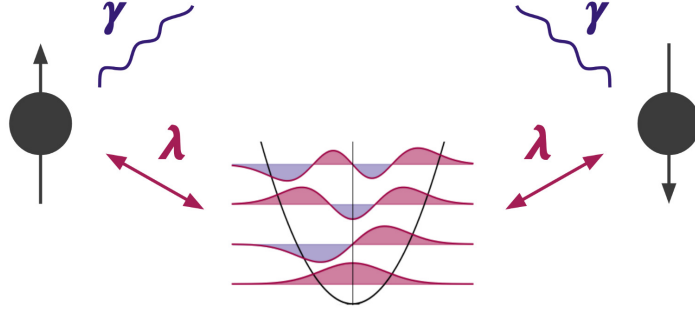
Figure 2.1: Depiction of model described by Eqs. (2.1, 2.4) for a number of spins $N_S = 2$. The two spin sites are coupled to one harmonic oscillator of frequency ω via coupling parameter λ. Each of the spins dissipates independently into the environment at a rate γ.

[67, 68, 27, 69]. Experimentally these regime shas been investigated in quantum systems such as circuit QED [70, 71, 72, 73, 74, 75], trapped ions [76], photonic systems [77] and semiconductors [78, 79].

2.2 Open System

The dissipative part of the dynamics is here described by a Gorini–Kossakowski–Sudarshan–Lindblad (GKSL) master equation, or Lindbladian, in it is diagonal form [80, 81]. The GKSL is a completely-positive and trace-preserving (CPTP) map, which governs the time-evolution of the system density matrix, giving an ensemble average of the dynamics. Also called a Markovian master equation, it is based on the Born-Markov approximation:

- Initially the system and environment are uncorrelated, s.t. the density matrix is a tensor product $\hat{\rho}_{SE}(t = 0) = \hat{\rho}_S \otimes \hat{\rho}_E$ (separability)

- The environment is much larger than the system and the interaction is weak, s.t. they remain separable at $t > 0$ (Born approximation)

- The environment is 'memory-less', i.e. the correlation functions decay much faster in the environment than in the system (Markov approximation)

- Fast oscillating terms in the interaction picture quickly average to zero and can be neglected (rotating wave or secular approximation)

The GKSL for our system of bosons and spins reads

$$\frac{d\hat{\rho}}{dt} = -\frac{i}{\hbar}\left[\hat{H}_{SB}, \hat{\rho}\right] + \gamma \sum_k \left(2\hat{L}_{S_i}\hat{\rho}\hat{L}_{S_i}^\dagger - \{\hat{L}_{S_i}^\dagger \hat{L}_{S_i}, \hat{\rho}\}\right) \qquad (2.4)$$

The Lindblad-, or jump-operators, act on the $k-$th spin $\hat{L}_{S_i} = |\downarrow\rangle\, k \,\langle\uparrow|$ with the decay rate γ, and describe what is known as the amplitude damping (AD) channel. $|\downarrow\rangle = |0\rangle$ represents the vacuum state, whereas $|\uparrow\rangle = |1\rangle$ represents the excited state of the spin.

Since $\hat{L}_{S_i}$ doesn't affect the harmonic oscillator, we can write the dissipation evolving the density matrix of each spin $\hat{\rho}_S$ individually

$$\frac{d\hat{\rho}_S}{dt} = \gamma\left[2\hat{\sigma}^-\hat{\rho}_S\hat{\sigma}^+ - \{\hat{\sigma}^+\hat{\sigma}^-, \hat{\rho}_S\}\right] \qquad (2.5)$$

The spin density matrix is given by

$$\hat{\rho}_S = \begin{pmatrix} p & q \\ q^* & 1-p \end{pmatrix} \qquad (2.6)$$

The entries p and q are often called 'populations' and 'coherences'.

Eq. (2.4) and Eq. (2.5) describe a setup where loss from imperfections in the cavity are neglectable but the spins exhibit broad emission lines. In these systems undesired decay transitions can include emission of frequencies which are suppressed by the cavity through destructive interference or absorption and thus are effectively lost [82, 83, 84].

In this thesis we consider the single-spin $N_S = 1$ and two-spin $N_S = 2$ case. In Sec. 4 and 5 we model the evolution of the dissipation (Eq. (2.5)) and under the Hamiltonian (Eq. (2.1)) separately, with the ultimate goal being to simulate the open system dynamics under the full GKSL in Eq. (2.4).

Where not marked explicitly, subfigures / subpanels are addressed by lowercase letters, ordered first left to right, then top to bottom.

Chapter 3

Method

3.1 The Idea: Trotterizing into Unitary and Non-Unitary Evolution

We start out by presenting the circuit structure of our approach to simulate the open spin-boson problem, as it will inform the individual steps going forward. We will lean on the concept of Trotterization, that is to approximate the total evolution by a repeated sequence of simpler evolutions. By making each repeated sequence represent a small time-slice, one partially makes up for the fact that the terms are generally non-commuting and should act simultaneously. We go into more detail on Trotterization in Sec. 3.2.2.

Applied to the open spin-boson problem, we split the total open system dynamics into evolutions of a unitary U, a dissipation D, and a reset $|0\rangle$. The proposed circuit layout is displayed in Fig. 3.1. The interaction with the environment is modeled by the repetition of a dissipation and a reset step, also referred to as collision models [85, 86]. Through the spin-auxiliary interaction D we can dissipate the spin(s) into the environment in a controlled manner. The non-unitary resets of the auxiliary will then make the environment Markovian (forgetting), and be the source which makes our whole circuit non-unitary. For connectivity reasons each spin interacts with it's own neighbouring auxiliary.

The circuits for one step of unitary, dissipation, and reset, as finally realized on the hardware, are in Appendix C.

3.2 Implementation of the Unitary

We start by explaining our method to realize the unitary $U = e^{-i\hat{H}_{SB}t}$, while we will describe the implementation of the dissipation D and reset $|0\rangle$ separately in Sec. 4.
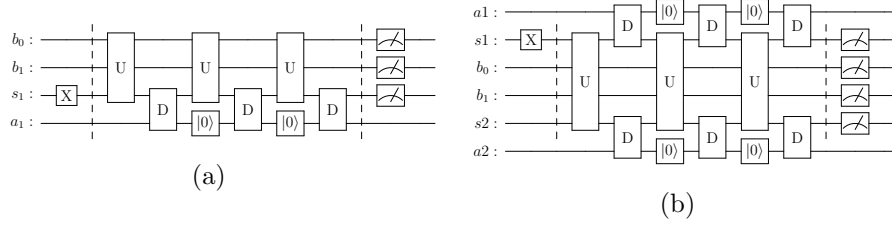
Figure 3.1: Circuit structure, alternating between a unitary evolution U, dissipative interactions with auxiliary qubits D, and resets $|0\rangle$. A system of (a) one spin (b) two spins. Here the spins are represented by s_k, the harmonic oscillator modes (4 levels) are encoded on the b_k qubits and the ancilla qubits are represented by a_k. X-gate represents the initial state preparation, the final gates represent measurements.

3.2.1 Mapping Bosons to Qubits

To realize a unitary $e^{-i\hat{H}t}$ into a set of gates on a circuit, the Hamiltonian must be written in terms of Pauli (spin) operators. Fermionic operators can be mapped in a straight forward way using the Jordan-Wigner transformation, Bravyi–Kitaev representation [87], or newer algorithms [88, 89]. While the fermionic part of the Hamiltonian $\hat{H}_{SB}$ is already in terms of Pauli matrices, we need to translate the bosonic operators.

A few ways of mapping bosonic systems to a set of qubits have been explored in the literature [90, 91, 92, 93, 94, 95]. Sawaya et al. [95] introduced the d-level-to-qubit mapping, which is based on encoding the Fock-basis (second quantization), where each energy level of the harmonic oscillator $|n\rangle$ represents one level of a d-level system. While the mapping is theoretically identical to one used for first quantization operators [93], our Hamiltonian is already in terms of second quantization operators, we chose to use the d-level-encoding.

The steps of the d-level-to-qubit mapping can be summarized as follows [95]. The goal is to encode the bosonic operators $\hat{A}$ as strings of Pauli matrices.

1. Truncate the infinite-dimensional harmonic oscillator $|n\rangle$ at d_{HO} levels

$$n = 0, \ldots, d_{HO} - 1 \ \text{ and } \ a^\dagger |n\rangle = 0 \tag{3.1}$$

2. Rewrite each bosonic operator as a sum of transitions from levels $|n'\rangle$ to $|n\rangle$

$$\hat{A} = \sum_{n,n'=0}^{d_{HO}-1} a_{n,n'} |n\rangle \langle n'|, \ \hat{A} \in \{\hat{a}, \hat{a}^\dagger, \hat{a}^\dagger\hat{a}\} \tag{3.2}$$

3. Assign each level an integer

$$|n\rangle \xrightarrow{\text{integer}} |l\rangle \, , \ l \in \mathbb{N} \tag{3.3}$$

4. Write each integer in binary

$$|l\rangle \xrightarrow{\text{integer-to-bit}} \bigotimes_{m=1}^{Q_B} |b_m\rangle \, , \ b_m \in \{0,1\} \tag{3.4}$$

5. Map each bit pair $|b_m\rangle \langle b_m'|$ to Pauli matrices using

$$
\begin{aligned}
|0\rangle \langle 0| &= \frac{1}{2} \left(\mathbb{1} + \hat{\sigma}^z \right) \\
|1\rangle \langle 1| &= \frac{1}{2} \left(\mathbb{1} - \hat{\sigma}^z \right) \\
|0\rangle \langle 1| &= \frac{1}{2} \left(\hat{\sigma}^x + i\hat{\sigma}^y \right) = \hat{\sigma}^+ \\
|1\rangle \langle 0| &= \frac{1}{2} \left(\hat{\sigma}^x - i\hat{\sigma}^y \right) = \hat{\sigma}^-
\end{aligned}
\tag{3.5}
$$

This results in each level-transition written as a string of Pauli operators and each bosonic operator $\hat{A}$ written as a sum of N_P Pauli strings

$$\hat{A} = \sum_{k=1}^{N_P} c_k \bigotimes_{j=1}^{Q_B} \hat{\sigma}_{kj}, \ \hat{\sigma}_{kj} \in \{\mathbb{1}, \hat{\sigma}^x, \hat{\sigma}^y, \hat{\sigma}^z\} \tag{3.6}$$

Where a Pauli string is a tensor product of Pauli matrices over all qubits $\hat{\sigma}^{(\cdot)} \otimes \hat{\sigma}^{(\cdot)} \otimes \ldots \hat{\sigma}^{(\cdot)} = \hat{\sigma}^{(\cdot)} \hat{\sigma}^{(\cdot)} \ldots \hat{\sigma}^{(\cdot)}$. $Q_B = \lceil \sqrt{d_{HO}} \rceil$ is the number of qubits needed to encode d_{HO} bosonic levels, and $\lceil \cdot \rceil$ is the ceiling function.

Integer-to-Bit Encodings

The choice of integer-to-bit encoding warrants a closer look, since they affect the number of gates required to implement a given Hamiltonian. Integer-to-bit encodings are mappings which write arbitrary integers as a set of ordered binary numbers. The easiest example is the standard binary way of counting $\{0, 1, 2, 3\} \rightarrow \{00, 01, 10, 11\}$.

Standard binary and Gray code [94] are examples of compact encodings, meaning that the make use of the full Hilbert space by mapping to all possible combinations of 0s and 1s. A popular non-compact encoding is unary (also called one-hot), which maps $\{0, 1, 2, 3\} \rightarrow \{0001, 0010, 0100, 1000\}$. Non-compact encodings require more qubits $Q_B \geq \lceil \sqrt{d_{HO}} \rceil$, but the hope is that

they require less gates. Since they do not make use of the full Hilbert space, only a subset of bits is necessary to uniquely identify each integer. In the unary encoding, if one knows that a bit b is set to 1, then one knows all other bits to be 0. As a consequence, one can ignore all bit pairs $|0\rangle \langle 0|$ in step 5., and only map pairs where $b_m = 1$ or $b'_m = 1$ when using unary.

We will compare the performance of the integer-to-bit encodings standard binary, Gray code, and unary in Sec. 5.1.3.

3.2.2 Trotterization

To implement the unitary evolution operator $U = e^{-i\hat{H}_{SB}t}$ we need to rely on a second layer of Trotterization (sometimes called product formulae or Suzuki-Trotter formulae). The reason is that it is unknown how to express exponentials of sums of Pauli strings $e^{-i\sum_k h_k t}$ into a set of gate instructions, while it is known for exponentials of individual Pauli strings $e^{-ih_k t}$.

The simplest Trotterization is the first order Suzuki-Trotter (or Lie-Trotter) product formula

$$e^{-i\hat{H}_{SB}t} = e^{-i\sum_{k=1}^{N} h_k t} \tag{3.7}$$

$$= \left(\prod_{k=1}^{N} e^{-ih_k \Delta t} \right)^{\frac{t}{\Delta t}} + \mathcal{O}(t\Delta t) \tag{3.8}$$

$$= \left(e^{-ih_1 \Delta t} \, e^{-ih_2 \Delta t} \, ... \, e^{-ih_N \Delta t} \right)^{\frac{t}{\Delta t}} + \mathcal{O}(t\Delta t) \tag{3.9}$$

where h_k are N different, generally non-commuting, Pauli strings, i.e. terms of the encoded Hamiltonian. See Eqs. (B.1, B.2) in Appendix B for more details on h_k.

A better approximation is given by the second order Suzuki-Trotter formula [96, 97]

$$e^{-i\hat{H}_{SB}t} = e^{-i\sum_{k=1}^{N} h_k t} \tag{3.10}$$

$$= \left(\prod_{k=1}^{N} e^{-ih_k \Delta t/2} \prod_{k=N}^{1} e^{-ih_k \Delta t/2} \right)^{\frac{t}{\Delta t}} + \mathcal{O}(t\Delta t^2) \tag{3.11}$$

$$= \left(e^{-ih_1 \frac{\Delta t}{2}} \, ... \, e^{-ih_N \frac{\Delta t}{2}} \, e^{-ih_N \frac{\Delta t}{2}} \, ... \, e^{-ih_1 \frac{\Delta t}{2}} \right)^{\frac{t}{\Delta t}} + \mathcal{O}(t\Delta t^2) \tag{3.12}$$

The individual exponentials of Pauli strings $e^{-ih_k \Delta t}$ are then implemented via the CNOT-staircase [57, 32], which is taken care of by Qiskit [98]. We will use both the first and second order Suzuki-Trotter formulae, and explore their trade-offs in Sec. 5.2.

3.2.3 Decomposition of Isometries

So far we described how to implement the unitary on a quantum circuit by Trotterization: encoding the Hamiltonian into Pauli matrices, Trotterizing the unitary, and using the CNOT-staircase. Alternatively one can write out the unitary matrix and try to directly decompose it into a set of gates via optimization on a classical computer.

For a 2×2 unitary, the corresponding gate is just the universal single-qubit rotation, or U3-gate. For a two-qubit 4×4 unitary, the KAK decomposition method [99] requires an optimal number of CX-gates. For larger unitaries, the decomposition of isometries (DoI) [100] [101] can implement any arbitrary unitary, with a theoretical lower bound on the number of used CX-gates gates.

While the DoI is close to exact, the classical overhead and circuit depth are significantly higher than for Trotterization. In general, the DoI of a $n \times n$ unitary requires $2^{2n} - \frac{1}{24}2^n + O(n^2)2^n$ CX-gates and a classical run time of $O(n2^{3n})$ [102]. In our case, the DoI of a 3-qubit unitary (one spin and 4 HO levels) requires 23 CX-gates, while a 5-qubit unitary (two spins and 8 HO levels) already requires 507 CX-gates (tab. 5.2). (AB: fix numbers) The scaling in the number of gates with increasing qubit counts are unrealistic for use with NISQ devices. In addition, the classical overhead meant our laptop frequently ran out of computing power when trying to decompose unitaries bigger than $2^6 \times 2^6$.

While DoI could be useful for simulating the smallest unitaries that we are considering, for our method to remain scalable to larger systems, we will use Trotterization instead of DoI. We will use DoI in some noiseless simulations, where gate depth does not matter, and for the 4×4 unitaries describing two-qubit interactions in Sec. 4.

3.2.4 Other Methods to Implement the Unitary

Trotterization was the first method used to realize a unitary on a circuit [6], but since then improvements and new methods have been developed, which do not require the classical optimization necessary for DoI. While we do not use them in this thesis, we want to briefly review some alternative methods and discuss why we prefer to use Trotterization.

Suzuki-Trotter formulas are a relatively simple and surprisingly effective method, but the circuit size depends linearly on the number of terms in the system Hamiltonian making it only practical for sparse Hamiltonians [103].

A minor variation of Trotterization is to use a randomized product formula, which simply randomizes the order of the terms $e^{-ih_k \Delta t}$. Although randomizing was shown to have some advantages in some systems, we did not experiment

with it on the spin-boson Hamiltonian and could give minor improvements to our method.

Similarly the quantum stochastic drift protocol (QDrift) selects each Trotter term randomly, but does so with a probability based on the term's weight. While random, it will stochastically drift towards the correct unitary over time [103]. The query complexity does not dependent of number of terms, but instead on the overall strength (l1-norm) of the Hamiltonian. The downside is that the asymptotic scaling in time at a given error rate is the same as the first order Trotter formula and performs worse than the second order formula [104]. For the spin-boson Hamiltonian QDrift already performed worse than first order Trotterization, probably due to our Hamiltonian's l1-norm, although we did not investigate further.

In the Taylor-series expansion, the Hamiltonian itself is repeatedly applied to the system until a truncation point. Since the Hamiltonian is not a unitary matrix, it is split into a LCU [105, 106]. LCU can be implemented on a single circuit using controlled operations called uniformly controlled gates (UCG) or quantum multiplexers. Decomposing these controlled operations over many qubits into CX-gates and single-qubit-gates usually results in deep circuits, making it unfeasible for our Hamiltonian.

Qubitization is an alternative approach that's a popular choice for electronic structure Hamiltonians, that uses ideas from quantum walks. It builds on the quantum signal processing (QPE) algorithm, which works by mapping the eigenvalues of the Hamiltonian onto an auxiliary qubit [107]. Alternatively, the ground state energy can be found via quantum phase estimation (QPE). Qubitization requires additional qubits to store the eigenvalues, but scales provably optimal with the evolution time and the error tolerance. Like LCU methods, QPE heavily relies on gates controlled by multiple qubits, called Toffoli gates, which have to be decomposed into many CX-gates. Thus while promising, Qubitization can not be efficiently implemented on NISQ devices.

3.3   Simulation Methods

3.3.1   Quantum Hardware

The Quantum Computers we use are the transmon-based 7-qubit `ibm_jakarta` and the 27-qubit `ibm_toronto` devices provided by IBM. As a default we use `ibm_jakarta`, unless for the cases where we require more than seven qubits. To perform simulations of quantum circuits and run experiments on actual quantum hardware, we use IBM's Qiskit software [98].

Both devices use the native gate set {CNOT, ID, RZ, SX, X}, which we define in Sec. A.3. In the literature and in this thesis circuits are often described

by non-native gates or assuming perfect connectivity, as both vary from device to device. In these cases the circuits are classically processed (transpiled) into the native gates and connectivity of the actual hardware, before running an experiment. The transpiling process is handled by Qiskit.

All operations on a quantum computer are unitary, with the exceptions of measurements, resets, and the natural occurring noise. In many devices the reset is implemented by idling the qubit and waiting for it to relax down to the ground state, or accelerating the process by actively dissipating the qubit (cavity-cooling) [108, 109]. In IBM's devices, the reset is implemented as a conditional reset. Each reset is composed of a mid-circuit measurement, conditionally followed by an x-gate, ensuring the qubit is in the $|0\rangle$ state after the operation. As a consequence we can calculate the action of resetting a subsystem as taking the partial trace over that subsystem (i.e. tracing out the subsystem).

Figure 3.2: Qubit connectivity of the used (a) `ibm_jakarta` and (b) `ibm_toronto` devices.

3.3.2 Measurements

Measurements are made in the standard computational z-basis $\hat{=}\{|0\rangle , |1\rangle\}$, from which we get the state probabilities $\mathcal{P}_k = |\,|\phi_k\rangle\,|^2$. To make a Measurement in the x-basis, we insert a π-rotation about the X+Z axis, known as the Hadamard-gate, before the regular z-measurement [110]. Similarly for the y-basis we apply a S-adjoint-gate ($S^\dagger$-gate) and a Hadamard-gate, followed by the measurement.

As a default we run each circuit with $2^{13} = 8192$ shots (repetitions) and take the mean of the measured probabilities.

Quantum State Tomography We obtain the density matrix $\hat{\rho}^{approx}$ of a state on a circuit via quantum state tomography. It is comprised of running the same circuit multiple times, with final measurements in the z-, y-, and x-basis. The density matrix is then reconstructed using least-squares fitting.

The number of measurements needed to characterize the density matrix, scales exponentially with the number of qubits, as each combination of qubits and bases are measured.

3.3.3 Classical Simulations

We verify our results with a classical Lindblad Master equation solver in the Quantum Toolbox in Python (QuTiP) library [111]. This provides us with the evolution of the density matrix $\hat{\rho}^{exact}$, to which we will just refer to as the exact result.

3.3.4 Error Measures and Observables

To measure the error at each point in time we use the infidelity, which measures the overlap in the density matrices $\mathcal{I}$ [112]

$$\mathcal{I}(\hat{\rho}^{exact}, \hat{\rho}^{approx}) = 1 - \left(\text{Tr} \left[\sqrt{\sqrt{\hat{\rho}^{exact}} \hat{\rho}^{approx} \sqrt{\hat{\rho}^{exact}}} \right] \right)^2 \qquad (3.13)$$

In some context we are only interested in the state probabilities $\mathcal{P}_k$, the diagonal elements of the density matrix.

$$|\psi\rangle = \sum_{k=1}^{N_{states}} \langle\phi_k|\psi\rangle |\phi_k\rangle , \ \mathcal{P}_k = |\langle\phi_k|\psi\rangle|^2 \qquad (3.14)$$

In that case we use the mean absolute error (MAE)

$$\mathcal{E}_{MA} = \frac{1}{N_{states}} \sum_{k=1}^{N_{states}} |\mathcal{P}_k^{True} - \mathcal{P}_k^{Measured}| \qquad (3.15)$$

Computing Observables

From a physical point of view we are interested in simulating observables beyond the state probabilities.

We get the average occupation in the Harmonic Oscillator from classically post-processing the probabilities of the states

$$\langle\hat{n}\rangle = \langle\hat{a}^\dagger\hat{a}\rangle = \sum_{k=1}^{N_{states}} \mathcal{P}_k \cdot n_k, \ n_k |\phi_k\rangle = \hat{n} |\phi_k\rangle \qquad (3.16)$$

Where n is the number of bosons associated with a state $|\phi\rangle$, $\hat{n} |\phi\rangle = n |phi\rangle$.

For the spins we measure their values in the z- and x-direction to get $\langle\hat{S}^z\rangle$ and $\langle\hat{S}^x\rangle$. For the two spin case we also look at the connected correlation

$$C^{ZZ} = \langle\hat{S}_1^z\hat{S}_2^z\rangle - \langle\hat{S}_1^z\rangle\langle\hat{S}_2^z\rangle \tag{3.17}$$

$$C^{XX} = \langle\hat{S}_1^x\hat{S}_2^x\rangle - \langle\hat{S}_1^x\rangle\langle\hat{S}_2^x\rangle \tag{3.18}$$

These connected correlation functions (also called Ursell functions or cumulants) corresponds to the covariance in statistics and vanish if and only if $\hat{\sigma}_1^{(\cdot)}$ and $\hat{\sigma}_2^{(\cdot)}$ are statistically independent [113, 114, 115]. In the quantum circuit we measure the both spins in the z-/x-basis and classically calculate

$$\begin{aligned}
C =& \langle\hat{S}_k\hat{S}_l\rangle - \langle\hat{S}_k\rangle\langle\hat{S}_l\rangle = \\
=& + (\mathcal{P}_{00} + \mathcal{P}_{11} - \mathcal{P}_{10} - \mathcal{P}_{01})_{kl} \\
& - (-\mathcal{P}_{00} - \mathcal{P}_{01} + \mathcal{P}_{10} + \mathcal{P}_{11})_k \\
& \cdot (-\mathcal{P}_{00} - \mathcal{P}_{10} + \mathcal{P}_{01} + \mathcal{P}_{11})_l
\end{aligned} \tag{3.19}$$

In QuTiP we calculate observables $\hat{O}$ from the density matrix.

$$\langle\hat{O}\rangle = \text{Tr}\left[\hat{\rho}^{exact}\cdot\hat{O}\right] \tag{3.20}$$

The operator $\hat{O}$ reads explicitly

$$\begin{aligned}
\langle\hat{n}\rangle: \quad & \hat{O} = \mathbb{1}_{S_k} \otimes \hat{n} \quad \otimes \mathbb{1}_{S_l} \\
\langle\hat{S}_1\rangle: \quad & \hat{O} = \mathbb{1}_{S_1} \otimes \mathbb{1}_{HO} \otimes \hat{S}_2 \\
\langle\hat{S}_2\rangle: \quad & \hat{O} = \hat{S}_1 \quad \otimes \mathbb{1}_{HO} \otimes \mathbb{1}_{S_2} \\
C: \quad & \hat{O} = \hat{S}_1 \quad \otimes \mathbb{1}_{HO} \otimes \hat{S}_2
\end{aligned}$$

for the average occupation, spin of the first and second spin, and the connected correlation respectively.

3.3.5 Error Mitigation

Error mitigation is a class of techniques that use classical post-processing to reduce the effects of noise [24]. Error correction algorithms in contrast combine multiple qubits into fewer logical qubits, essentially by using extra qubits to detect any errors through quantities like the parity. Error correction has only recently been first demonstrated in superconducting devices [116, 117, 118], but we will not discuss this further here.

Coming back to error mitigation methods, the required classical computing power or number of measurements usually scales unfavourably with the number of qubits. Nevertheless they can improve errors considerably in NISQ devices and are envisioned to continue to be useful.

Measurement Error Mitigation

The error mitigation technique we are going to use throughout is Qiskit's implementation of measurement error mitigation.

In short, the circuit is measured without any gates for the calibration step, knowing that all qubits should be measured as $|0\rangle$. Repeating this measurement gives a noise matrix describing the error of the readout. In the second step the noise matrix is inverted, which in practice is approximated using least-squares fitting. The inverse noise matrix is then applied to all future measurements of the actual, non-empty, circuits of interest.

Further Error Mitigation Techniques

We want to mention a couple of other error mitigation algorithms which are potentially useful but beyond the scope of this work.

Next to the measurement error mitigation we use, there are multiple improved versions with various scalings in measurements and classical complexity [119, 120].

A similar idea is to characterize the noise in the gates and then again invert the effects due to noise. Zero noise extrapolation (ZNE) [22, 23, 121] does so by first increasing the noise via Pulse-stretching, gate-folding, or unitary folding, to then fit a curve (extrapolate) to find the noiseless limit.

A recompilation of a circuit aims to find a new circuit which can approximate a desired circuit to a high degree but with a reduced number of gates. The new circuit is, for example, build up by incrementally adding gates and optimising the gate parameters at each step [122, 35, 123, 124, 125].

In Clifford data regression a classical computer simulates quantum circuits that resemble the circuit of interest, but which are easier to classically calculate [126]. Then a linear model is trained on the results from the noisy quantum circuit and the approximation on the classical computer to predict noise-free observables.

Probabilistic error cancellation (PEC) [127, 128] is an idea where the desired ideal gates are replaced by linear combinations of implementable noisy gates. One then samples a Monte Carlo average from this linear combinations of noisy gates to approximate the desired expectation values.

While many of these techniques have been used to great success, their computational complexity, and the effort required to implement them efficiently, pose significant hurdles. For these reasons we will only use the already implemented, and comparatively fast, measurement error mitigation in Qiskit and leave these methods as possible future avenues.

3.4 Reduced-Noise Models

While it is important to study how well current quantum processors can simulate our system, we also aim to explore what outcomes could be possible on future, less noisy, hardware.

To describe their current devices, IBM supplies noise models based on device properties measured during calibration. To simulate these reduced-noise-scenarios, we use the same error channels that IBM, but alter the device properties.

The noise models include error sources in the gates, as thermal relaxation (relaxation and dephasing) and depolarizing errors, and also readout errors [129].

For our reduced-noise models we scale down the average gate infidelity $\mathcal{I}_{Gate}$, the gate times t_{Gate}, and the false-readout probabilities $P(1|0)$, $P(0|1)$ by the same noise-factor ξ. Explicitly:

$$\mathcal{I}_{Gate} \to \xi \cdot \mathcal{I}_{Gate} \tag{3.21}$$

$$t_{Gate} \to \xi \cdot t_{Gate} \tag{3.22}$$

$$P(1|0), \ P(0|1) \to \xi \cdot P(1|0), \ \xi \cdot P(0|1) \tag{3.23}$$

Importantly for our reduced-noise models, the Infidelity from thermal relaxation $\mathcal{I}_T$ is linear in the gate time t_{Gate}. Thus when we rescale $\mathcal{I}_{Gate} \to \xi \cdot \mathcal{I}_{Gate}$, $t_{Gate} \to \xi \cdot t_{Gate}$, we indirectly scale $\mathcal{I}_D \to \xi \cdot \mathcal{I}_D$, $\mathcal{I}_T \to \xi \cdot \mathcal{I}_T$. This way the relative contribution of the error channels $\mathcal{I}_D/\mathcal{I}_T$ to the infidelity remains unchanged.

Indeed, realistically some of these parameters will not see equal improvement in the next years, but a more detailed analysis of differentiated improvements of different aspects is beyond the scope of this work.

3.4.1 Error Sources

At every gate, first the thermal relaxation and then the depolarizing error is applied. The strength of the depolarizing error is calculated backwards, to reach a target 'gate error' when combined with the thermal relaxation. Details can be found at [130].

Thermal Relaxation Error

Thermal relaxation is defined by the qubit-specific parameters $T1$ time, $T2$ time, qubit frequency f_{Qubit} and qubit temperature $\mathcal{T}_{Qubit}$. The thermal error channel is then given time to act according to a gate-dependent gate time. For

two-qubit-gates, the error is simply the tensor product between two single-qubit channels.

$T1$ is qubit-specific time until relaxation, i.e. to decay from the excited state to the ground state. $T2$ qubit-specific coherence time, or time until dephasing. The qubit frequency f_{Qubit} is the difference in energy between the ground and excited states. The qubit temperature $\mathcal{T}_{Qubit}$ is assumed to be 0 in Qiskit's and our noise models.

The qubit frequency and temperature enter only via the excited state population. If $f_{Qubit} = \infty$ or $\mathcal{T}_{Qubit} = 0$, the excited state population is 0. Since $\mathcal{T}_{Qubit} = 0$ in our models, both the frequency and temperature can effectively be ignored as parameters.

For $T_2 < T_1$, thermal relaxation is most straight-forwardly described by (assuming the device to be at 0 temperature)

$$K_{T_0} = \sqrt{\mathcal{P}_I}\mathbb{1}, \tag{3.24}$$

$$K_{T_1} = \sqrt{\mathcal{P}_Z}\hat{\sigma}^z, \; K_{T_2} = \sqrt{\mathcal{P}_{reset}}\,|0\rangle\langle0| \tag{3.25}$$

$$\mathcal{E}_T(\hat{\rho}) = \sum_{i=10}^{2} K_{T_k}\hat{\rho}K_{T_k}^\dagger \tag{3.26}$$

It is composed of the probabilities of a phase-flip $\mathcal{P}_Z$, a reset to the ground state $\mathcal{P}_{reset}$, or for nothing to happen $\mathcal{P}_{\mathbb{1}}$. The probabilities $\mathcal{P}_Z$, $\mathcal{P}_{reset}$ are calculated of T_1, T_2 and the gate time t_{Gate}.

$$\mathcal{P}_{reset} = 1 - \mathcal{P}_{T_1} = 1 - e^{-t_{Gate}\cdot\frac{1}{T_1}} \tag{3.27}$$

$$\mathcal{P}_Z = (1 - \mathcal{P}_{reset})(1 - \frac{\mathcal{P}_{T_2}}{\mathcal{P}_{T_1}})/2 \tag{3.28}$$

$$= (1 - \mathcal{P}_{reset})(1 - e^{-t_{Gate}\cdot(\frac{1}{T_2} - \frac{1}{T_1})})/2 \tag{3.29}$$

$$\mathcal{P}_{\mathbb{1}} = 1 - \mathcal{P}_Z - \mathcal{P}_{reset} \tag{3.30}$$

If $2T_1 \geq T_2 > T_1$ thermal relaxation has to be described by it's Choi matrix

$$\hat{\rho} \rightarrow \mathcal{E}_T(\hat{\rho}) = tr_1[C(\hat{\rho}^T \otimes I)] \tag{3.31}$$

$$C_{\mathcal{E}_T} = \begin{pmatrix} 1 & 0 & 0 & \mathcal{P}_{T_2} \\ 0 & 0 & 0 & 0 \\ 0 & 0 & \mathcal{P}_{reset} & 0 \\ \mathcal{P}_{T_2} & 0 & 0 & 1 - \mathcal{P}_{reset} \end{pmatrix} \tag{3.32}$$

Which can also be used if $T_2 < T_1$ to compute the process fidelity in Eq. (3.41).

At the time of writing all qubits on the Jakarta hardware satisfied $T_2 < T_1$, while on ibmq_toronto some qubits show $T_2 > T_1$.

Depolarizing Error

The depolarizing noise (or Pauli) channel is composed of either a bit-flip ($\hat{\sigma}^x$), a phase-flip ($\hat{\sigma}^z$) or both at the same time ($\hat{\sigma}^y$), all with equal probability [129].

$$\hat{\rho} \to \mathcal{E}_D(\hat{\rho}) = \sum_{i=1}^{3} K_{\mathcal{P}_k} \hat{\rho} K_{\mathcal{P}_k}^{\dagger} \tag{3.33}$$

$$K_{\mathcal{P}_0} = \sqrt{1 - \mathcal{P}_D}\mathbb{1}, \ K_{\mathcal{P}_1} = \sqrt{\frac{\mathcal{P}_D}{3}}\hat{\sigma}^x \tag{3.34}$$

$$K_{\mathcal{P}_2} = \sqrt{\frac{\mathcal{P}_D}{3}}\hat{\sigma}^y, \ K_{\mathcal{P}_3} = \sqrt{\frac{\mathcal{P}_D}{3}}\hat{\sigma}^z \tag{3.35}$$

Gate Infidelity The depolarizing error is calculated from the target gate infidelity $\mathcal{I}_{Gate}$, and the infidelity due to thermal relaxation $\mathcal{I}_T$. The probability of a depolarizing error is calculated such that errors not explained by thermal relaxation are said to be due to the depolarizing channel

$$\mathcal{I}_D = \mathcal{I}_{Gate} - \mathcal{I}_T \tag{3.36}$$

The target gate infidelity is given as a parameter, while $\mathcal{I}_T$ has to be calculated as

$$\mathcal{F}_T = 1 - \mathcal{I}_T \tag{3.37}$$

$$= \mathcal{F}_{avg}(\mathcal{E}_T, U) \tag{3.38}$$

$$= \int d\phi \langle \phi | U^{\dagger} \mathcal{E}_T(|\phi\rangle\langle\phi|) U | \phi \rangle \tag{3.39}$$

$$= \frac{d\mathcal{I}_{pro}(\mathcal{E}_T, U) + 1}{d + 1} \tag{3.40}$$

where $\mathcal{I}_{pro}(\mathcal{E}_T, U)$ is the Process fidelity of the input quantum channel $\mathcal{E}_T$ with a target unitary U, and d is the dimension of the channel.

$$\mathcal{I}_{pro}(\mathcal{E}_T, \mathcal{F}) = F(C_{\mathcal{E}_T}/d, \rho_{\mathcal{F}}) \tag{3.41}$$

where $\mathcal{F}$ is the state fidelity as defined in the main text

$$\mathcal{F}(\rho_1, \rho_2) = \left(\text{Tr} \left[\sqrt{\sqrt{\rho_1}\rho_2\sqrt{\rho_1}} \right] \right)^2 \tag{3.42}$$

$C_{\mathcal{E}_T}/d$ is the normalized Choi matrix for the channel $\mathcal{E}_T$, and d is the input dimension of $\mathcal{E}_T$.

Depolarizing Error Probability If we write the depolarizing error in terms of the identity and the complete depolarizing channel D, we can rewrite the gate fidelity

$$\mathcal{E}_D = (1 - \mathcal{P}_D) \cdot \mathbb{1} + \mathcal{P}_D \cdot D \tag{3.43}$$

$$\mathcal{F}_{gate} = 1 - \mathcal{I}_{Gate} \tag{3.44}$$

$$= \mathcal{F}(\mathcal{E}_D \cdot \mathcal{E}_T) \tag{3.45}$$

$$= (1 - \mathcal{P}_D)\mathcal{F}_T + \mathcal{P}_D \cdot \mathcal{F}_D \tag{3.46}$$

$$= \mathcal{F}_T - \mathcal{P}_D \cdot (d \cdot \mathcal{F}_T - 1)/d \tag{3.47}$$

Where $d = 2^{qubits}$ is the dimensionality of the gate. From this the solution for the depolarizing error probability is

$$\mathcal{P}_D = d(\mathcal{F}_T - \mathcal{F}_{gate})/(d \cdot \mathcal{F}_T - 1) \tag{3.48}$$

$$= d(\mathcal{I}_{Gate} - \mathcal{I}_T)/(d \cdot \mathcal{F}_T - 1) \tag{3.49}$$

More details can be found at [130].

Measurement Error

A measurement error is equivalent to a bit-flip $\hat{\sigma}^x$ followed by a noiseless readout [129]. The probability of the readout error $\mathcal{P}_R$ is given by the probability $P(n|m)$ of recording a noisy measurement outcome as n, given the true measurement outcome is m.

$$K_{R_0} = \sqrt{1 - \mathcal{P}_R}\mathbb{1}, \; K_{R_1} = \sqrt{\mathcal{P}_R}\hat{\sigma}^x \tag{3.50}$$

$$\mathcal{P}_R = \sum_{n \neq m} P(n|m) \tag{3.51}$$

Where n, m run over all qubits, in the case of two qubits $n, m \in \{00, 01, 10, 11\}$. See [130] for further details.

Error Sources in Reference Device

Given the three error sources, one can ask which error source causes the dominant contribution to the noise in our results. As we use measurement error mitigation and it is independent of the circuit depth, we will ignore the measurement error. Instead we focus on the ratio of the thermal and depolarizing errors in contributing to the infidelity, $\mathcal{I}_T/\mathcal{I}_D$. To give a rough estimation, we assume all gates $g \in \{\text{CNOT, RZ, SX, X}\}$ and all qubits q are used equally often, and average over both.

$$\mathcal{I}_T/\mathcal{I}_D = \frac{1}{N_q}\sum_{q=1}^{N_q}\left(\frac{1}{N_g}\sum_{g}^{N_g=4}\left(\frac{\mathcal{I}_T(q,g)}{\mathcal{I}_D(q,g)}\right)\right) \tag{3.52}$$

	ibm_jakarta	ibm_toronto
Processor	Falcon r5.11H, V1.1.0	Falcon r4, V1.7.7
Avg. CX-gate Error	1.109e-2	4.936e-2
Avg. Readout Error	3.349e-2	4.119e-2
Avg. T1	139.01 us	113.87 us
Avg. T2	44.82 us	101.63 us
Avg. Gate time	341.333 ns	454.095 ns
Avg. Qubit Frequency	5.16 GHz	5.08 GHz
Avg. Qubit Anharmonicity	-0.341 GHz	-0.329 GHz

Figure 3.3: Calibration data at the time of writing of the quantum computers used in this work.

We calculate $\mathcal{I}_T(q, g)$ and $\mathcal{I}_D(q, g)$ using Eqs. (3.37) and (3.36) respectively, and get the current calibration data from IBM. At the time of writing, the result for the Jakarta device is $\mathcal{I}_T/\mathcal{I}_D = 15.4$, while for the the older `ibm_toronto` device $\mathcal{I}_T/\mathcal{I}_D = 354.1$. We can conclude that in our systems thermal relaxation is the main source of infidelity by one to two orders of magnitude compared to depolarization.

We want to point out that this does not hold for all devices. For example, the newest generation of chips in the 127 qubit IBM Washington device show $\mathcal{I}_T/\mathcal{I}_D = 0.49$.

Calibration Data

We base our reduced-noise models on the same hardware that we run our full-noise circuits on, the 7 qubit Jakarta and 27 qubit Toronto devices. The question is which error source is the dominant one contributing to the noise in our results. The average calibration data at the time of writing is noted in Fig. 3.3. For more details see [131].

Chapter 4

Simulating Two-Level Dissipation

Before we model the full master equation Eq. (2.4), we simulate the dissipation in the spin(s), defined by Eq. (2.5), without the unitary evolution.

4.1 Interaction with an Auxiliary Qubit

The AD channel is a popular model to describe lossy systems, and has been studied in classical methods as well as quantum computing. As such, one finds a couple of different approaches in the literature which effectively describe the AD channel using quantum hardware [57, 55, 132, 85]. The idea common to these approaches is the use of an auxiliary qubit to perform a unitary operation on the bigger Hilbert space of both qubits. While sharing the underlying structure, the different approaches utilise different unitaries and lead to different circuits. In the following we will unify some of the previous techniques, by showing that they produce the same dynamics for the spin if (a) the auxiliary starts in the $|0\rangle$ state and (b) the auxiliary is traced out after the interaction. In our scheme (Sec. 3.1) we trace out the auxiliary by measuring and resetting.

4.1.1 Kraus Operators

We described the quantum channel (or quantum map) of our open system using a GKSL master equation. A quantum channel $\mathcal{C}$ is a linear, unital and completely-positive map which maps the density matrix at one time to a later time. In the Heisenberg picture, by Choi's theorem [133], the channel $\mathcal{C}$ takes

the form

$$\mathcal{C}(\hat{\rho}) = \hat{\rho}(t) = \sum_k K_k \hat{\rho} K_k^{\dagger}, \ \sum_k K_k^{\dagger} K = \mathbb{1} \tag{4.1}$$

Which is called the operator sum (or Kraus) representation, and the operators K_k are called Kraus operators of $\mathcal{C}$. Such a Kraus representation always exists [134]. While the Kraus operators can be obtained starting from the GKSL, it is in general hard [135].

For the AD channel, the Kraus operators are well known and are given by [55, 136]

$$K_0 = \sqrt{\lambda} \begin{bmatrix} 1 & 0 \\ 0 & \sqrt{1-\mu} \end{bmatrix}, \qquad K_1 = \sqrt{\lambda} \begin{bmatrix} 0 & \sqrt{\mu} \\ 0 & 0 \end{bmatrix}$$

$$K_2 = \sqrt{1-\lambda} \begin{bmatrix} \sqrt{1-\mu} & 0 \\ 0 & 1 \end{bmatrix}, \ K_3 = \sqrt{1-\lambda} \begin{bmatrix} 0 & 0 \\ \sqrt{\mu} & 0 \end{bmatrix}$$

Where $\lambda = \left(1 + e^{-(k_B T)^{-1}}\right)^{-1}$ adjusts the equilibrium state to the temperature of the system. In our case we are interested in $\hat{L}_{S_i} = |\downarrow\rangle\langle\uparrow|$, which is the special case of zero temperature, i.e. $\lambda = 1$. In the zero-temperature-limit the channel is described by only K_0 and K_1. The Kraus operators are non-unitary and cannot directly be implemented on a quantum circuit. Instead we can use their minimal unitary dilation $\hat{\mathcal{U}}$, using the Sz.-Nagy theorem, as reported by [54].

$$\hat{\mathcal{U}}_A = \begin{pmatrix} A & D_{A^{\dagger}} \\ D_A & -A^{\dagger} \end{pmatrix}, \ D_A = \sqrt{\mathbb{1} - A^{\dagger} A} \tag{4.2}$$

The minimal unitary dilations of K_0 and K_1 are:

$$\hat{\mathcal{U}}_{K_0} = \begin{pmatrix} 1 & 0 & 0 & 0 \\ 0 & \sqrt{1-\mu} & 0 & \sqrt{\mu} \\ 0 & 0 & -1 & 0 \\ 0 & \sqrt{\mu} & 0 & -\sqrt{1-\mu} \end{pmatrix}, \tag{4.3}$$

$$\hat{\mathcal{U}}_{K_1} = \begin{pmatrix} 0 & \sqrt{\mu} & \sqrt{1-\mu} & 0 \\ 0 & 0 & 0 & 1 \\ 1 & 0 & 0 & 0 \\ 0 & \sqrt{1-\mu} & -\sqrt{\mu} & 0 \end{pmatrix} \tag{4.4}$$

Parameter μ

Before we can implement Eq. (4.3), we need to find the right value for the parameter μ. Since we originally stated the problem in the form of the GKSL

master equation, we want to express μ in terms of the parameters γ and t. We can get an expression for μ by comparing the action of the Kraus operators to the action of the original AD master equation in Eq. (2.5).

The Kraus operators K_0, K_1 will evolve the density matrix of the spin $\hat{\rho}_S$ as [132]

$$\hat{\rho}_S = \begin{pmatrix} p & q \\ q^* & 1-p \end{pmatrix} \rightarrow \begin{pmatrix} \mu + p(1-\mu) & q\sqrt{1-\mu} \\ q^*\sqrt{1-\mu} & (1-\mu)(1-p) \end{pmatrix} \tag{4.5}$$

Applying the master equation Eq. (2.5) to the same density matrix gives

$$\dot{p} = \gamma(1-p) \;\rightarrow\; p(t) = p_0 e^{-\gamma t} + (1 - e^{-\gamma t})$$
$$\dot{q} = -\frac{\gamma q}{2} \qquad \rightarrow\; q(t) = q_0 e^{-\gamma t/2}$$

By comparison of Eq. (4.5) and (4.6), we get $\mu = 1 - e^{-\gamma t}$.

Evolution of a Single Kraus Operator

In general, for multiple Kraus operators, each unitary dilation $\hat{\mathcal{U}}_{K_k}$ is implemented on a separate circuit, with the same initial state prepared on each. After the circuits are measured, the resulting probabilities are classically added together to give the probabilities of the evolved state. This poses a problem for our scheme, as it would require to prepare the state after the previous time-step to compute the next time-step at each Trotter step.

Importantly though, while one can use separate circuits to implement $\hat{\mathcal{U}}_{K_0}$, $\hat{\mathcal{U}}_{K_1}$, one does not need to evolve both unitary dilations. It suffices to evolve $\hat{U}_{Kraus} = \hat{\mathcal{U}}_{K_0}$ on $|0\rangle_A \langle 0| \otimes \hat{\rho}_S$ and trace out the auxiliary with a reset. We will quickly show that this is indeed the case. With the auxiliary starting in the ground state $|0\rangle$, the density matrix of spin and auxiliary will evolve as

$$\hat{\rho}_{AS}(t) = \hat{U}_{Kraus}\left[|0\rangle_A \langle 0| \otimes \hat{\rho}_S\right] \hat{U}^\dagger_{Kraus} \tag{4.6}$$

$$= \hat{U}_{Kraus} \begin{pmatrix} p & q & 0 & 0 \\ q^* & 1-p & 0 & 0 \\ 0 & 0 & 0 & 0 \\ 0 & 0 & 0 & 0 \end{pmatrix} \hat{U}^T_{Kraus} \tag{4.7}$$

$$= \begin{pmatrix} p & q\sqrt{1-\mu} & 0 & q\sqrt{\mu} \\ q^*\sqrt{1-\mu} & (1-\mu)(1-p) & 0 & \sqrt{\mu}\sqrt{1-\mu}(1-p) \\ 0 & 0 & 0 & 0 \\ q^*\sqrt{\mu} & \sqrt{\mu}\sqrt{1-\mu}(1-p) & 0 & 0 \end{pmatrix} \tag{4.8}$$

Where $\hat{U}_{Kraus}^{\dagger} = \hat{U}_{Kraus}^{T}$ is a real matrix, since $0 \leq \mu \leq 1$. To get the evolved density matrix of just the spin, we trace out the auxiliary (Eq. (A.18)) and renormalize $\hat{\rho}_S = \text{Tr}_A [\hat{\rho}_{AS}]$ to get

$$\hat{\rho}_S = \begin{pmatrix} p & q\sqrt{1-\mu} \\ q^*\sqrt{1-\mu} & (1-\mu)(1-p) \end{pmatrix} \tag{4.9}$$

After renormalizing to $\text{Tr}[\hat{\rho}_S] = 1$ we get back Eq. (4.5).

4.1.2   Amplitude Damping Matrix

A natural place to start for implementing a channel would be to apply Stinespring dilation [137] to get a unitary evolution on the expanded Hilbert space of our system (the spin) with the environment (auxiliary). This purified evolution is governed by the Hamiltonian [132]

$$\hat{H}_{AD} = g \left(\hat{\sigma}_S^+ \hat{\sigma}_A^- + \hat{\sigma}_S^- \hat{\sigma}_A^+ \right) \tag{4.10}$$

And described by the unitary operator $\hat{U}_{ADM} = e^{-i\hat{H}_{AD}t}$

$$\hat{U}_{ADM} = \begin{pmatrix} 1 & 0 & 0 & 0 \\ 0 & \cos gt & -i\sin gt & 0 \\ 0 & -i\sin gt & \cos gt & 0 \\ 0 & 0 & 0 & 1 \end{pmatrix} \tag{4.11}$$

Which we will call AD matrix.

Parameter g

From looking at $\hat{U}_{ADM}$, it is not obvious that it acts the same way on the spin as $\hat{U}_{Kraus}$. We proceed as with $\hat{U}_{Kraus}$, by starting with the auxiliary in the ground state $|0\rangle$

$$\hat{\rho}_{AS}(t) = \hat{U}_{ADM} \left[|0\rangle_A \langle 0| \otimes \hat{\rho}_S \right] \hat{U}_{ADM}^{\dagger} \tag{4.12}$$

And by taking the partial trace over the auxiliary

$$\hat{\rho}_S(t) = \text{Tr}_A [\hat{\rho}_{AS}(t)] \tag{4.13}$$

$$= \begin{pmatrix} p + (1-p)\sin^2 gt & q\cos gt \\ q^*\cos gt & (1-p)\cos^2 gt \end{pmatrix} \tag{4.14}$$

Comparing Eq. (4.13) with (4.5), we see that if $\sin^2 gt = \mu = 1 - e^{-\gamma t}$, and thus $gt = \arcsin\sqrt{1 - e^{-\gamma t}}$, $\hat{U}_{ADM}$ also describes the AD channel.

4.1.3 Amplitude Damping Circuit

While for the Kraus method and AD matrix we started from mathematical descriptions of our channel, we can ask whether there exists a description in terms of gates on a circuit. Indeed, in general any single-qubit channel can be reproduced with one CX-gate and one auxiliary [138]. For the AD channel there is an AD circuit as seen in Fig. 4.1, consisting of two controlled operations [57]. Specifically, a controlled-$R_Y(\theta)$ (rotation around y-axis) is followed by a controlled-NOT and a reset of the auxiliary qubit. The spin qubit is represented by s, and the auxiliary qubit by a.
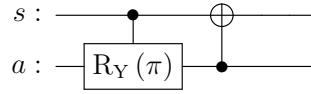
Figure 4.1: The amplitude damping circuit as described by [57] on generic hardware.

To compare the AD circuit with our previous approaches, we write the circuit in matrix form (see A.3 for the gate definitions)

$$\hat{U}_{ADC} = \mathrm{CRY}(\theta)_{f,a} \cdot \mathrm{CX}_{a,f} \tag{4.15}$$

$$= \begin{pmatrix} 1 & 0 & 0 & 0 \\ 0 & \cos\frac{\theta}{2} & 0 & -\sin\frac{\theta}{2} \\ 0 & 0 & 1 & 0 \\ 0 & \sin\frac{\theta}{2} & 0 & \cos\frac{\theta}{2} \end{pmatrix} \cdot \begin{pmatrix} 1 & 0 & 0 & 0 \\ 0 & 1 & 0 & 0 \\ 0 & 0 & 0 & 1 \\ 0 & 0 & 1 & 0 \end{pmatrix} \tag{4.16}$$

$$= \begin{pmatrix} 1 & 0 & 0 & 0 \\ 0 & \cos\frac{\theta}{2} & 0 & -\sin\frac{\theta}{2} \\ 0 & \sin\frac{\theta}{2} & 0 & \cos\frac{\theta}{2} \\ 0 & 0 & 1 & 0 \end{pmatrix} \tag{4.17}$$

Parameter θ

We show that $\hat{U}_{ADC}$ implements the AD channel for the right value of θ. As with $\hat{U}_{Kraus}$ and $\hat{U}_{ADM}$ we start with the auxiliary in the ground state and trace it out after evolving the joined density matrix $\hat{\rho}_{AS}$

$$\hat{\rho}_{AS}(t) = \hat{U}_{ADC} \left[|0\rangle_A \langle 0| \otimes \hat{\rho}_S \right] \hat{U}_{ADC}^\dagger \tag{4.18}$$

$$= \begin{pmatrix} p & q\cos\frac{\theta}{2} & q\sin\frac{\theta}{2} & 0 \\ q^*\cos\frac{\theta}{2} & (1-p)\cos^2\frac{\theta}{2} & (1-p)\sin\frac{\theta}{2}\cos\frac{\theta}{2} & 0 \\ q^*\sin\frac{\theta}{2} & (1-p)\sin\frac{\theta}{2}\cos\frac{\theta}{2} & (1-p)\sin^2\frac{\theta}{2} & 0 \\ 0 & 0 & 0 & 0 \end{pmatrix} \tag{4.19}$$

$$\hat{\rho}_S(t) = \text{Tr}_A\left[\hat{\rho}_{AS}(t)\right] = \begin{pmatrix} p & q\cos\frac{\theta}{2} \\ q^*\cos\frac{\theta}{2} & (1-p)\cos^2\frac{\theta}{2} \end{pmatrix} \tag{4.20}$$

Similar to $\hat{U}_{ADM}$ in Eq. (4.13), after renormalizing we get from comparison with Eq. (4.5) that $\sin^2\theta/2 = \mu = 1 - e^{-\gamma t}$, and so $\theta = 2gt = 2\arcsin\sqrt{1-e^{-\gamma t}}$.

4.1.4 Collision Model (Partial Swap)

The three descriptions above lead to a two-body interaction where the spin dissipates a part of it's energy onto an environment auxiliary. This idea is similar to a class of approaches known as collision models (CM). CM approximate the system–bath dynamics of open quantum systems by repeated two-body unitary collisions [85]. The most general collision between two qubits is described by the unitary matrix [85]

$$\begin{aligned}
\hat{C}(c_z, c, t) =& e^{-i2c_z t}\,|00\rangle\langle 00| + |11\rangle\langle 11| \\
& + \cos ct\,|10\rangle\langle 10| + |01\rangle\langle 01| \\
& - i\sin ct\hat{\sigma}^+\hat{\sigma}^- + \hat{\sigma}^-\hat{\sigma}^+ \\
=& \begin{pmatrix} e^{-i2c_z t} & 0 & 0 & 0 \\ 0 & \cos ct & -i\sin ct & 0 \\ 0 & -i\sin ct & \cos ct & 0 \\ 0 & 0 & 0 & e^{-i2c_z t} \end{pmatrix}
\end{aligned} \tag{4.21}$$

To recover the AD channel, we set $c_z = c/2$ [85]

$$\begin{aligned}
\hat{pS}(ct) = e^{-ict\hat{S}_n} =& \cos ct\mathbb{1} - i\sin ct\hat{S} \\
=& \begin{pmatrix} e^{-ict} & 0 & 0 & 0 \\ 0 & \cos ct & -i\sin ct & 0 \\ 0 & -i\sin ct & \cos ct & 0 \\ 0 & 0 & 0 & e^{-ict} \end{pmatrix}
\end{aligned} \tag{4.22}$$

Which is the special case of the two-qubit partial swap, with the swap operator $\hat{S} = \frac{1}{2}(\mathbb{1} + \hat{\sigma}_1 \cdot \hat{\sigma}_2)$.

Parameter c

To get the parameter c, we can compare the Kraus operators of our AD channel (Eq. (4.5)) to the Kraus representation of the collision map [85]

$$K_0 = e^{-c_z t}\,|0\rangle_S\langle 0| + e^{c_z t}\cos ct\,|1\rangle_S\langle 1| \tag{4.23}$$

$$K_1 = -ie^{c_z t}\cos ct\hat{\sigma}^- \tag{4.24}$$

The collision map evolves the density matrix of the spin of Eq. (4.5) according to

$$\hat{\rho}_S(t) = \begin{pmatrix} p\cos^2 ct & ce^{2ic_z t}\cos ct \\ q^* e^{-2ic_z t}\cos ct & (1-p) + p\sin^2 ct \end{pmatrix} \qquad (4.25)$$

Comparing that back to the Eq. (4.5) or (4.6), we see that we get the same action if we set $c_z = c/2$ and $ct = 2\theta = 2\arcsin\sqrt{\mu}$.

4.1.5   Comparison

As we saw, the (a) unitary dilation of Kraus operators, (b) AD matrix, (c) AD circuit, and (d) collision model all result in the same state of the spin $\hat{\rho}_S(t)$ when starting from $|0\rangle_A \langle 0| \otimes \hat{\rho}_S$ and resetting the auxiliary after the evolution. The question is whether it makes a difference which method one implements.

To get the circuits which implement the Kraus, AD matrix, and CM method, we use DoI. For the AD circuit (Fig. 4.1) we need to transpile into the native gate set of the Toronto hardware. The different circuit decomposition for the four methods are in Fig. 4.2.

The Kraus, AD matrix, and AD circuit (Fig. 4.2(a-c)) have very similar implementations, using two CX-gates and 15 or 16 single-qubit-gates. Interestingly, the collision model (Fig. 4.2(d)) decomposes into only nine single-qubit-gates at the cost of an additional CX-gate. This reduction of gates is offset by the fact that CX-gates add about one order of magnitude more noise than single-qubit-gates.

Going forward, we will use the AD circuit to describe the dissipation in our model, since it takes the least amount of gates, together with the Kraus description, with the advantage of being already described by a circuit originally (Fig. 4.1).

4.2   Results and Interpretation

We now focus on just the AD circuit and it's fidelity in implementing the amplitude damping channel. We set the open system parameter to $\gamma = 1$. A discussion of the choice of parameters follows for the full open spin-boson model in Sec. 6.1.

4.2.1   A Single Repetition of Dissipation

The AD circuit can be implemented directly, as it does not rely on any Trotterization. At each time-step, $CRY(\theta)$ is set to $\theta = 2\arcsin\sqrt{1 - e^{-\gamma t}}$ and the

(a) Kraus

(b) AD matrix

(c) AD circuit

(d) Collision model
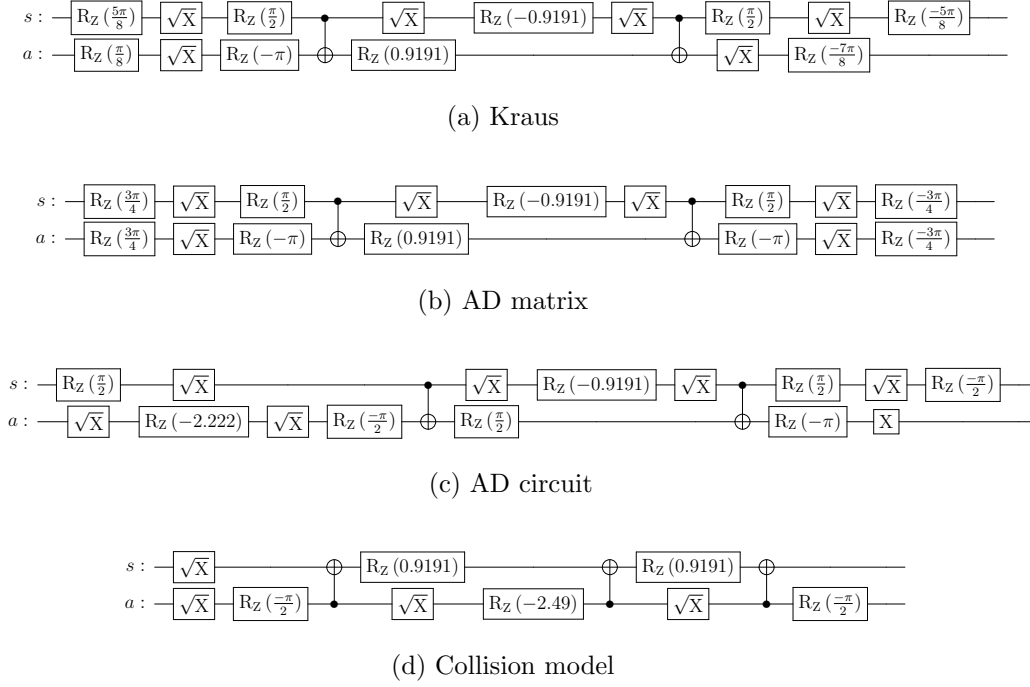
Figure 4.2: Circuits for four (equivalent) methods to model dissipation using a spin-auxiliary-interaction, transpiled onto the used quantum hardware. Gate values reflect $\gamma = t = 1$.

circuit (Fig. 4.1) is transpiled into the native gates (Fig. 4.2c) of the device. As the circuit only needs to be repeated once, the circuit depth stays constant at each time-step.

Fig. 4.3 considers one repetition of the AD circuit under noise. In panel (a), the exact simulation (solid line) is overlayed with markers for $\xi = 0.01$ (dots), $\xi = 0.1$ (triangles), $\xi = 1$ (pluses). Only for $\xi = 1$ there is a visible deviation from the exact predictions at the first few times-steps, where the dissipation is overestimated. Nevertheless, at all noise-levels, the amplitude damping channel is simulated to very high fidelity, see panel (b).

4.2.2 Multiple Repetitions of Dissipation

In chapter 6 we combine the dissipation with the unitary evolution to simulate the full open system. In between the unitary evolution, we will apply the dissipation for a short time-step Δt, requiring multiple repetitions of the dissipation. We thus now consider the case where we fix $\Delta t = 0.2$ in the AD circuit and copy it multiple times to reach a target time t.

As before we plot the evolution and infidelity in Fig. 4.4. We observe
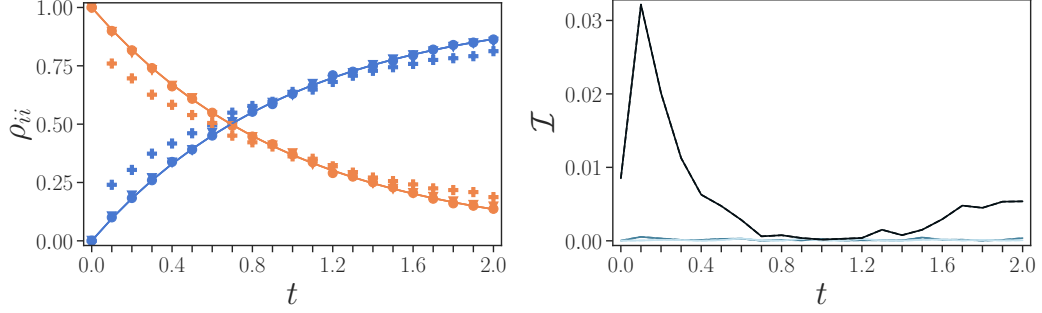
Figure 4.3: A single repetition of the AD circuit at different levels of noise. (a) Population of states. The solid lines are exact simulations, the markers show results of the circuit at $\xi = 0.01$ (dots), $\xi = 0.1$ (triangles), $\xi = 1$ (pluses). (b) Infidelity over time at $\xi = 0.01, 0.1, 1$ (lighter to darker lines). The dissipative rate is $\gamma = 1$.

an increased deviation and infidelity, most prominently at $\xi = 1$, due to the increased circuit depth.

In Fig. 4.4(c) we depict the scaling of the infidelity with the time-step size Δt. Lower Δt is better in all cases, and optimal at a single repetition $\Delta t = t$.

4.2.3 Noise from Gates

The noise in the gates leads itself to dissipation, even without the action of the gates. To model this we turn to the idea of gate folding. We keep the number and types of gates the same, but rearrange them such that their action is the identity $\mathbb{1}$. This results in just the natural noise acting on the circuit.

One circuit which approximately achieves this is depicted in Fig. 4.5. The original AD circuit (Fig. 4.2c) consisted of the gates {2 CX, 4 SX, 4 RZ} acting on the spin, {2 CX, 2 SX, 4 RZ, 1 X} acting on the auxiliary. To achieve the gate folding we use the formulas

$$CX \cdot CX = \mathbb{1} \tag{4.26}$$
$$RZ(\pi) \cdot RZ(\pi) \cdot RZ(\pi) \cdot RZ(\pi) = \mathbb{1} \tag{4.27}$$
$$SX \cdot SX \cdot SX \cdot SX = \mathbb{1} \tag{4.28}$$
$$X \cdot X = \mathbb{1} \tag{4.29}$$
$$SX \cdot SX \cdot X = \mathbb{1} \tag{4.30}$$

We rearranged the gates in such a way, that the spin idles while {1 SX, 1 RZ} act on the auxiliary in both circuits. On the hardware level RZ-gates can be
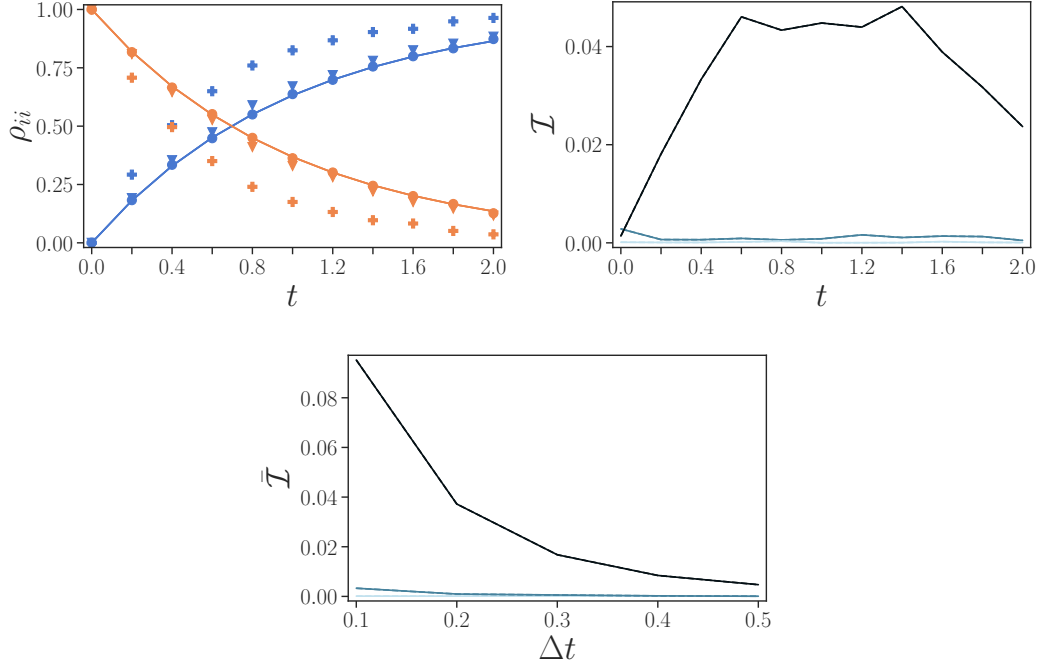
Figure 4.4:   Multiple repetitions of the AD circuit at different levels of noise. (a) Population of states. The solid lines are exact simulations, the markers show results of the circuit at $\xi = 0.01$ (dots), $\xi = 0.1$ (triangles), $\xi = 1$ (pluses). (b) Infidelity over time at $\xi = 0.01, 0.1, 1$ (lighter to darker lines). (c) Time-averaged infidelity at different time-step sizes Δt. The common open system parameter is $\gamma = 1$, time-step sizes in (a), (b) is $\Delta t = 0.2$.

implemented virtually, at zero time and no error [139]. Even though the RZ-gates are redundant in the folded circuit, we keep them for completeness. Note that X and SX share the same gate time. The barriers (dotted grey, vertical lines) are so that the gates won't be combined and removed by the classical transpiler.
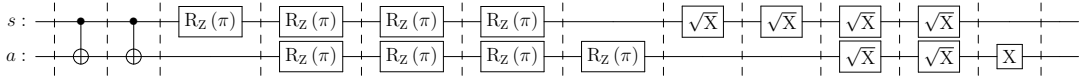
Figure 4.5: Gate folding of the AD circuit. Gates are rearranged s.t. the cancel and act as identity.

Results for the Folded Circuit

Fig. 4.6 depicts the evolution and infidelity of multiple repetitions of the folded AD circuit ($\Delta t = 0.2$) in current devices $\xi = 1$. The noiseless evolution (triangles) consists just of two straight lines, showing that indeed the folded circuit acts as identity. We observe that on the actual hardware (dots), the natural occurring noise somewhat models the amplitude damping channel.

This is in line with the previous observation, that the noisy AD circuit at the theoretical optimal $\theta = 2\arcsin\sqrt{1 - e^{-\gamma t}}$ overestimates the amplitude damping channel (see Figs. 4.3, 4.4). That opens up the possibility of finding a practically optimal value θ', depending on the level of noise and the time-step size, which is inversely proportional to the number of gates. Such an optimization could be interesting, but is beyond the scope of this work.
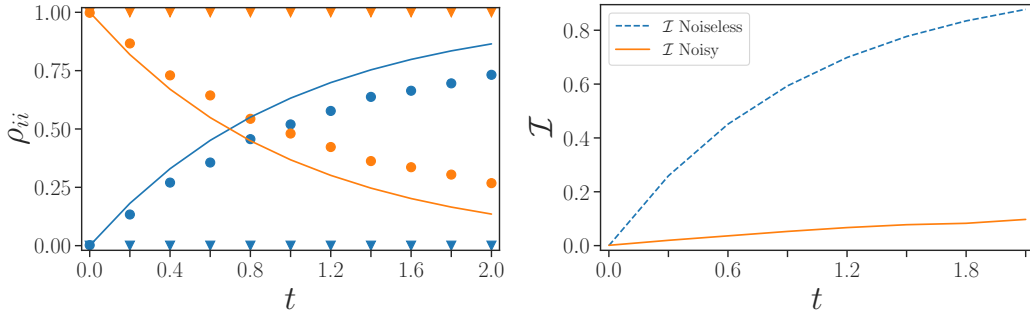
Figure 4.6: Dissipation coming from noise in the AD circuit. (a) Evolution when using gate folding at $\Delta t = 0.2$, $\xi = 1$ (b) Infidelity compared to exact $\gamma = 1$ simulations.

Chapter 5

Simulating the Hamiltonian

Before we turn to the full open system dynamics in Sec. 6, we evaluate how closely we can model the closed system Hamiltonian in noiseless simulations and on noisy hardware. To assess what affects the simulation error, we compare different integer-to-bit encodings and variations of the spin-boson Hamiltonian. In Sec. 5.1 we discuss qubit and gate requirements, and introduce a post-selection strategy with unary encoding. We then present the results in simulations in Sec. 5.2. In particular we consider theoretical errors that arise from Trotterization and practical errors due to noise in the quantum computer.

5.1 Encodings and Hamiltonians

5.1.1 Hamiltonians with different Interactions

When describing a physical system, there are always choices of Hamiltonians that represent different aspects of the system more faithfully. While we aim to simulate in the spin-boson model in Eq. (2.1), in this chapter we evaluate how the results are affected by a change to a related Hamiltonians.

More specifically we test two additional models with different interactions between the spin and the harmonic oscillator.

Jaynes-Cummings-Interaction

The Jaynes-Cummings-Interaction, like the spin-boson model, is a widely studied Hamiltonian to model the interaction between light and a two-level system.

$$\hat{H}_{JC-I} = \hbar\omega\hat{a}^\dagger\hat{a} + \frac{1}{2}(\hat{S}^z + \epsilon\hat{\sigma}^x) + \lambda(\hat{\sigma}^-\hat{a}^\dagger + \hat{\sigma}^+\hat{a}) \tag{5.1}$$

As with the spin-boson Hamiltonian $\hat{H}_{SB}$, we include the term $\frac{1}{2}\epsilon\hat{\sigma}^x$, which breaks the conservation of excitations. We are going to discuss the Jaynes-Cummings model without this $\hat{\sigma}^x$ term and the use of conservation laws in Sec. 7.

Z-Interaction

We also consider a variation, where the interaction is changed from $\hat{\sigma}^x$ to $\hat{\sigma}^z$

$$\hat{H}_{Z-I} = \hbar\omega\hat{a}^\dagger\hat{a} + \frac{1}{2}(\hat{S}^z + \epsilon\hat{\sigma}^x) + \lambda\hat{\sigma}^z\,(\hat{a}^\dagger + \hat{a}) \qquad (5.2)$$

so that the interaction depends on the orientation of the spin.

5.1.2 Boson-to-Qubit Encodings

When mapping bosons to qubits in Sec. 3.2.1, different integer-to-bit encodings result in different Pauli strings and ultimately in different representations of the Hamiltonian. While the mappings of the Hamiltonian are theoretically equivalent, their implementation and therefore the accuracy of simulation differ.

Unary Encoding

It was previously reported that unary encoding can lead to a reduction in the number of gates [95, 140, 141]. In the context of linear optical quantum computing unary encoding of single photons was used as an alternative to (Gaussian) boson sampling [142].

Another motivation is the possibility to use a post-selection strategy as a way of error mitigation. Due to device noise or limited accuracy in the implementation, most measurements do not represent a valid unary state, i.e. one measures $|1\rangle$ on more or less than exactly one qubit. These non-valid measurements can then be discarded.

On the flipside, unary requires significantly more qubits, as the number of qubits grows linearly with the dimension of the simulated Hilbert space, instead of logarithmically, as is the case with compact encodings.

When using unary encoding we cannot use quantum state tomography (QST) to calculate the density matrix and fidelity. Instead we use the MAE of the state probabilities $\mathcal{E}_{MA}$ (Eq. (3.15)) as an error measure.

Encoding the Harmonic Oscillator or the Full System

There are two interpretations of unary encoding that we consider. The first approach is to encode the harmonic oscillator but leave the spin un-encoded, as

we have done so far with standard binary and Gray code. The second variation is to use the unary encoding for the full combined Hilbert space of oscillator and spin $\mathcal{H}_{HO} \otimes \mathcal{H}_S$. We refer to both variations as 'unary' and 'full-unary', respectively.

5.1.3 Qubit and Gate Requirements

We first evaluate the difference in gate and qubit requirements, before considering noise in Sec. 5.2.

Qubit Requirements

The qubits required to realize the different encodings are compared in Fig. 5.1. Since only the harmonic oscillator is unary encoded , unary requires

$$N_Q = \log_2\left(dim(\mathcal{H}_S)\right) + dim(\mathcal{H}_{HO}) \tag{5.3}$$

qubits,. Full-unary encodes the harmonic oscillator and the spin, and thus the qubit number grows linearly with the total Hilbert space

$$N_Q = dim(\mathcal{H}_S) + dim(\mathcal{H}_{HO}) \tag{5.4}$$

Standard binary and Gray code both use qubits at optimal efficiency. If the number of harmonic oscillator levels is constant, the qubits as a function of spin number is the same in unary and in compact encodings. The qubit requirements for full-unary however increase rapidly with the system size, and can quickly become unfeasible. If one considers the use of unary, it is therefore useful to consider which sub-systems to encode.
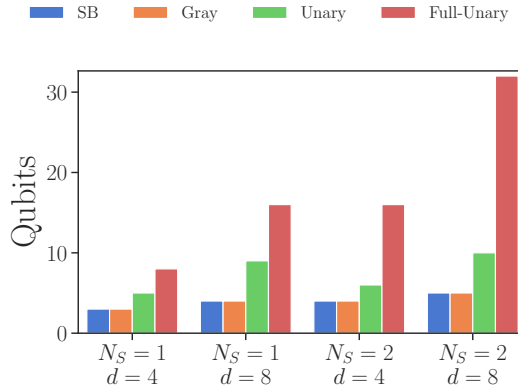
Figure 5.1: Qubit counts using different integer-to-bit encodings to implement the unitary $e^{-i\hat{H}_{SB}\Delta t}$.

Gate Requirements

The gate requirements to evolve one time-step of the trotterized unitary $e^{-i\hat{H}_{SB}\Delta t}$ and dissipation on the ibmq_jakarta device are listed in Fig. 5.2. This includes additional CX-gates to implement any necessary SWAP-gates, due to the limited qubit connectivity (Fig. 3.2). It is important to note that the number of gates can vary, since the transpiler uses a statistical process to map the circuit optimally to the qubit connectivity and the current calibration data of the hardware. In the cells marked n.a. our computer was unable to transpile the circuit, due to the high number of qubits $Q = 32$. While we only list the values for the spin-boson Hamiltonian, the same patterns hold for $\hat{H}_{Z-I}$ and $\hat{H}_{JC-I}$. The mapped Hamiltonians and their gate requirements can be found in Appendix B.

Even though an advantage in gate count was previously reported for different systems, unary (green) and full-unary (red) use significantly deeper circuits in the spin-boson Hamiltonian. We analyze whether or not unary and full-unary can still give an advantage due to a reduced Trotterization error and error mitigation via post-selection in Sec. 5.2.3.

Comparing the two compact encodings Standard binary (blue) and Gray code (orange) in Fig. 5.2, $\hat{H}_{SB}$ Gray code yielded fewer gates than standard binary in all cases for our Hamiltonian. Next to the encodings we also show the rapid scaling of gates with the number of qubits when using the exact DoI (gray), which we discussed in Sec. 3. We note that in terms of circuit depth, Gray code is optimal for our system.

5.2   Results and Interpretation

We now want to use the various encodings to simulate the respective unitary evolution of the three mentioned Hamiltonians. While the gate counts can give an approximation of the performance under noise, we are ultimately interested in the fidelity of the simulation.

Inaccuracies of the implementation on a quantum computer can arise from different causes. We first consider errors in the Trotterization of the evolution, which are also present in noiseless simulations. We then include errors due to the noise in the quantum computer.

For the Hamiltonian, we choose the parameters $\epsilon = 0.5$, $\omega = 4$, $\lambda = 2$ for one spin, and $\epsilon = 0.5$, $\omega = 6$, $\lambda = 2$ for two spins. We truncate the harmonic oscillator at four levels, which can be encoded with two qubits. For the initial state, we consider a pure product state between spins and bosons, with one spin in the excited state and zero excitations in the harmonic oscillator. Explicitly

N_S	d_{HO}	Trotter order	Standard Binary		Gray code		Isometric		Unary		full-unary	
			Single	CX	Single	CX	Single	CX	Single	CX	Single	CX
1	4	first	43	19	37	14	137	35	73	34	144	73
1	4	second	85	38	64	26			143	68	282	138
1	8	first	144	59	120	56	604	245	147	150	320	170
1	8	second	349	150	176	102			317	258	710	339
2	4	first	86	29	83	28	604	245	121	86	797	550
2	4	second	176	60	173	56			266	163	1492	1043
2	8	first	223	123	217	117	2631	1127	268	256	n.a.	n.a.
2	8	second	468	259	424	258			659	508	n.a.	n.a.

Figure 5.2:   Gate counts of integer-to-bit encodings in the spin-boson model. Both CX-gate and single-qubit gates to evolve one time-step of the unitary $e^{-i\hat{H}_{SB}\Delta t}$ on the jakarta device.

the initial state for the single and two spin case reads respectively

$$|\psi_{N_S=1}(t=0)\rangle = |S\rangle \otimes |B\rangle = |1\rangle \otimes |0\rangle \tag{5.5}$$

$$|\psi_{N_S=2}(t=0)\rangle = |S\rangle \otimes |B\rangle \otimes |S\rangle = |1\rangle \otimes |0\rangle \otimes |0\rangle \tag{5.6}$$

We choose these parameters to be the same for the final simulation of the open system later (Sec. 6), which we discuss and justify in Sec. 6.1.

5.2.1   Spin-Boson Model and Gray code

We first study the implementation of $\hat{H}_{SB}$ using Gray code, which we use for the open system simulations (Sec. 6).

Error from Trotterization

We start with the possible implementation error, without considering noise from the machine. In Fig. 5.3 we consider the unitary evolution of the Hamiltonian $\hat{H}_{SB}$ from Eq. (2.1) for a time step Δt. The solid and dashed lines compare the first- to the second-order Trotter formula. We observe a significant reduction of infidelity in the second-order method.
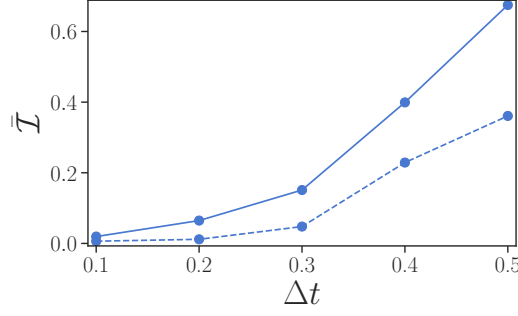
Figure 5.3: Trotterization error in the spin-boson model. Time-averaged infidelity for the evolution from $t = 0$ to $t = 2$ in noiseless simulations of the Hamiltonian. The solid and dashed lines are used for first-order and second order Trotter implementations respectively. The common parameters are $\epsilon = 0.5$, $\omega = 4$, $\lambda = 2$.

Infidelity under Noise

We now turn to noisy devices and ask which time-step size Δt achieves the highest fidelity $\mathcal{I}$.

In Fig. 5.3, for noiseless simulations, we observed that the infidelity increases monotonously with the time-step size Δt, and that a second order Trotterization is always preferred. In the presence of noise, however, an increased number of gates can lead to stronger noise effects, and thus instead of improving the quality of the simulations, it may result in worse fidelity. In Fig. 5.4(a) we consider different magnitudes of noise $\xi = 0.01$, 0.1, 1 (from lighter to darker colors) for either a first order Trotter step (continuous lines) or a second order Trotter step (dashed lines). We observe that for intermediate values of noise there is an optimal time interval Δt that corresponds to lowest infidelity, and that first order Trotterization can perform better at smaller Δt.

in Fig. 5.4(b) we show the general scaling of the infidelity with the level of noise. The blue line with circles depicts the time-averaged infidelity ($t = 0$ to $t = 2$), and the orange line with triangles infidelity at the final time. For simplicity second order Trotter at $\Delta t = 0.2$ is used throughout. We observe a logarithmic growth of infidelity with the noise-factor ξ.

5.2.2 Further Hamiltonians and Encodings

Continuing from Gray code and $\hat{H}_{SB}$, we compare the error rate to encodings standard binary, unary, and full-unary and the Hamiltonians with JC-type and Z-type interaction.
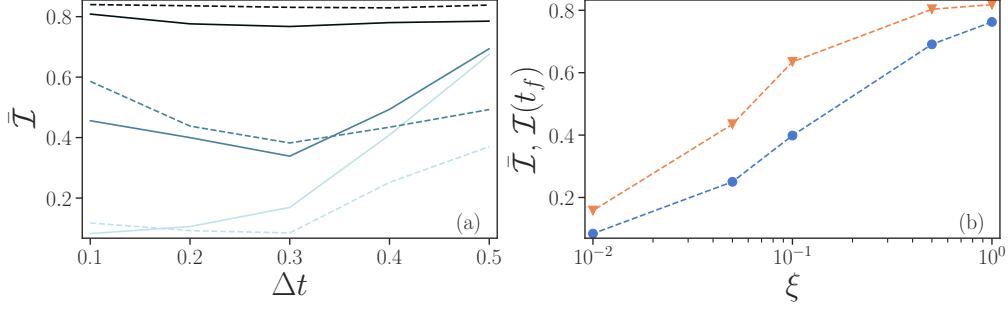
Figure 5.4: Error under noise in the spin-boson model. (a) Infidelity averaged over time as a function of time-step size Δt for an evolution from $t = 0$ to $t_f = 2$. Different noise levels $\xi = 0.01, \ 0.1, \ 1$ are represented by lighter to darker colors. (b) Time-averaged (blue circles) and final (orange triangles) infidelity as a function of noise levels. Here the final time is taken as $t_f = 2$, and we choose $\Delta t = 0.2$. In both panels, results from first-order and second-order Trotter implementations are represented by continuous and dashed lines respectively. Parameters are set to $\epsilon = 0.5$, $\omega = 4$, $\lambda = 2$.

Error in Trotterization

When using Trotter formulas, the error depends on the number of the terms in the Hamiltonian and on their commutation relations. In general, the accuracy increases for sparse Hamiltonians and the approximation becomes exact when all terms commute $[h_k, h_l] = 0$. On noisy hardware the number of gates required to realize all terms $e^{-ih_k \Delta t}$ becomes important, and depends on the number of qubits each term h_k acts on, as well as non-trivial cancellations of neighbouring gates [95].

In Fig. 5.5(a) we evaluate the infidelity in the Trotterization of the different Hamiltonians as a function of the time-step size Δt. The Jaynes-Cummings-interaction (orange line) results in the lowest infidelity, followed by the spin-boson Hamiltonian (blue line) and the Z-interaction (green line). The second-order Trotterization (dashed lines) has significantly smaller infidelity than a first-order formula (continuous lines). In Fig. 5.5(b) we consider the relative difference in infidelity $\bar{\mathcal{I}}_{rel}$ between the spin-boson model $\hat{H}_{SB}$ compared to $\hat{H}_{JC-I}$ and $\hat{H}_{Z-I}$ for first-order Trotterization.

$$\bar{\mathcal{I}}_{rel} = |\bar{\mathcal{I}}_{SB} - \bar{\mathcal{I}}_{(\cdot)}|/\bar{\mathcal{I}}_{SB} \tag{5.7}$$

For $\Delta t \approx 0.3$ the relative difference reaches $> 40\%$ between $\hat{H}_{SB}$ and $\hat{H}_{JC-I}$ (blue line), and $> 30\%$ between $\hat{H}_{SB}$ and $\hat{H}_{Z-I}$ (orange line). We conclude that the Trotterization error can be impacted significantly by the choice of Hamiltonian.
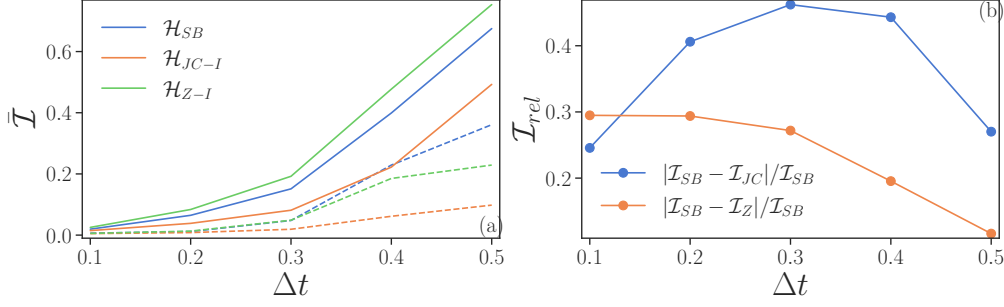
Figure 5.5: Trotterization error in other Hamiltonians. Time-averaged infidelity for noiseless simulations from $t = 0$ to $t = 2$ of different Hamiltonians. (a) Spin-boson Hamiltonian in blue, Jaynes-Cummings-interaction in orange, Z-interaction in green. The solid and dashed lines are used respectively for first-order and second order Trotter implementations. (b) Relative difference in infidelity $\mathcal{I}_{rel}$ between the spin-boson Hamiltonian and the Jaynes-Cummings-/Z-interaction Hamiltonian. The common parameters are $\epsilon = 0.5$, $\omega = 4$, $\lambda = 2$.

Error under Noise

In Fig. 5.6 the time-averaged MAE for various combinations of encodings and Hamiltonians at different levels of noise is depicted. Since we include unary and full-unary, we use the MAE instead of the infidelity for all encodings. The results for unary and full-unary make use of post-selection to reduce the error.

In the low to medium noise regime (Fig. 5.6(a-b)) unary and full-unary perform significantly better than the compact encodings for all Hamiltonians. Even though unary and full-unary use more gates, at low levels of noise the reduced Trotterization error and the post-selection result in a net advantage. Comparing the compact encodings, Gray code generally performs slightly better than standard binary.

Between the different Hamiltonians the error rate can vary up to 20% at a given encoding and noise level. When using Gray code we observe the lowest error for $\hat{H}_{SB}$, although no clear picture emerges to definitively conclude which Hamiltonian is the easiest to simulate. In general the optimal encoding depends on the level of noise and the studied Hamiltonian.

5.2.3 Unary Encoding

We observed a significantly lower error when using unary encodings at lower levels of noise. Next we study the effect of post-selection as an error mitigation technique more closely.

Fig. 5.7 compares the MAE with (solid) and without (dashed) post-selection.

(a) $\xi = 0.01$ (b) $\xi = 0.1$ (c) $\xi = 1$

■ SB   ■ Gray   ■ Unary   ■ Full-Unary
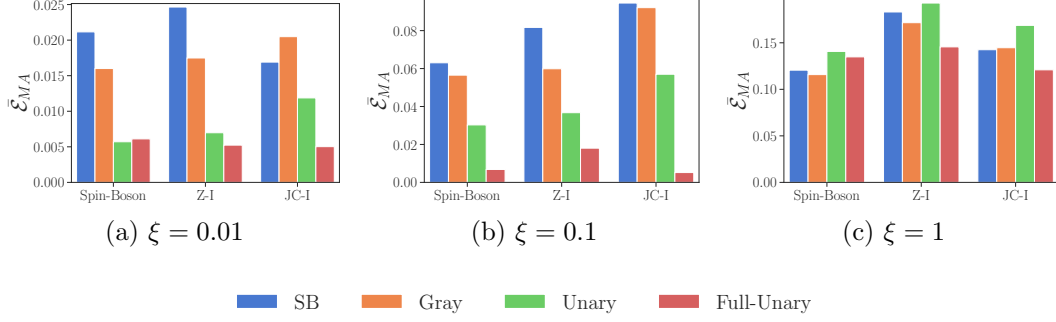
Figure 5.6: Error under noise in other Hamiltonians. Time-averaged MAE $\bar{\mathcal{E}}_{MA}$ of different encodings and Hamiltonians at noise-levels $\xi = 0.01, 0.1, 1$. First order Trotter at $\Delta t = 0.2$. Parameters are $\epsilon = 0.5$, $\omega = 4$, $\lambda = 2$.

Unary (Fig. 5.7(a)) and full-unary (Fig. 5.7(b)) show very similar behaviour. At all levels of noise, there is a notable improvement when using post-selection.
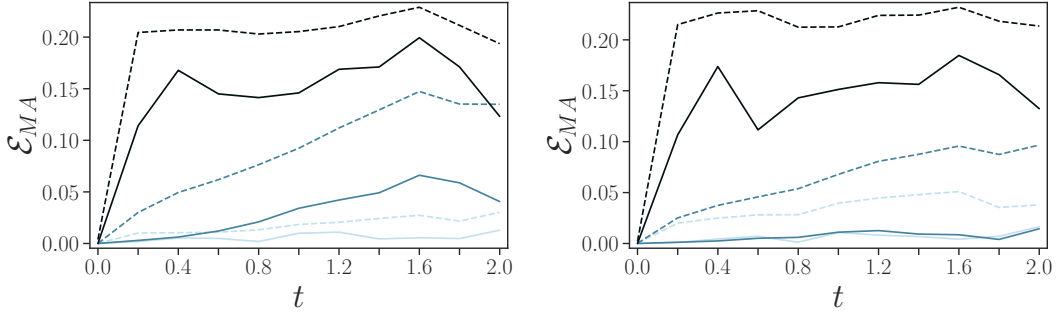
Figure 5.7: Post-selection in unary encoding. MAE $\mathcal{E}_{MA}$ with (solid lines) and without (dashed lines) using post-selection for error mitigation when using (a) unary (b) full-unary encoding. Different noise levels $\xi = 0.01$, 0.1, 1 are represented by lighter to darker colors. Parameters are $\epsilon = 0.5$, $\omega = 4$, $\lambda = 2$.

In Fig. 5.8 we combine the evolution using post-selection with the relative number of measurements which were kept (not discarded) in the post-selection process. We define the post-selection-ratio as

$$\mathcal{R}_{ps} = \frac{M_{total} - M_{discarded}}{M_{total}} \tag{5.8}$$

Again, unary (Fig. 5.8(a)) and full-unary (Fig. 5.8(b)) show near identical behaviour. As the error (solid lines) increases with time, so does the number of discarded measurements (dotted lines). While for $\xi = 0.01$, 0.1 the change

is more or less linear, it is more abrupt for $\xi = 1$, signifying that the noise quickly dominates and saturates the error. We observe that the discarded measurements grow proportionally to the calculated error in all cases.
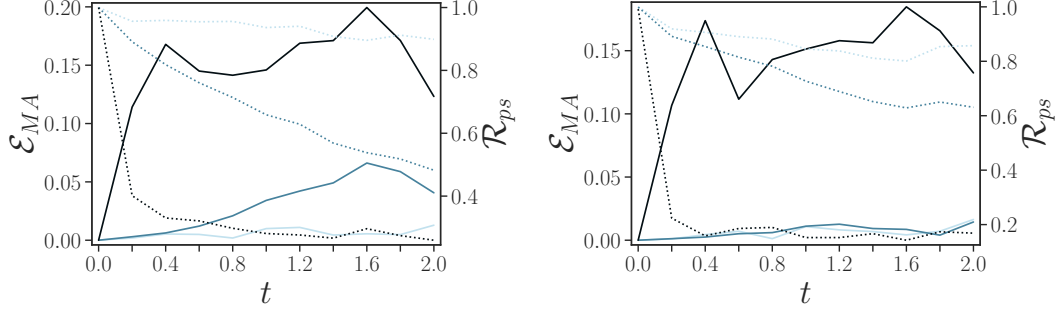
Figure 5.8: Rate of post-selection in unary encoding. MAE $\mathcal{E}_{MA}$ (solid lines) and the post-selection-ratio $\mathcal{R}_{ps}$ (dotted lines) when using (a) unary (b) full-unary encoding. Different noise levels $\xi = 0.01,\ 0.1,\ 1$ are represented by lighter to darker colors. All use first-order Trotter at $\Delta t = 0.2$. Parameters $\epsilon = 0.5,\ \omega = 4,\ \lambda = 2$.

Chapter 6

Simulating the Open Spin-Boson Model

Until now, we studied the unitary and dissipative evolution separately in chapters 4 and 5. We now want to combine both to simulate the dynamics of the open spin-boson model.

6.1 Model Parameters

In the previous chapters 4 and 5 we already used system parameters, for which we now provide our reasoning.

Previously and going forward, we set the dissipative rate $\gamma = 1$, and used $\epsilon = 0.5$, $\omega = 4$, $\lambda = 2$ and $\epsilon = 0.5$, $\omega = 6$, $\lambda = 2$ as parameters for the hamiltonian in the single and two spin case. As the initial state, we consider a pure product state, with one spin in the excited state and zero excitations in the harmonic oscillator.

6.1.1 Dissipative Rate

In Fig. 6.1(a-c) we compare the observables in the single spin case at different dissipation parameters γ. With higher γ the oscillations in $\langle \hat{n} \rangle$, $\langle \hat{S}^z \rangle$, $\langle \hat{S}^x \rangle$ increasingly flatten out. For $\gamma \geq 1$ the effect of dissipation is clearly visible.

The correlations between two spins as a function of γ is depicted in Fig. 6.1(d, f). At higher levels of dissipation the coherence between the two spins are increasingly suppressed, but at $\gamma = 1$ there are still measurable correlations.

We choose $\gamma = 1$, so that the dynamics differ significantly from the closed system $\gamma = 0$ case, but there are still meaningful correlations between the two spins.
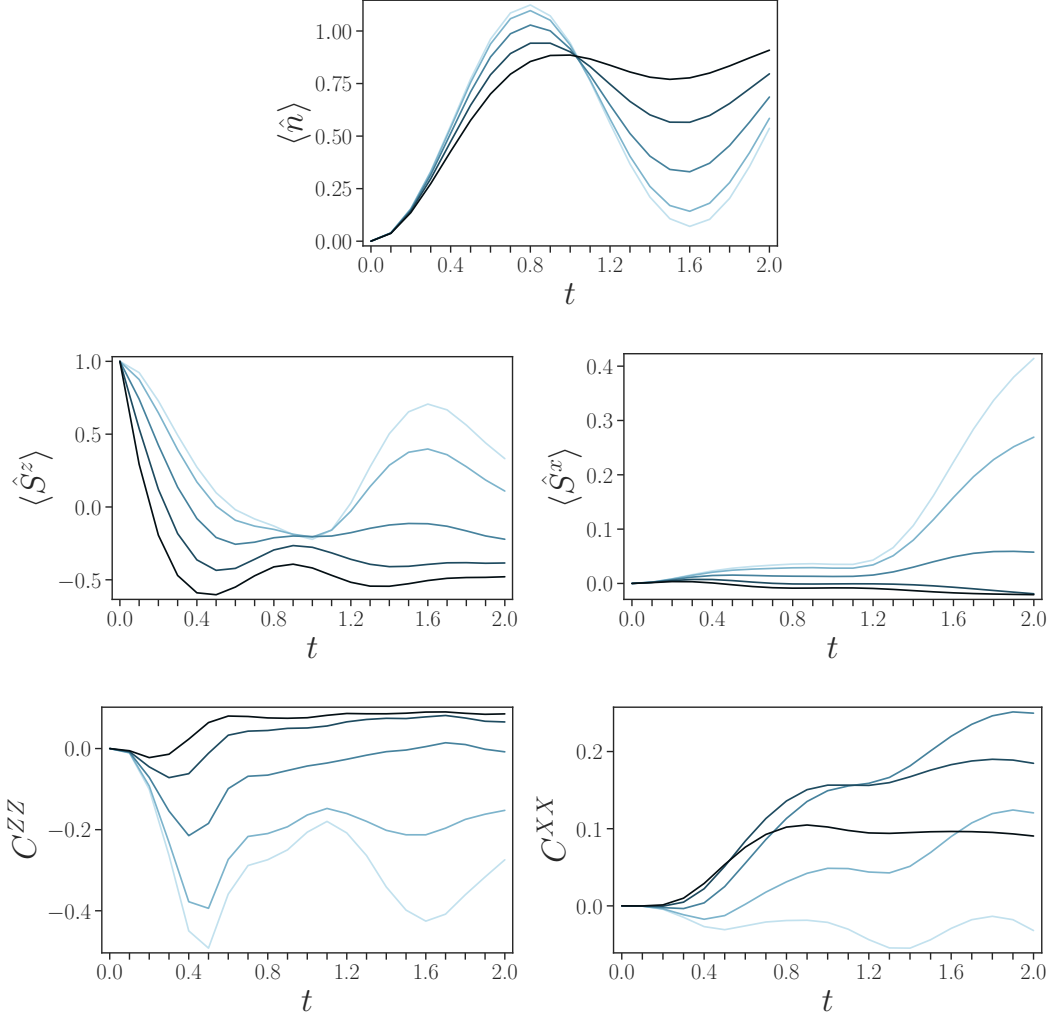
Figure 6.1: Noiseless simulations of the open system at different dissipation parameters γ. (a) Average harmonic oscillator occupation $\hat{n}$ (b) $\hat{S}^z$ (c) $\hat{S}^x$ (d) C^{ZZ} (e) C^{XX} Lighter to darker colors represent $\gamma = 0$, 0.5, 1.0, 1.5, 2.0. The common parameters are $\epsilon = 0.5$, $\omega = 4$, $\lambda = 2$.

6.1.2 Truncation of the Harmonic Oscillator

In Sec. 5.2, and continuing here, we already truncated the harmonic oscillator at $d_{HO} = 4$ and used Gray code as an integer-to-bit mapping.

We want to use a compact encoding, so that we can efficiently use the full Hilbert Space to encode $d_{HO} = 2^{Q_B}$ harmonic oscillator levels on Q_B qubits. Comparing the compact encodings standard binary and Gray code, Gray code is preferable as it requires less gates in all cases (Fig. 5.2).

We saw that an increase of the levels of the harmonic oscillator increases

the qubit and gate count (Fig. 5.2). To keep the gate depth low, we choose $d_{HO} = 4$ on $Q_B = 2$ qubits. To see weather or not the cutoff at $d_{HO} = 4$ is justified, we will identify if $d_{HO} = 4$ captures the dynamics of the system by comparing it to $d_{HO} = 8$.

Figs. 6.2, 6.3, 6.4 depict the dynamics and observables at different truncation levels $d_{HO} = 4$ and $d_{HO} = 8$ for one and two spins in exact simulations.

For one spin the dynamics, as well as $\langle \hat{n} \rangle$, $\langle \hat{S}^z \rangle$, and $\langle \hat{S}^x \rangle$ match qualitatively. Although there are small quantitative differences for the dynamics, $\langle \hat{n} \rangle$, and $\langle \hat{S}^z \rangle$.

For two spins $d_{HO} = 4$ and $d_{HO} = 8$ differ more. While the dynamics and observables still match qualitatively, there are more significant quantitative differences. The dynamics of some states, $\langle \hat{n} \rangle$, and the correlations C^{ZZ}, C^{XX} show the largest deviations.

For a quantitatively accurate treatment, eight levels in the harmonic oscillator are necessary. Nevertheless, a reasonably precise evolution of the system up to a time $t = 2$ can be obtained by considering simply four levels for the harmonic oscillator.

6.2   Results for the One Spin System

We now turn to implementing the open system simulations on quantum hardware.

We will first consider errors that raise from the Trotterization of the evolution in Sec. 6.2.1. We will then consider errors due to the noisy nature of the quantum computer in Sec. 6.2.2. In Sec. 6.3 we will then study the case of two spins coupled to the harmonic oscillator.

6.2.1   Error from Trotterization

As explained earlier, to implement the open dynamics we Trotterize the unitary and dissipative parts of the master equation. However, also for the implementation of the unitary evolution we need to rely on another layer of Trotterization.

We first consider both layers of Trotterization. In Fig. 6.5(a) we evaluate the infidelity both for unitary and dissipative evolutions versus Δt, i.e. following Eq. (2.4) for $\gamma = 0$ (blue lines with circles) or $\gamma = 1$ (orange lines with triangles). We observe that the second-order Trotterization, dashed lines, has significantly smaller infidelity than a first-order implementation, continuous lines. Interestingly, beyond $\Delta t \approx 0.3$, the infidelity in just the Hamiltonian simulation is larger than the infidelity when including the dissipation. Furthermore, independently on whether one considers first-order or second-order

Figure 6.2: Dynamics and observables of an one spin system at different truncation levels of the harmonic oscillator. Dynamics at (a) $d_{HO} = 0, \ldots, 3$ and (b) $d_{HO} = 0, \ldots, 7$. Observables at both cutoffs (c) average bosonic occupation $\langle \hat{n} \rangle$ and spin-z $\langle \hat{S}^z \rangle$ (d) spin-x $\langle \hat{S}^x \rangle$. Solid lines for $d_{HO} = 4$, dashed lines for $d_{HO} = 8$. Parameters are $\epsilon = 0.5$, $\omega = 4$, $\lambda = 2$, $\gamma = 1$.

Trotterization, the dissipative dynamics have either smaller infidelities or are very close to the unitary case.

In Fig. 6.5(b) we now implement the unitary evolution perfectly using DoI instead of a Trotter formula, such that the only Trotterization is the separation of unitary and dissipative parts. Lighter to darker dotted lines show dissipation rates $\gamma = 0, \ldots, 2.5$. We see that larger dissipation rate γ corresponds to larger infidelities. However, the main message is that for $\gamma = 1$ the infidelity simply from the Hamiltonian evolution (Fig. 6.5(a)) is one order of magnitude larger than the contribution from dissipation (Fig. 6.5(b)). This implies that the unitary is the main contribution to the infidelity.

6.2.2 Error in Presence of Noise
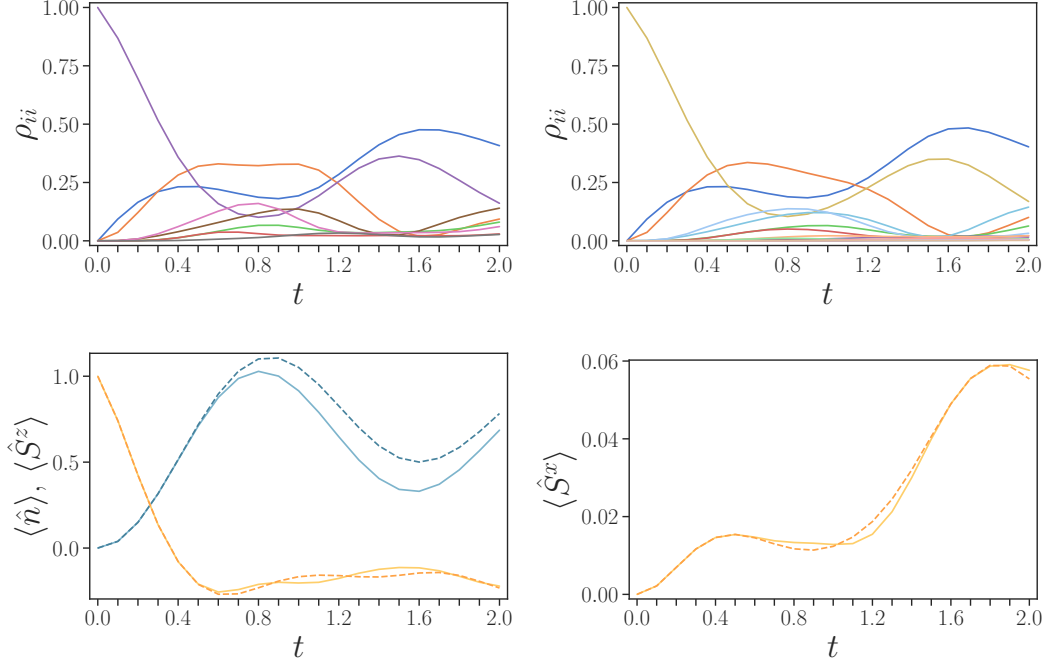
We now turn to more realistic, and thus noisy, devices.
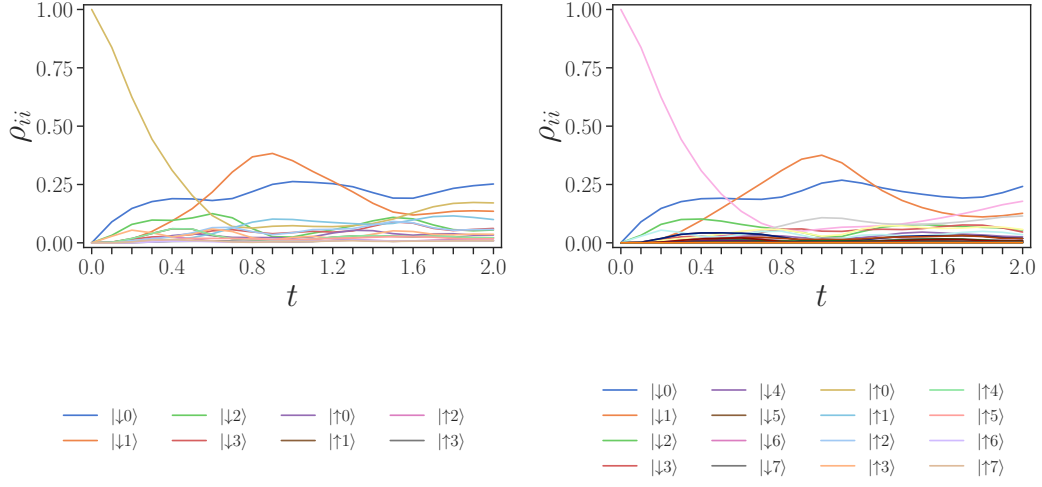
Figure 6.3: Dynamics of a two spin system at different truncation levels of the harmonic oscillator. Dynamics at (a) $d_{HO} = 0, \ldots, 3$ and (b) $d_{HO} = 0, \ldots, 7$. Parameters are $\epsilon = 0.5$, $\omega = 6$, $\lambda = 2$, $\gamma = 1$.

Optimal Trotter-Step-Size

In Fig. 6.5, for noiseless simulations, we observed that the infidelity increases monotonously with the time-step size Δt, and that a second-order Trotterization is always preferred. In the presence of noise, however, an increased number of gates can lead to stronger noise effects, and thus instead of improving the quality of the simulations, it may result in worse fidelity. In Fig. 6.6(a) we thus consider evolution of the full model, unitary and dissipative part, up to a time $t = 2$ for different magnitudes of noise $\xi = 0.01$, 0.1, 1 (from lighter to darker colors) for either a first-order Trotter step (continuous lines) or a second-order Trotter step (dashed lines). In particular we depict the infidelity versus the length of the time step Δt. We observe that for intermediate values of noise there is an optimal time interval Δt that corresponds to lowest infidelity, and that first-order Trotterization can perform better at smaller Δt.

Infidelity under Noise

We now consider the open system dynamics case. The impact of noise on fidelity is depicted in Fig. 6.6(b). Here we show both the average infidelity over the time interval from $t = 0$ to $t = 2$ (blue line with circles), and the infidelity at the final time (orange line with triangles). We consider exclusively a second-order Trotter decomposition and a time step $\Delta t = 0.2$. Fig. 6.6(b) indicates a monotonous growth of infidelity with the noise-factor ξ, for the
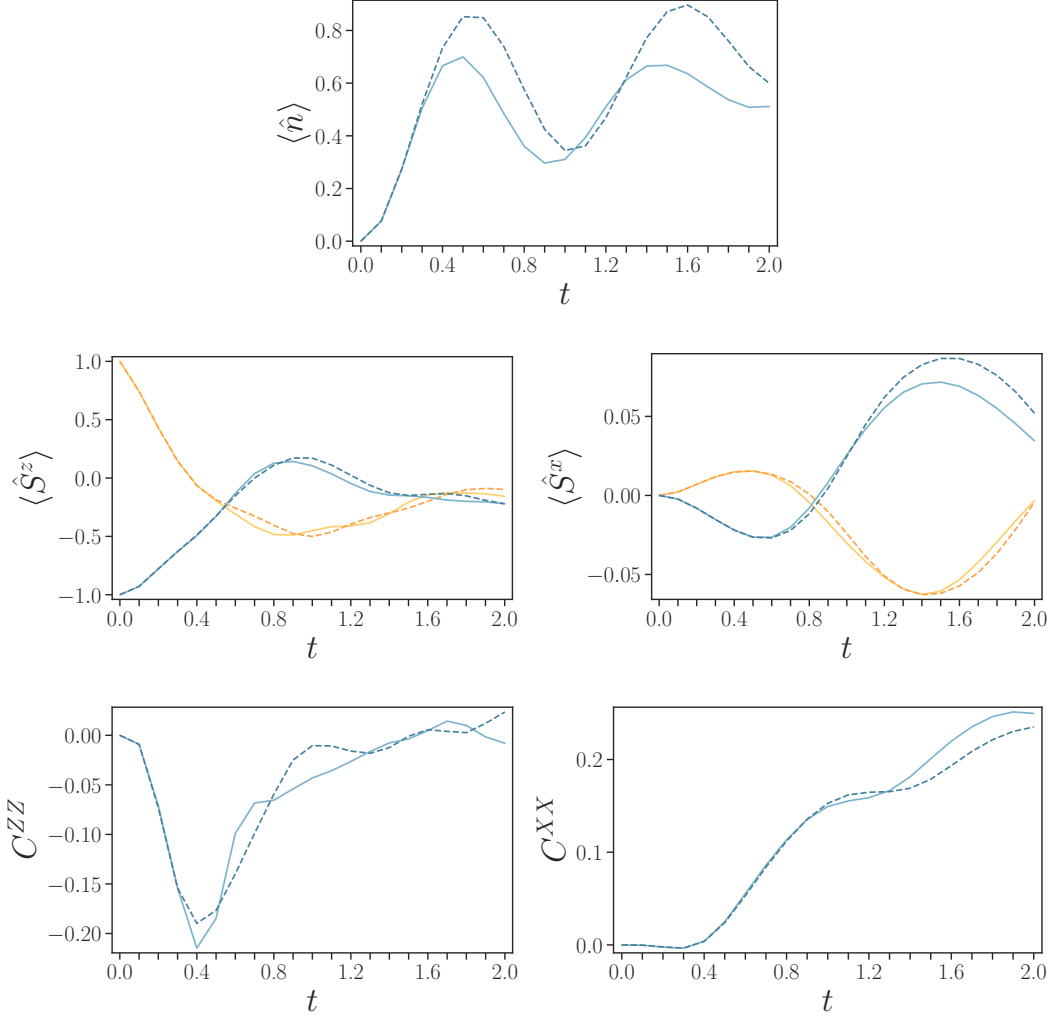
Figure 6.4: Observables of a two spin system at different truncation levels of the harmonic oscillator. (a) Average bosonic occupation $\langle \hat{n} \rangle$ (b) spin-z $\langle \hat{S}^z \rangle$ (c) spin-x $\langle \hat{S}^x \rangle$ (d) spin-z connected correlation C^{ZZ} (e) spin-x connected correlation C^{XX}. Solid lines represent $d_{HO} = 0, \ldots, 3$, dashed lines $d_{HO} = 0, \ldots, 7$. In (b) and (c) yellow lines are for the first spin, blue lines for the second spin. Parameters $\epsilon = 0.5$, $\omega = 6$, $\lambda = 2$, $\gamma = 1$.

parameters explored.

Infidelity over Time

In Fig. 6.7 we show the infidelity versus time for first-order (solid lines) and second-order (dashed line) Trotterizations, while $\Delta t = 0.2$. We observe that only for small values of ξ one would prefer a second-order Trotterization to
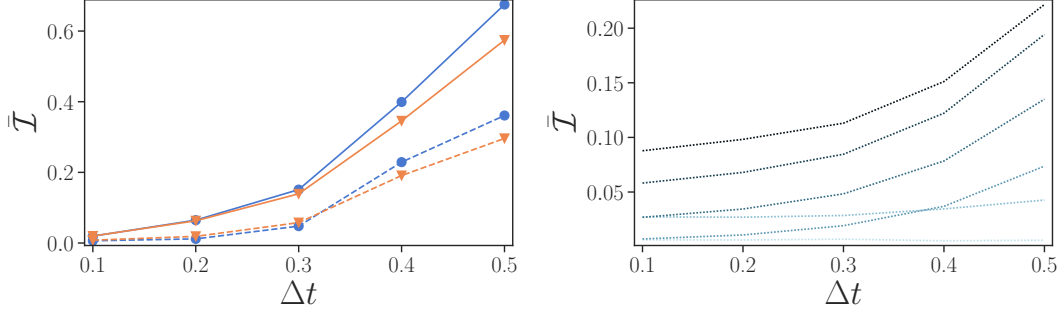
Figure 6.5: Time-averaged infidelity for the evolution from $t = 0$ to $t = 2$. (a) Noiseless simulations of the Hamiltonian $\gamma = 0$ (blue line, dots) and the open system $\gamma = 1$ (orange line, crosses). The solid and dashed lines are used respectively for first-order and second-order Trotter implementations. (b) Noiseless simulations of the open system at various dissipation rates, using an exact implementation of the Hamiltonian with DoI. $\gamma = 0, \ldots, 2.5$ correspond to lighter to darker dotted lines. The common parameters are $\epsilon = 0.5$, $\omega = 4$, $\lambda = 2$.
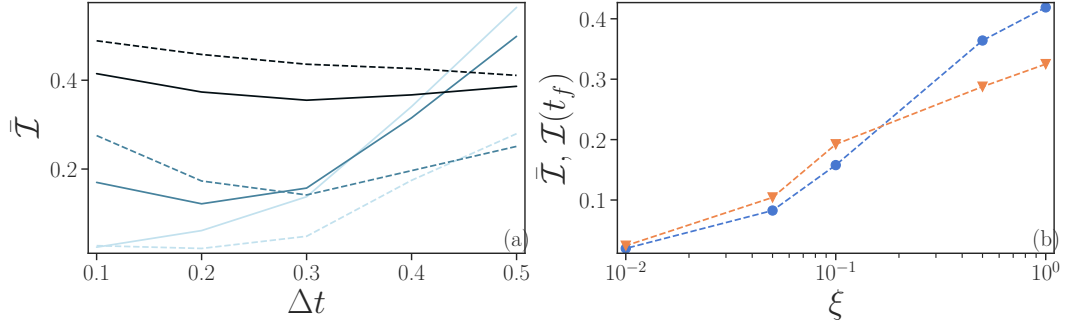
Figure 6.6: (a) Infidelity averaged over time as a function of time-step size Δt for an evolution from $t = 0$ to a final time $t_f = 2$. Different noise levels $\xi = 0.01,\ 0.1,\ 1$ are represented by lighter to darker colors. (b) Time-averaged (blue circles) and final (orange triangles) infidelity as a function of noise levels at $\Delta t = 0.2$. In both panels, results from first-order Trotter implementations are represented by continuous lines, while second-order by dashed lines. Parameters $\epsilon = 0.5$, $\omega = 4$, $\lambda = 2$, $\gamma = 1$.

improve on the fidelity of the states. We note, not shown here, that for $\xi = 0.01$ the dynamics are almost identical to the noiseless case.
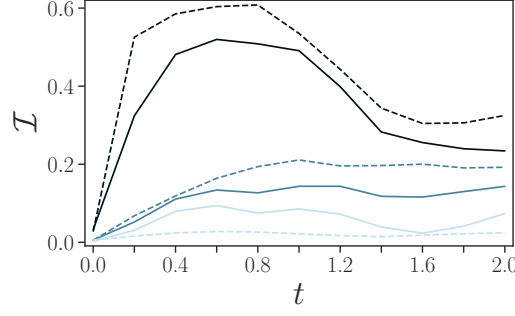
Figure 6.7: Infidelity as a function of time in open system simulation in presence of noise. Using first-order Trotter (solid) and second-order Trotter (dashed) at $\Delta t = 0.2$. At noise-factor $\xi = 0.01$, 0.1, 1 (from lighter to darker colors). Other parameters are $\epsilon = 0.5$, $\omega = 4$, $\lambda = 2$, $\gamma = 1$.
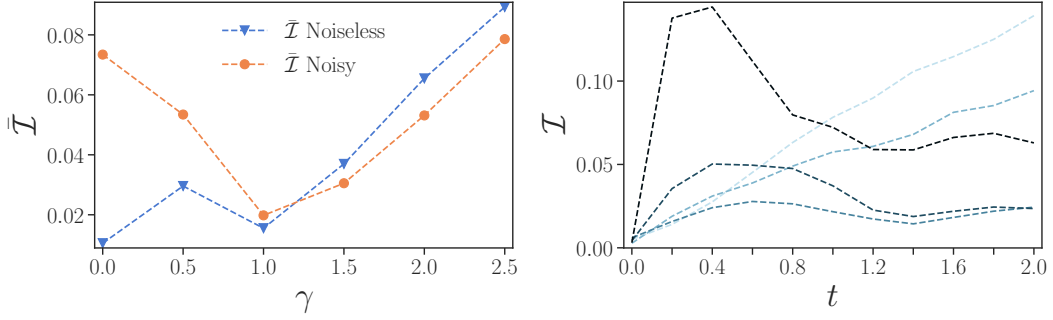
Figure 6.8: Dissipative rate under noise. (a) Infidelity averaged over time versus dissipative rate γ with noise $\xi = 0.01$ (orange line with circles) and without noise (blue line with triangles). (b) Infidelity as a function of time $\gamma = 0$, 0.5, 1, 1.5, 2, 2.5 (from lighter to darker colors). Second-order Trotter at $\Delta t = 0.2$ and the other parameters are $\epsilon = 0.5$, $\omega = 4$, $\lambda = 2$.

6.2.3 Dissipative Rate under Noise

To better understand the role of dissipation, we aim to verify its effect on the accuracy of the simulation. To focus specifically on the role of γ, we consider only a second-order Trotter evolution, a fixed value of $\Delta t = 0.2$ and $\xi = 0.01$, where the simulation of the quantum computer shows generally better performance.

Fig. 6.8(a) we plot the time-averaged infidelity at different values of γ, with (orange line with circles) and without noise (blue line with triangles). At higher values of γ the infidelity of the noisy quantum computer is lower than the noiseless simulations. While we only show $\xi = 0.01$, the same behaviour holds for $\xi = 0.1$.

In Fig. 6.8(b) we plot the infidelity versus time for different values of the dissipative rate γ. We observe two regimes in terms of γ. For $\gamma \leq 1$ the infidelity tends to increase with time, while for larger values of γ, the infidelity can decrease after an initial time.

The infidelity depending on γ in current devices ($\xi = 1$) is shown in Fig. 6.9. While the noisy results do not improve on the noiseless simulations at any γ (Fig. 6.9(a)), the regime around $\gamma = 3$ leads to greatly reduced infidelity (Fig. 6.9(b)). To better understand this behaviour at $\gamma = 3$, we compare the exact (Fig. 6.9(c)) to the noisy $\xi = 1$ simulations (Fig. 6.9(d)). We observe that the exact evolution quickly stagnates, predominantly with no excitations in the spin or harmonic oscillator (blue line). We attribute this to the strong rate of dissipation. Similarly the natural dissipation due to noise on quantum hardware leads to qubits in the $|\downarrow\rangle$ state, which closely mimics the exact behaviour.

It thus occur that the intrinsic dissipative dynamics can, in some regimes, be better represented on a noisy device.

6.2.4 Observables

We examine the evolution of the spin in Fig. 6.10. It depicts the expectation values of $\hat{\sigma}^z$ (panel (a)) and $\hat{\sigma}^x$ (panel (b)) of the spin versus time. In both panels the blue dotted line corresponds to the exact values and lighter to darker shaded lines to noiseless and $\xi = 0.01$, 0.1, 1. Solid lines are used for first-order Trotterizations, while dashed lines for second-order. For each noise level ξ we have used the Trotterization order which corresponds to the lower fidelity.

In the exact reference in Fig. 6.10(b) the value of $\hat{\sigma}^x$ grows slightly over time to < 0.1. However on current hardware ($\xi = 1$) we observe a significant rise in $\hat{\sigma}^x$. We consider this behaviour in more detail in Sec. 6.3.2.

Instead, the simpler evolution of $\hat{\sigma}^z$ is captured fairly well also for the different values of ξ. We hypothesize that the dissipation of the spin in the exact model is mimicked by the thermal relaxation of the spin-qubit on the noisy device. This observation aligns with the previous conclusion that dissipative dynamics can be well modelled by itself dissipative hardware.

Harmonic Oscillator under Noise

Fig. 6.11(a) depicts the average occupation in the harmonic oscillator for $d_{HO} = 4$ levels. The oscillatory evolution of the occupation of the harmonic oscillator is captured, only partially, with the smaller non-zero noise parameter considered $\xi = 0.01$, while the occupation of the harmonic oscillator at
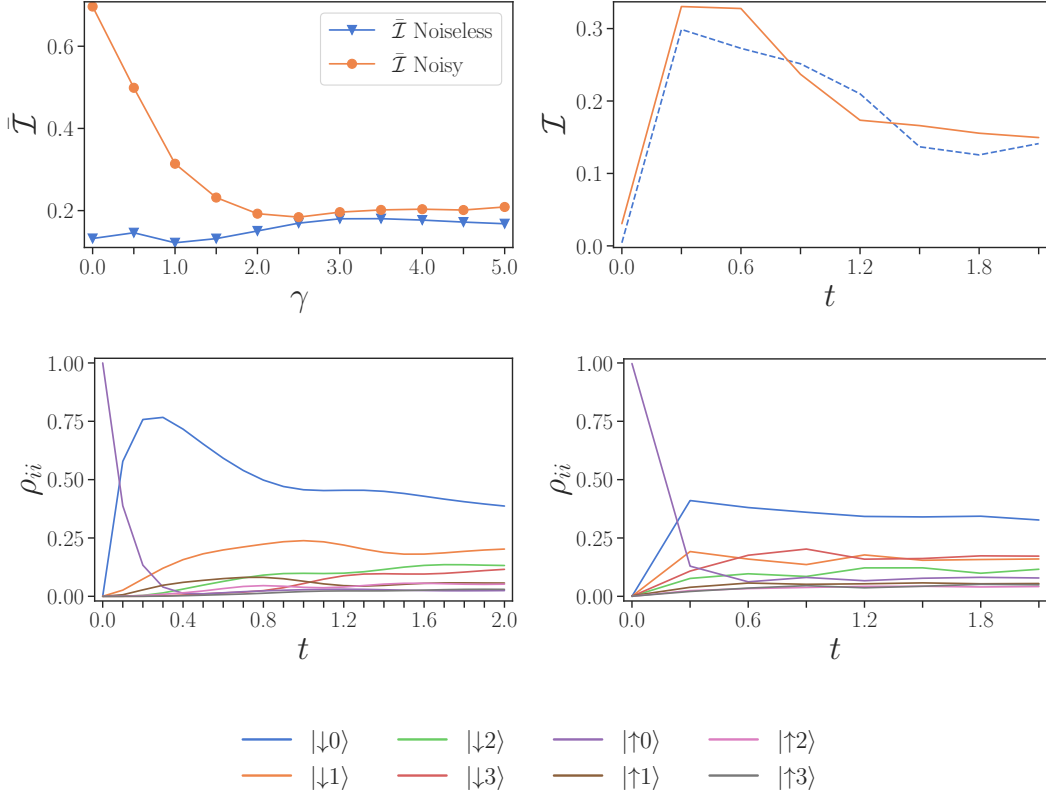
Figure 6.9: Dissipative systems can be easier to simulate. (a) Time-averaged infidelity at different dissipative rates γ. (b) Infidelity over time (c) exact evolution (d) evolution under noise, all at $\gamma = 3$ (a), (b), (d) using 1st order Trotter with $\Delta t = 0.3$ at full noise $\xi = 1.0$. Common parameters are $\epsilon = 0.5$, $\omega = 4$, $\lambda = 2$, $\gamma = 3$.

$\xi = 1$ quickly stagnates at around a value of 1. It seems that the average bosonic occupation $\langle \hat{n} \rangle$ increases with the presence of noise. In Fig. 6.11(b) we compare $d_{HO} = 4$ (a) to $d_{HO} = 8$ (b), to see how the available levels of the harmonic oscillator affect $\langle \hat{n} \rangle$. We observe that in the case of a more noisy setup (darker colors), including higher levels for the harmonic oscillator would result in higher average occupation $\langle \hat{n} \rangle$.

We hypothesize that due to noise all possible states are realized, including states which correspond to higher levels of the harmonic oscillator and are only sparsely occupied in the exact simulations. The probability of a physical state under noise is biased by the qubit state representing the physical state. For example, the qubit state $|\downarrow\downarrow\rangle$ (representing $\hat{n} = 0$) is more likely than $|\uparrow\uparrow\rangle$ (representing $\hat{n} = 3$), due to thermal relaxation. The state probabilities under
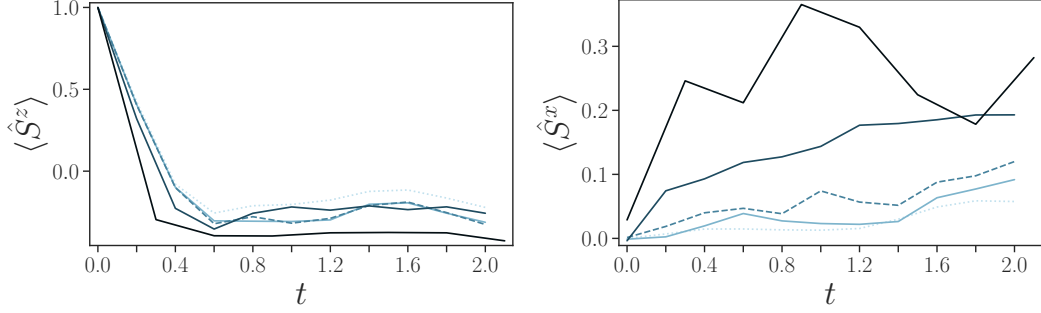
Figure 6.10: Expectation values for one spin on noisy hardware. (a) Spin-z $\langle \hat{S}^z \rangle$ (b) spin-x $\langle \hat{S}^x \rangle$ as function of time. Different noise levels $\xi = 0.01$, 0.1, 1 are presented, respectively by lighter to darker colors. As a reference, exact simulations are depicted by the blue dotted lines. Results obtained using first-order Trotterization are with solid lines, while second-order with dashed lines. Other parameters are $\epsilon = 0.5$, $\omega = 4$, $\lambda = 2$ and $\gamma = 1$.

noise are discussed in Sec. 6.2.5 and Fig. 6.12.

Thus including a number of available levels when choosing a truncation can cause a higher average occupation $\langle \hat{n} \rangle$ in presence of noise.
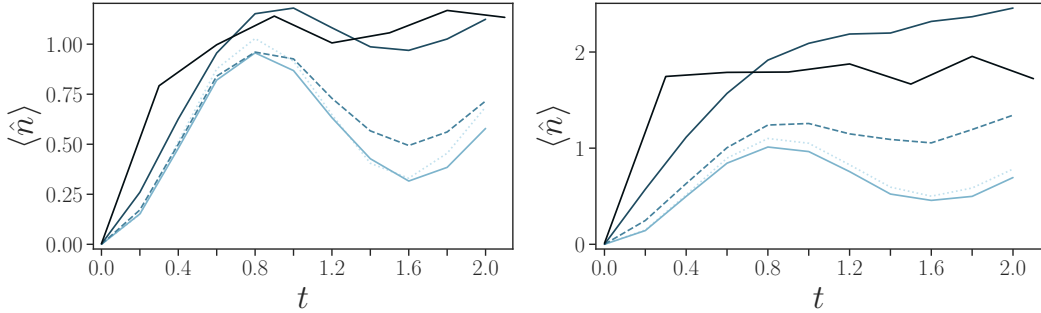
Figure 6.11: Average bosonic occupation $\langle \hat{n} \rangle$ at different truncation levels of the harmonic oscillator for one spin under noise. (a) $d_{HO} = 4$ (b) $d_{HO} = 8$. Noiseless, $\xi = 0.01$, 0.1, 1 in lighter to darker colors, with first-order Trotterization in solid lines and second-order Trotterization in dashed lines. Exact simulations as dotted lines. Parameters are $\epsilon = 0.5$, $\omega = 4$, $\lambda = 2$, $\gamma = 1$.

6.2.5 State Probabilities

After looking at higher level observables, we want to investigate the underlying dynamics of the states. Fig. 6.12 shows the state probabilities over time at different noise levels. We previously achieved optimal results using different Trotter formulas and time-steps Δt at different noise-levels ξ, but for simplicity here we show first-order Trotter at $\Delta t = 0.2$ in all panels.

Fig. 6.12(a) shows the desired exact dynamics. The initial state consists of an excited spin $|\uparrow\rangle$ and no excitations in the harmonic oscillator $|0\rangle$ (purple line). Partially the spin drops to the ground state and excites a level in the harmonic oscillator (orange line), and we observe some oscillation. At the same time, owing to the open system, the excited spin partially dissipates directly into the environment, leaving the system in the lowest energy state (blue line). We also see higher energy states populated (e.g. pink line), signifying an effect of $\hat{\sigma}^x$ in the Hamiltonian (Eq. 2.1).

Comparing the exact simulation (Fig. 6.12(a)) and the noiseless circuit (Fig. 6.12(b)), we observe some quantitative differences using the (suboptimal) first-order Trotter formula.

In contrast, at $\xi = 1$ the noise becomes dominant after one to two time-steps (Fig. 6.12(e)). After that the evolution stays relatively constant over time, with the probability of a state essentially determined by the qubit configuration associated with that state. As the qubits tend mostly towards the ground state under noise, the predominantly measured state is also the ground state of the system (blue line).

For $\xi = 0.1$ in Fig. 6.12(d), the states are similarly biased towards low energy states, but less so. Finally the low-noise case of $\xi = 0.01$ in Fig. 6.12(c) is hardly indistinguishable from the noiseless simulation Fig. 6.12(b).

Finally, Fig. 6.12(f) compares the infidelity between the noise-levels $\xi = 0.01, 0.1, 1$ (lighter to darker colours) to the exact simulation. For $\xi = 1$ the infidelity peaks at $t = 0.6$ and decreases at later times. We hypothesize that this is due to coherences (off-diagonal terms in the density matrix) decreasing in the exact simulation, as the system goes to equilibrium. A similar reduction of coherence is known to also occur in the presence of noise, matching the noisy with the exact simulation. The lines for noiseless (not shown) and $\xi = 0.01$ simulations overlap.

Simulating the state evolution remains challenging at medium to high noise levels.
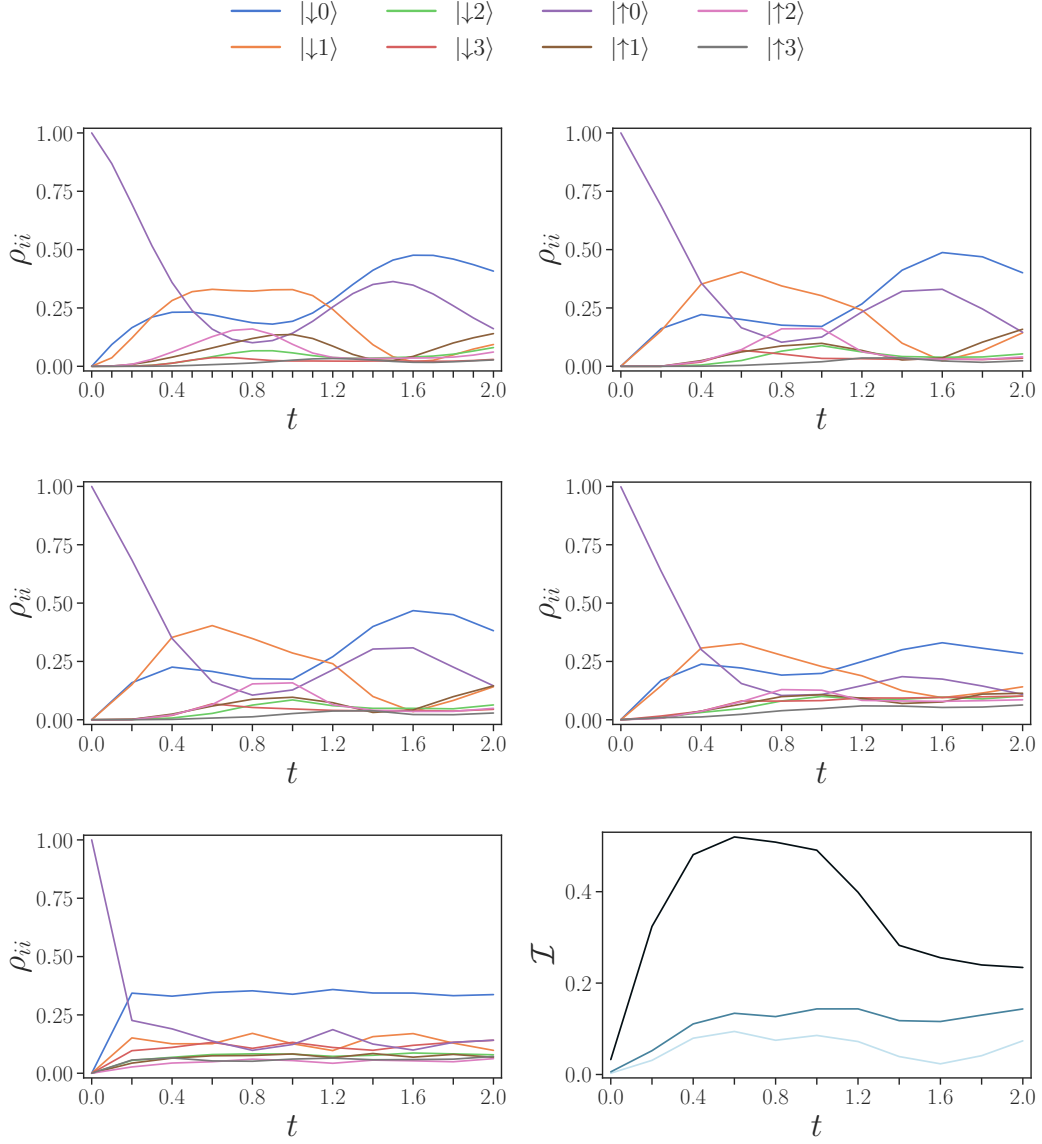
Figure 6.12: Evolution over time at different noise levels. (a) Exact (b) noise-less simulations. Simulations at noise-level (c) $\xi = 0.1$ (d) $\xi = 0.01$ (e) $\xi = 1$ (current devices). (f) Infidelity over time comparing each noise-level to the exact case. All results use first-order Trotter at $\Delta t = 0.2$. Parameters are $\epsilon = 0.5$, $\omega = 4$, $\lambda = 2$.

6.3   Results for the Two Spin System

We now extend the system to two spins so as to see whether it is possible to study correlation developing between them through a mediated interaction via

61

the harmonic oscillator, as the two spins do not directly interact with each other. We use the parameters $\epsilon = 0.5$, $\omega = 6$, $\lambda = 2$ and $\gamma = 1$. We prepare the initial state in a product state of one spin in the excited state, one in the ground state, and the harmonic oscillator completely empty. This allows to observe non-trivial dynamics while still requiring a small number of occupied level for the harmonic oscillator.

6.3.1 Trotterization

As for the single spin simulations, we first evaluate the infidelity in the presence of noise. Simulating two spins requires roughly twice the number of gates as simulating one spin. A single Δt evolution with a first-order Trotter requires 8 single-qubits and 36 CX-gates, while the second-order Trotter requires 177 single-qubits and 70 CX gates, see Figs. 5.2 and Sec. B.
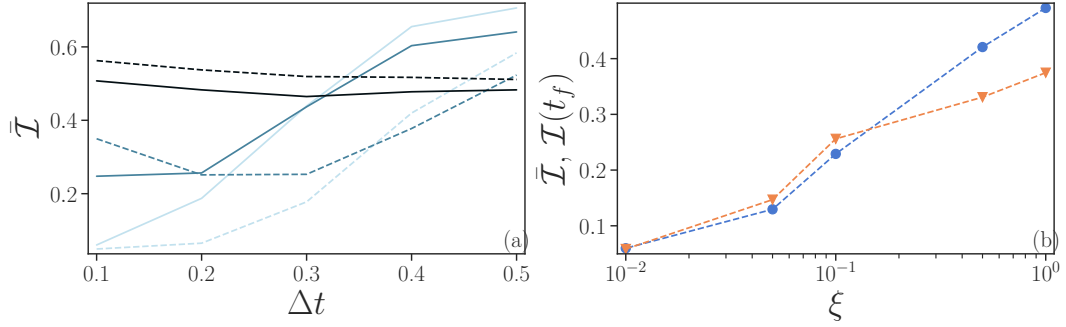
Figure 6.13: (a) Infidelity averaged over time as a function of time-step size Δt for an evolution from $t = 0$ to a final time $t_f = 2$. Different noise levels $\xi = 0.01$, 0.1, 1 are represented by lighter to darker colors. (b) Time-averaged (blue circles) and final (orange triangles) infidelity as a function of noise levels. Here the final time is taken as $t_f = 2$. and we choose $\Delta t = 0.2$. In both panels, results from first-order Trotter implementations are represented by continuous lines, while second-order by dashed lines. Parameters $\epsilon = 0.5$, $\omega = 4$, $\lambda = 2$, $\gamma = 1$.

We depict the infidelity versus the length of the time step Δt in Fig. 6.13(a). Like in the one spin case, we observe that for intermediate values of noise there is an optimal time interval Δt that corresponds to lowest infidelity, and that first-order Trotterization can perform better at smaller Δt. We find that the optimal Trotter time-step Δt to be the same as for the single spin case.
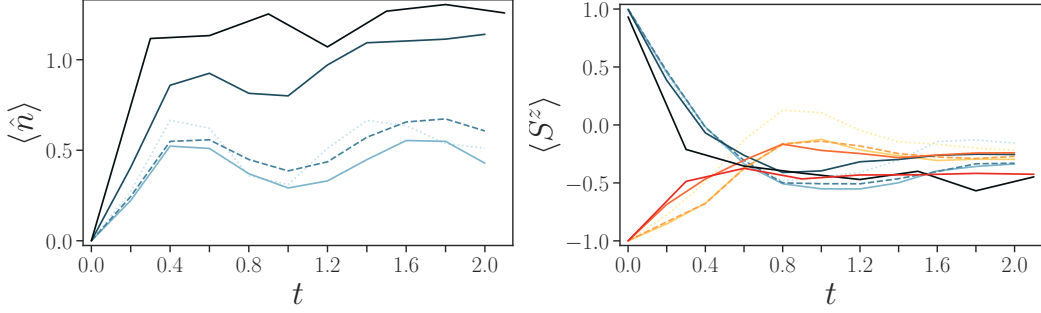
Figure 6.14: Observables for two spins on noisy hardware. (a) Average bosonic occupation $\langle \hat{n} \rangle$ (b) spin-z $\langle \hat{S}^z \rangle$ as function of time. Different noise levels $\xi = 0.01$, 0.1, 1 are presented, respectively by lighter to darker colors. In (b) and (c) blue lines account for s_1 and red lines for s_2. As a reference, exact simulations are depicted by the blue dotted lines. Results obtained using first-order Trotterization are with solid lines, while second-order with dashed lines. Other parameters are $\epsilon = 0.5$, $\omega = 6$, $\lambda = 2$ and $\gamma = 1$.

6.3.2 Observables

Before turning to computing correlations between the spins, we consider observables in the spins and the harmonic oscillator separately.

In Fig. 6.14(a) we observe an increased number of bosons in the presence of noise, similar to the single-spin behaviour discussed in Sec. 6.2.4.

The evolution of the spins in z-direction is depicted in Fig. 6.14(b). Starting in the excited state, s_1 quickly decays (blue lines), while there is an almost simultaneous rise in s_2 (red lines). We note that in both spins the features in z-direction are well captured, even in the presence of noise (darker colours).

S^x and S^y under Noise

For the one spin system we observed that the characteristics of spin in x-direction deviate significantly in the noisy circuits. In Fig. 6.15(a,b) we consider $\langle \hat{S}^x \rangle$ in the two spin system. For low to medium noise levels $\langle \hat{S}^x \rangle$ stays close to 0, with $\langle \hat{S}^x_1 \rangle$ and $\langle \hat{S}^x_2 \rangle$ slightly oscillating in opposite directions. For $\xi = 1$, as in the single spin system, we observe a significant increase in $\langle \hat{S}^x \rangle$ after a few time-steps.

We observe the same behaviour for $\langle \hat{S}^y \rangle$ in Fig. 6.15(c,d). In all four panels in Fig. 6.15 as well as for one spin in Fig. 6.10 the $\langle \hat{S} \rangle$ values grows notably $\approx 0.2 - 0.4$ on current hardware ($\xi = 1$). We are unsure what causes the increase, but suspect it is due to the nature of the depolarizing error (see Sec. 3.4.1). Nevertheless, in our simulation the spin behaviour in x-/y-direction

can only be represented faithfully at low levels of noise.
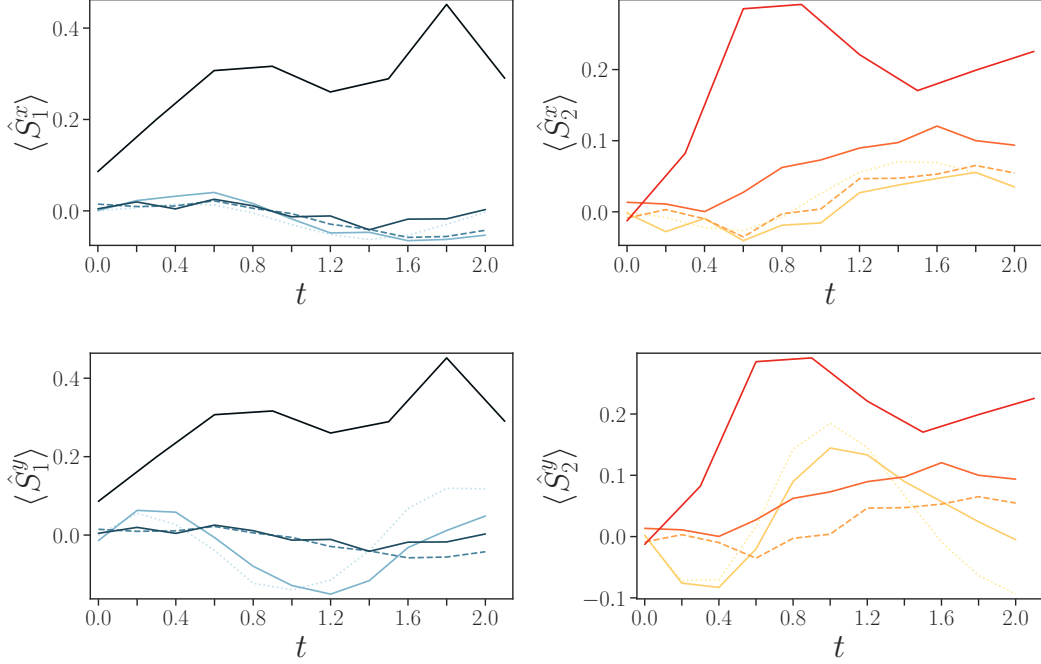
Figure 6.15: Evolution of the spins in x- and y-direction under noise in the two spin system. $\langle \hat{S}^z \rangle$ in (a) spin one and (b) spin two, $\langle \hat{S}^x \rangle$ in (c) spin one and (d) spin two as function of time. Different noise levels noiseless, $\xi = 0.01$, 0.1, 1 are presented, respectively by lighter to darker colors. As a reference, exact simulations are depicted by the dotted lines. Results obtained using first-order Trotterization are with solid lines, while second-order with dashed lines. Parameters are $\epsilon = 0.5$, $\omega = 6$, $\lambda = 2$ and $\gamma = 1$.

Spin-Spin Correlations

We observed some anti-symmetric behaviour in $\langle \hat{S}_{1,2} \rangle$ in Fig. 6.14, which could possibly be explained by an interaction mediated by the harmonic oscillator, or, in the case of the noisy simulations, coincidental effects of noise. To evaluate whether our system exhibits true correlation we consider the correlators C^{ZZ}, C^{XX} at different noise levels.

$$C^{ZZ} = \langle \hat{S}_1^z \hat{S}_2^z \rangle - \langle \hat{S}_1^z \rangle \langle \hat{S}_2^z \rangle$$
$$C^{XX} = \langle \hat{S}_1^x \hat{S}_2^x \rangle - \langle \hat{S}_1^x \rangle \langle \hat{S}_2^x \rangle. \tag{6.1}$$

In Fig. 6.16 we show C^{ZZ} and C^{XX} for, again, noiseless, $\xi = 0.01$, 0.1, 1 from lighter to darker lines. The solid lines correspond to first-order Trotter
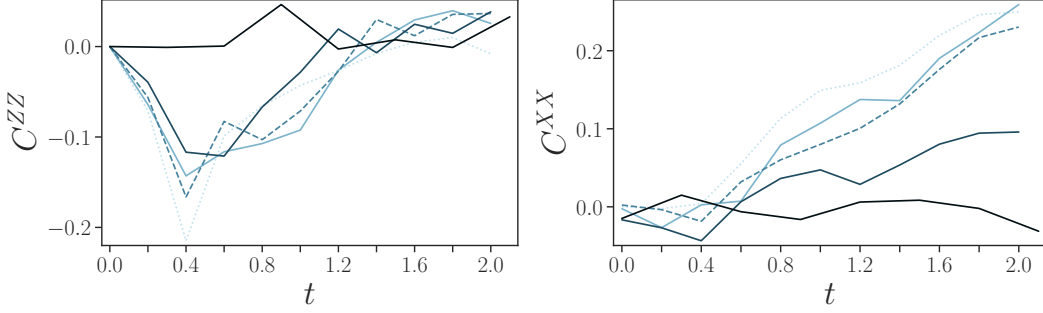
Figure 6.16: Correlations for the case of two spins. (a) Spin-z connected correlation C^{ZZ} (b) spin-x connected correlation C^{XX} as a function of time. Noiseless, $\xi = 0.01$, 0.1, 1 are presented, respectively by lighter to darker colors. As a reference, exact simulations are depicted by the dotted lines. Results obtained using first-order Trotterization are with solid lines, while second-order with dashed lines. Other parameters are $\epsilon = 0.5$, $\omega = 6$, $\lambda = 2$ and $\gamma = 1$.

and dashed lines to second-order Trotter and these Trotterization orders have been chosen as they result, for the respective amount of noise, to the lowest infidelity. In both panels the dotted lines correspond to the exact values, The exact case simulations shows a build-up in anti-correlation in z-direction at $t = 0.4$, before reducing to 0 which can be observed already for $\xi = 0.1$. A correlation in x-direction builds up monotonously over time and one would need $\xi = 0.01$ for a clearer signal.

6.3.3 State Probabilities

We again present the dynamics of the state probabilities underlying the observables. Much of the previous discussion for one spin in Sec. 6.2.5 holds for the two spin case, which is shown in Fig. 6.17.

The exact evolution is given in Fig. 6.17(a). At $t = 0$ the system starts with one spin excited and no excitations in the harmonic oscillator (grass green line), which quickly decays. Whereas in the single spin case the spin de-excited in favor of an excitation in the harmonic oscillator, here we observe a rise, and later a decay, of the excitation transferring to the other spin (orange line). Similar to the one spin system, the excited spin partially decays into the environment, resulting in the overall ground state (blue line).

Again, we observe a flattening of the lines with increasing noise, Fig. 6.17(b-e). At $\xi = 1$ (Fig. 6.17(e)) the qubits are predominantly in the $|0\rangle$ state, blue line.

We conclude that a qualitatively correct evolution of the states can only be achieved at low noise levels and small Trotterization time-steps.

6.4 Scaling to larger Systems

In principle, using our method, the system could be scaled up to a higher number of spins, and one should be able to observe correlations building up through the harmonic oscillator. In practice, the larger number of gates required to realize a bigger system would limit the fidelity in NISQ devices. Like going from one to two spins in this work, the circuit depth generally grows linearly with the number of spins, as to account for the interactions between each spin and the harmonic oscillator. While an increased number of qubits for spins and auxiliary might not directly be a problem, as much larger quantum computers are available, limited connectivity might prove difficult. Since two-qubit operations are limited to neighbouring qubits, increasing SWAP operations might be necessary, growing the CX-gates count. An interesting avenue accounting for connectivity is co-designing the chip with the problem in mind, as in [62].

At the same time, more spins could require including more levels of the harmonic oscillator, resulting in more qubits and more gates. To avoid that, going from one to two spins we had to increase ω to keep the higher levels of the harmonic oscillator sparsely populated. If one does not want to increase the number of levels studied for the harmonic oscillator, a similar adjustment, like decreasing the coupling between the harmonic oscillator and the spins, would be necessary when increasing the number of spins.
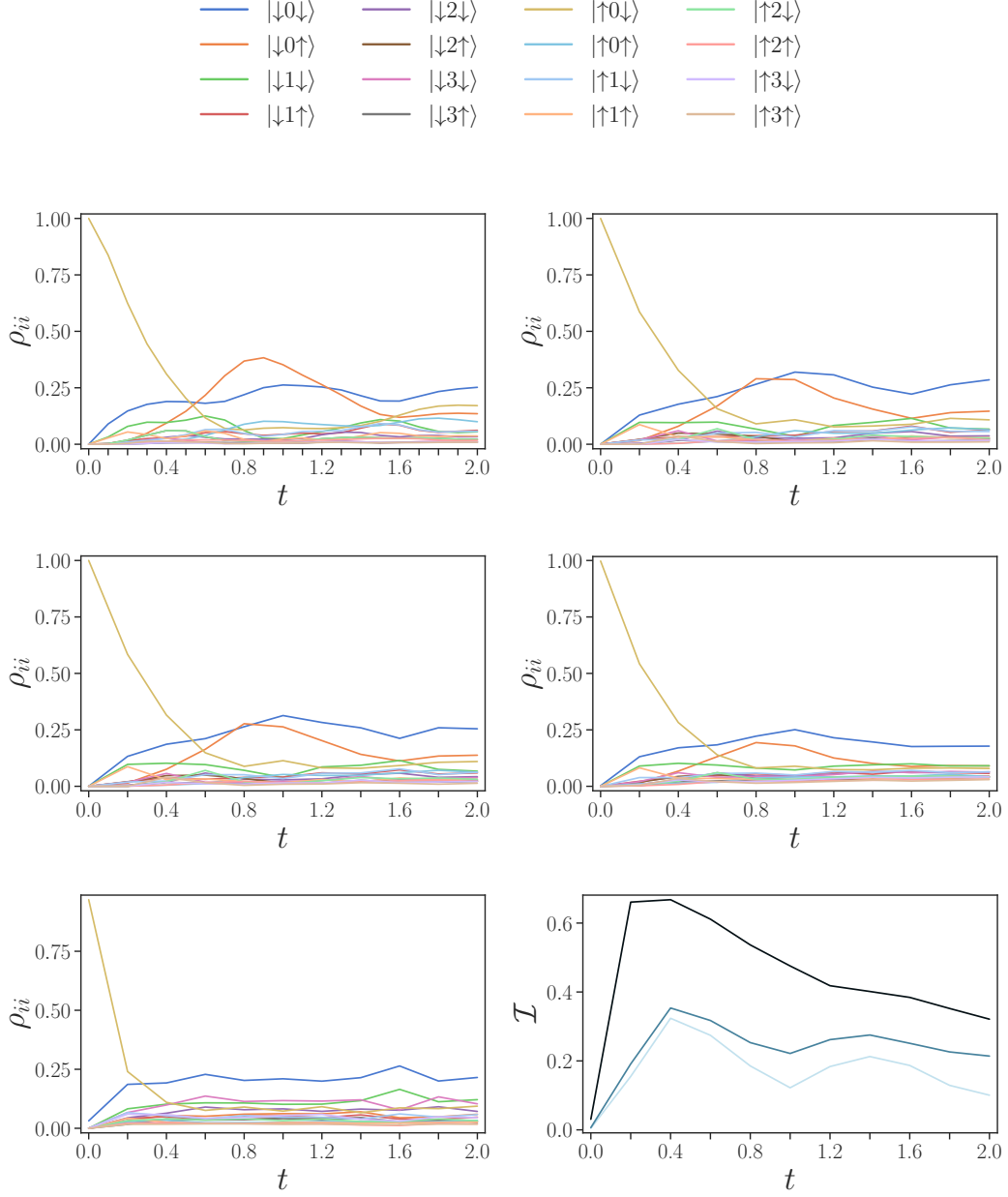
Figure 6.17: Evolution over time at different noise levels for the two spin system. (a) Exact (b) noiseless simulations. Simulations at noise-level (c) $\xi = 0.01$ (d) $\xi = 0.1$ (e) $\xi = 1$ (current devices). (f) Infidelity over time comparing each noise-level to the exact case. All results use first-order Trotter at $\Delta t = 0.2$. Parameters are $\epsilon = 0.5$, $\omega = 4$, $\lambda = 2$.

Chapter 7

Conservation in the Jaynes-Cummings Model

In the previous chapter we simulated open system dynamics in the spin-boson model, where the unitary evolution itself did not conserve any quantities. We now consider the opposite: a closed system with a number-conserving Hamiltonian. This variation of the spin-boson system allows for a post-selection strategy as an error mitigation technique.

7.1 Jaynes-Cummings Model

Like the spin-boson model, the Jaynes–Cummings model was developed in quantum optics to study light-matter interaction and describe the phenomena of spontaneous emission and absorption of photons. The Jaynes-Cummings model was derived out of the quantum Rabi Hamiltonian, like we used in Eq. (2.1), to make it exactly solvable [27]. It relies on the RWA, where the atomic transition frequency ω_a and the field mode frequency ω_f are small compared to the coupling strength λ [67, 68, 69]

$$\text{RWA}: \ |\omega_a - \omega_f| \ll |\omega_a - \omega_f|, \ \lambda/\omega_f \ll 1 \tag{7.1}$$

Under the RWA the interaction term in Eq. (2.1) can be approximated as

$$\begin{aligned} \hat{H}_I^{SB} &= \lambda \ \hat{\sigma}^x \left(\hat{a}^\dagger + \hat{a} \right) \\ &= \lambda \left(\hat{\sigma}^- + \hat{\sigma}^+ \right) \left(\hat{a}^\dagger + \hat{a} \right) \\ &= \lambda \left(\hat{\sigma}^- \hat{a}^\dagger + \hat{\sigma}^+ \hat{a} \right) + \lambda \left(\hat{\sigma}^+ \hat{a}^\dagger + \hat{\sigma}^- \hat{a} \right) \end{aligned} \tag{7.2}$$

$$\hat{H}_I^{JC} \approx \lambda \left(\hat{\sigma}^- \hat{a}^\dagger + \hat{\sigma}^+ \hat{a} \right) \tag{7.3}$$

where the counter-rotating term $\lambda \left(\hat{\sigma}^+ \hat{a}^\dagger + \hat{\sigma}^- \hat{a} \right)$ was neglected in the last step.

This turns out to be a valid approximation for the near resonance and weak coupling regimes, giving rise to phenomena like Rabi oscillations and vacuum Rabi mode splitting [27]. Theoretically the Jaynes-Cummings Hamiltonian describes the interaction of a two-level system with single mode of a quantized electromagnetic field, like the system of an atom in an optical cavity or resonator. Experimentally it has been studied in quantum system such as cavity QED [143, 144, 145], trapped ions [146, 147], quantum dots [148], and circuit QED [149, 150].

The Jaynes–Cummings Hamiltonian we consider is of the form

$$\hat{H}_{JC} = \hbar\omega \hat{a}^\dagger \hat{a} + \sum_{i=1}^{N_S} \left(\frac{1}{2} \hat{S}_i^z + \lambda(\hat{\sigma}^- \hat{a}^\dagger + \hat{\sigma}^+ \hat{a}) \right) \tag{7.4}$$

In contrast to the spin-boson Hamiltonian in Eq. (2.1), the Jaynes-Cummings Hamiltonian exhibits a continuous $U(1)$ symmetry under the operator $\hat{N}$

$$\hat{N} = \hat{a}^\dagger \hat{a} + \sum_{k=1}^{N_S} \hat{\sigma}_k^+ \hat{\sigma}_k^- \tag{7.5}$$

$$\hat{N} \left| \psi \right\rangle = \kappa \left| \psi \right\rangle \tag{7.6}$$

which was previously broken by the counter rotating term. $\left[\hat{H}_{JC}, \hat{N} \right] = 0$ conserves the number of excitations κ

$$\kappa = \kappa_{HO} + \kappa_S \tag{7.7}$$

$$= \text{const.} \tag{7.8}$$

Where κ_{HO} counts the number of excited levels in the harmonic oscillator and κ_S the number of spins in the excited state.

7.1.1   Reduced Hilbert Space

In the following we consider two spins $N_S = 2$. We set the initial state of the system to $\kappa = 2$ excitations, one in the harmonic oscillator and one in the first spin

$$\begin{aligned} \left| \psi_{N_S=2} \right\rangle (t=0) &= \left| S \right\rangle \otimes \left| B \right\rangle \otimes \left| S \right\rangle \\ &= \left| \uparrow \right\rangle \otimes \left| 1 \right\rangle \otimes \left| \downarrow \right\rangle \end{aligned} \tag{7.9}$$

From the initial state in Eq. (7.9) only four states are accessible under $\hat{H}_{JC}$, out of the 16 states in the full Hilbert Space.

$$
\begin{aligned}
d_{JC}^{full} &= dim\left(\mathcal{H}_S \otimes \mathcal{H}_{HO} \otimes \mathcal{H}_S\right) = 2 \cdot 4 \cdot 2 \\
&= 16 \\
d_{JC}^{eff} &= 4 \\
&\mathrel{\hat{=}} |{\uparrow}\,0\,{\uparrow}\rangle, \ |{\uparrow}\,1\,{\downarrow}\rangle, \ |{\downarrow}\,1\,{\uparrow}\rangle, \ |{\downarrow}\,2\,{\downarrow}\rangle \tag{7.10}
\end{aligned}
$$

7.1.2   Post-Selection Strategy

The strategy we consider is to use post-selection as error mitigation to make use of the reduced Hilbert Space. We discard non-physical measurement results which break the excitation number conservation, that is states which are not listed in Eq. (7.10), and renormalize such that the probabilities of the four states sum up to one.

The conservation holds only in z-direction and cannot be leveraged for measurements in the x- or y-basis. Thus there are no improvements to the infidelity, which is based on QST, or to $\langle \hat{S}^x \rangle$ or $\langle \hat{S}^y \rangle$. Instead of the infidelity we are going to use the MAE as an error measure.

7.2   Results using Post-Selection

7.2.1   Encoding

To implement the Jaynes-Cummings model we have to map the Hamiltonian using an integer-to-bit encoding and Trotterize it, identical to the procedure for previous Hamiltonians. The harmonic oscillator can be occupied at levels $0, 1, 2$, see Eq. (7.10), which can be encoded with two qubits. For the parameters, we choose $\epsilon = 0.5$, $\omega = 4$, $\lambda = 2$, the same as for the single spin spin-boson Hamiltonian.

We first decide on an optimal encoding. To focus on the post-selection from the conservation, we do not consider unary and full-unary, but rather standard binary and Gray code. One time-step of the unitary $e^{-i\hat{H}_{JC}\Delta t}$ requires {97 RZ, 56 CX, 52 SX, 4 X} gates using Gray code, where as using standard binary requires fewer gates: {74 RZ, 56 CX, 44 SX, 1 X}. That is significantly more than previously in the spin-boson model, which required {53 RZ, 29 CX, 30 SX, 3 X} gates for one time-step of the unitary with Gray code, dissipation, and reset. The encoded Jaynes-Cummings Hamiltonian is listed in Appendix B.3, and the circuits for one time-step are depicted in Appendix C.2.

In Fig. 7.1 we compare the MAE in standard binary and Gray code on noisy hardware. The results make use of post-selection and a first-order Trotterization of the unitary at $\Delta t = 0.2$. At all noise levels standard binary is preferred over Gray code, thus we only consider standard binary going forward.
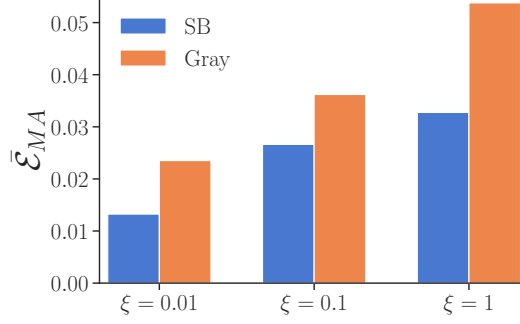
Figure 7.1: Time-averaged MAE over $t = 0, \ldots, 2$ when using standard binary and Gray code to map the Jaynes-Cummings Hamiltonian at varying levels of noise. We use post-selection and the first-order Trotter formula at $\Delta t = 0.2$. Parameters are $\epsilon = 0.5$, $\omega = 4$, $\lambda = 2$.

7.2.2   Error from Trotterization

The first error source is the Trotterization, which we depict in Fig. 7.2(a) using noiseless simulations. We observe that the second-order formula (dashed line) is preferred over first-order (solid line), and post-selection (blue line) results in lower errors than no post-selection (orange line). Thus, even without noise, post-selection significantly improves the results.

We previously saw that the error in the Trotterization varies with the choice of the Hamiltonian. In Fig. 7.2(b) we show the MAE from the Trotterization in the spin-boson model (green line) for comparison. We observe that with and without post-selection (blue line) the Jaynes-Cummings model can seemingly be implemented at lower error than the spin-boson model.

However we have to address that in the definition of the MAE in Eq. (3.15) we normalize by the number of states. Since in $\hat{H}_{JC}$ only a quarter of the states are non-zero, see Eq. (7.10), we would expect the MAE in simulations of $\hat{H}_{JC}$ to be only a quarter compared to the MAE in previous Hamiltonians. From this point of view the Trotterization error in the Jaynes-Cummings Hamiltonian in just four states is comparable to the error in the 16 states of the two spin-boson Hamiltonian. Thus we conclude that the Jaynes-Cummings Hamiltonian is harder to Trotterize than the spin-boson Hamiltonian.
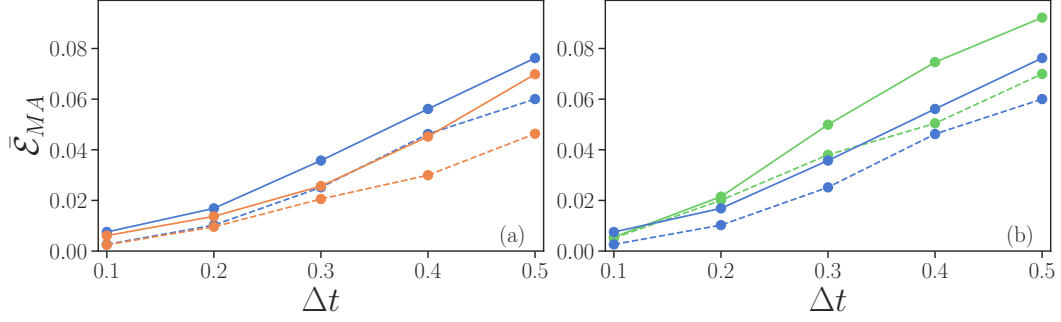
Figure 7.2: Trotterization error of the Jaynes-Cummings Hamiltonian. Time-averaged MAE as a function of time-step size Δt for for noiseless evolutions from $t = 0$ to $t = 2$. (a) In the Jaynes-Cummings model with (orange) and without (blue) post-selection. (b) In the two spin spin-boson model (green) and again in the Jaynes-Cummings model without post-selection (blue). The solid and dashed lines are used respectively for first-order and second-order Trotter implementations. The parameters are $\epsilon = 0.5$, $\omega = 4$, $\lambda = 2$.

7.2.3 Error from Noise

The second error source is the noise in the hardware, which we address now.

In Fig. 7.3(a) we again show the time-averaged MAE without any post-selection, but here at varying levels of noise. At a low noise level $\xi = 0.01$ (brightest line) the scaling of the infidelity in terms of Δt is similar to the noiseless simulations above. However at $\xi = 0.1$ and $\xi = 1$ the infidelity becomes largely independent of the time-step size and saturates at a high level.

We observe the same scaling behaviour for simulations with post-selection, depicted in Fig. 7.3(b). Importantly the error is reduced at all levels, especially $\xi = 0.1$ and $\xi = 1$, indicating that the post-selection is most effective in more noisy devices. Going forward we also note that under noise the lowest error is achieved with a first-order Trotter formula.

7.2.4 Error as a Function of Noise

We further investigate the scaling of the error as a function of noise, depicted in Fig. 7.4. For the spin-boson model we previously observed a logarithmic growth for the infidelity. Here in the Jaynes-Cummings model the error growth stagnates, with and without post-selection, indicating that the results are already maximally noisy. With post-selection (panel (b)) the MAE at the final time-step (orange line) seems to stay constant and even reduce with noise. To investigate we consider the error over time in Fig. 7.5(a).
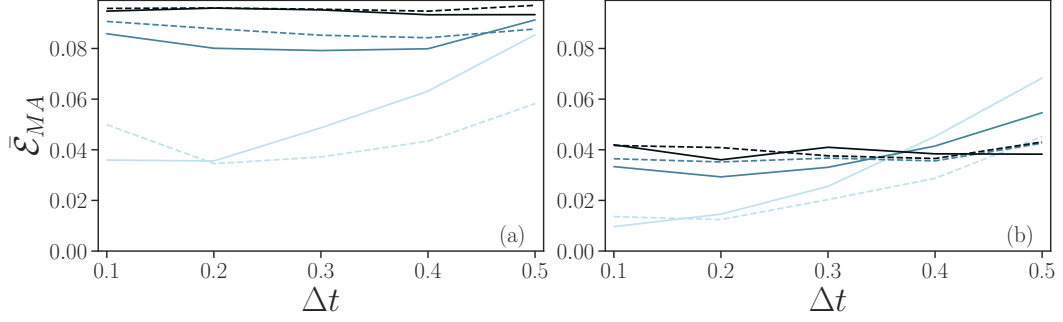
Figure 7.3: Trotterization under noise. MAE averaged over time as a function of time-step size Δt. (a) Without (b) with post-selection. Noisy simulations at $\xi = 0.01$, 0.1, 1, represented by lighter to darker colors. The solid and dashed lines are used respectively for first-order and second-order Trotter implementations. The parameters are $\epsilon = 0.5$, $\omega = 4$, $\lambda = 2$.
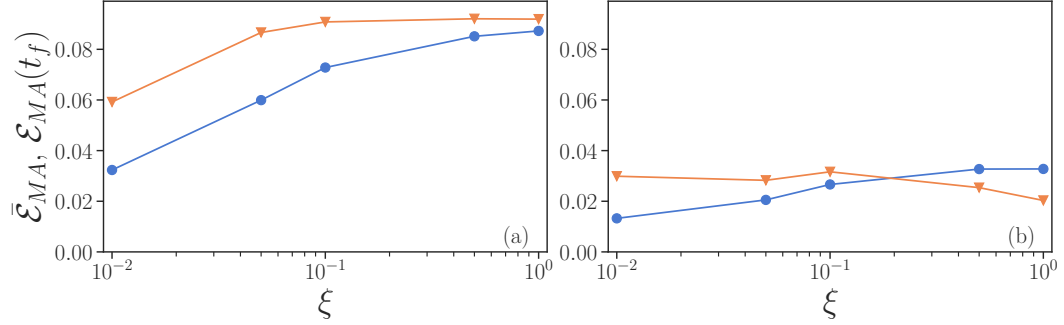
Figure 7.4: Error as a function of noise. Time-averaged (blue circles) and final (orange triangles) MAE as a function of noise levels, (a) with (b) without post-selection. The final time is taken as $t_f = 2$, and we choose $\Delta t = 0.2$. At noise-factor $\xi = 0.01$, 0.1, 1 (from lighter to darker colors). First-order Trotter implementations are represented by continuous lines, while second-order implementations are depicted by dashed lines. Parameters are $\epsilon = 0.5$, $\omega = 4$, $\lambda = 2$.

7.2.5 Post-Selection over Time

To explicitly see the improvement of the error mitigation, Fig. 7.5 compares the time evolution of the MAE with (solid) and without (dashed) post-selection. First-order Trotterization is represented by solid lines, second-order by dashed lines, and noise levels $\xi = 0.01$, 0.1, 1 by lighter to darker colors. After the initial time-step the error grows abruptly and then remains distributed equally over time. The rise is more pronounced at higher noise. At all levels of noise, there is a notable improvement when using post-selection.

We next consider the relation between the error rate and the post-selection more closely. In Fig. 7.5 we plot the relative number of measurements which were kept (not discarded) in the post-selection process, as previously defined in Eq. (5.8).

$$\mathcal{R}_{ps} = \frac{M_{total} - M_{discarded}}{M_{total}} \tag{7.11}$$

As the error (solid lines) increases with time, the number of valid measurements drops (dotted lines). While for $\xi = 0.01$, 0.1 the growth in discarded measurements is more or less linear, it is more abrupt for $\xi = 1$, again signifying that the noise dominates and saturates the error.

We conclude that post-selection as error mitigation is an effective strategy in reducing the error, but the error rate stays proportional.
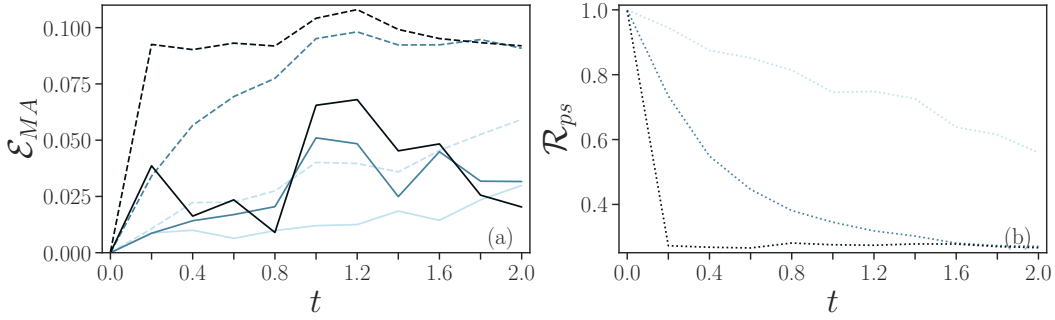
Figure 7.5: Effect of post-selection. (a) MAE with (solid lines) and without (dashed lines) using post-selection for error mitigation. (b) post-selection-ratio $\mathcal{R}_{ps}$ (dotted lines) when using post-selection. Different noise levels $\xi = 0.01$, 0.1, 1 are represented by lighter to darker colors. Parameters are set to $\epsilon = 0.5$, $\omega = 4$, $\lambda = 2$ and first-order Trotter at $\Delta t = 0.2$.

7.2.6 State Probabilities

In order to better understand the saturation of the error we now consider the state probabilities using post-selection. Fig. 7.6(a) depicts the evolution at $\xi = 0.01$ (triangles) and without noise (dots). Both follow the exact simulation (solid lines) closely and partly overlap.

At $\xi = 0.1$ (Fig. 7.6(b)) and $\xi = 1$ (Fig. 7.6(c)) the states stagnate after one to two time-steps. This aligns with previous observations that the Jaynes-Cummings Hamiltonian is intractable at medium to the currently high noise levels, as the noise dominates the results.
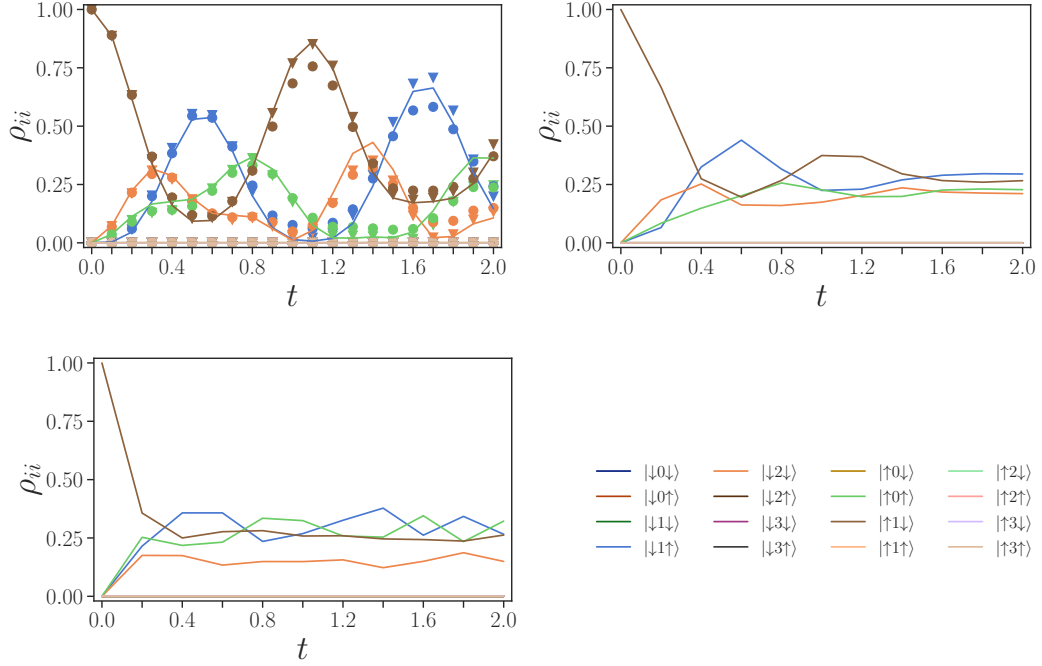
Figure 7.6: Evolution of the state probabilities. (a) $\xi = 0.01$ (triangles), noiseless (dots), and exact simulations (solid line) (b) $\xi = 0.1$ (solid line) (c) $\xi = 1$ (solid line). We use optimal Trotterization parameters: $\Delta t = 0.2$ at $\xi = 1$, $\Delta t = 0.2$ at $\xi = 0.1$, $\Delta t = 0.1$ at $\xi = 0.01$, all using first-order. Other parameters are $\epsilon = 0.5$, $\omega = 4$, $\lambda = 2$.

7.2.7 Observables

So far we focused on the feasibility of obtaining the correct state probabilities and the associated error. In the following we consider the accuracy in the simulation of observables.

Spins

The evolution of the spins is depicted in Fig. 7.7. The first spin starts in $|\uparrow\rangle$, while the second spin starts in $|\downarrow\rangle$ (Fig. 7.7(a,d)). After the initial time we observe a counter oscillation in $\langle \hat{S}^z \rangle$ in the exact, noiseless and $\xi = 0.01$ simulations. At medium to current noise $\xi = 0.1, 1$ both spins approach $\langle \hat{S}^z \rangle \approx 0$ instead.

The spin in x- and y-direction is zero in the exact reference, Fig. 7.7(b,c, e, f). However the noiseless circuit implementation (brightest solid line) shows oscillations in both directions in the first spin (Fig. 7.7(b,c)). The fluctuations reduce for higher levels of noise. In the second spin $\langle \hat{S}^x \rangle_2$ and $\langle \hat{S}^y \rangle_2$ remain

constant after the first time-step, after we again see the previously observed jump under noise.

We conclude that the behaviour of the spins can be simulated qualitatively accurately only at low levels of noise and in z-direction, where post-selection can be used, while for the first spin the error from the Trotterization is already too high to faithfully represent the evolution along x and y.
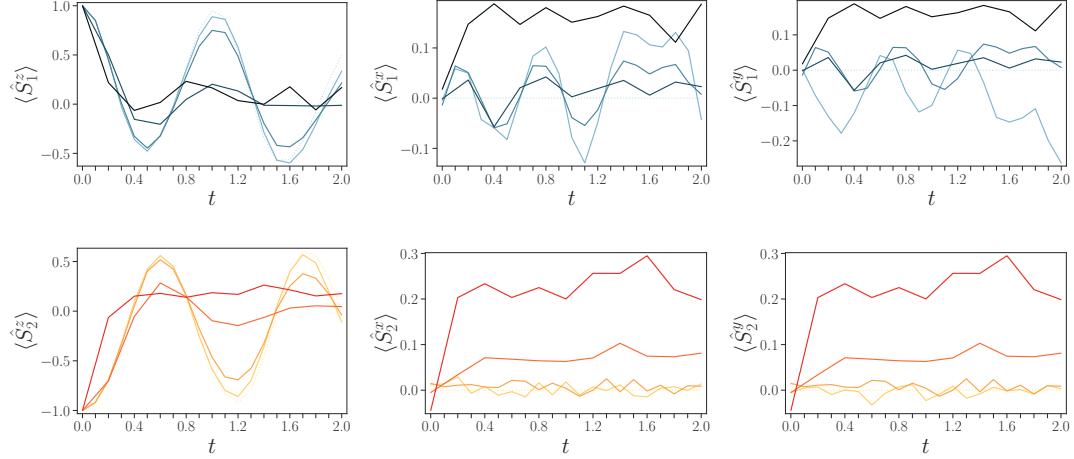
Figure 7.7: Expectation values for both spins on noisy hardware. (a) spin-z $\langle \hat{S}^z \rangle$ (b) spin-x $\langle \hat{S}^x \rangle$ as function of time. Exact, noiseless and $\xi = 0.01$, 0.1, 1 are presented, respectively by lighter to darker colors. Exact simulations are depicted by dotted lines. Results obtained using first-order Trotterization are with solid lines, while second-order with dashed lines. Other parameters are $\epsilon = 0.5$, $\omega = 4$, $\lambda = 2$.

Spin-Spin Correlations

We study the correlations between the spins in Fig. 7.8.

In z-direction (panel (a)) the exact reference (dotted line) remains close to zero until a negative peak at $t \approx 1.7$. The noiseless and $\xi = 0.01$ simulations (brightest solid lines) only somewhat represent the peak and predict a false second peak at $t \approx 0.4$.

In x-direction we observe a negative correlation and some oscillation in the exact evolution. Using circuit implementations (solid line), with and without noise, we instead measure close to zero.

It thus occurs that at $\Delta t = 0.1$, even without noise, the Trotterization error in the Jaynes-Cummings model is too high to simulate correlations qualitatively correct.
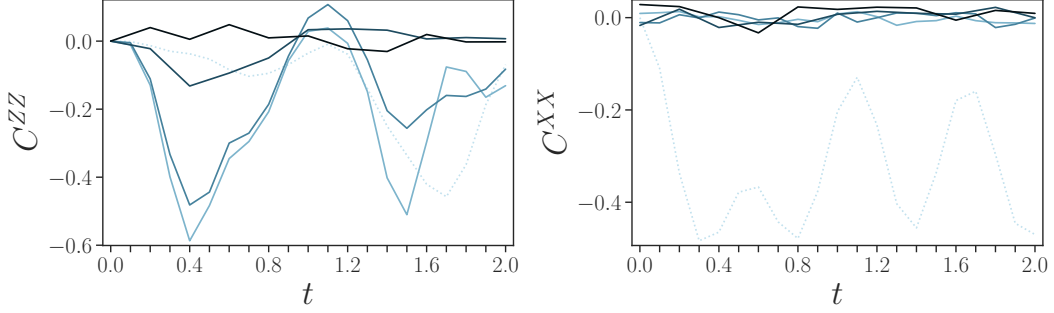
Figure 7.8: Correlations between two spins in the Jaynes-Cummings model. (a) spin-z connected correlation C^{ZZ} (b) spin-x connected correlation C^{XX} as a function of time. Exact, noiseless and $\xi = 0.01$, 0.1, 1 are presented, respectively by lighter to darker colors. Exact simulations are depicted by dotted lines. Results obtained using first-order Trotterization are with solid lines, while second-order with dashed lines. Parameters are $\epsilon = 0.5$, $\omega = 4$, $\lambda = 2$.

Conclusion

This chapter considered the Jaynes-Cummings Hamiltonian and the role post-selection under a conserved symmetry.

The Jaynes-Cummings system proved harder to simulate compared to the spin-boson model, requiring around 50% more gates to implement the unitary. Further the Trotterization error was high, with the error in just four non-zero states of $\hat{H}_{JC}$ being as large as the error in the 16 states of the two spin spin-boson Hamiltonian.

Using post-selection as error mitigation significally reduced the error in noisy and noiseless simulations. Nevertheless at $\xi = 0.1$ and $\xi = 1$ noise dominated the results, making simulations of states and S_k^x, S_k^y of individual spins only feasible up to $\xi = 0.01$. Calculating spin-spin correlations at $\Delta t = 0.1$ was not possible even in noiseless circuits, as the Trotterization error was too large at this time-step size.

While post-selection based on symmetries is a promising method, the Hamiltonian itself proved to be the bottleneck in our simulations, resulting in deep circuits and high Trotterization errors.

Chapter 8

Conclusions and Outlook

8.1 Conclusions

In this work we studied the feasibility of simulating open spin-boson dynamics on a quantum computer. We used current quantum devices supplied by IBM, and, anticipating future improved hardware, we run our simulations on 10% and 1% of current noise levels.

To implement the Hamiltonian, we used a second-quantization mapping of the bosonic degrees of freedom and a Trotterization of the unitary. We considered the implementation error in four integer-to-bit encodings and two variations of the spin-boson interaction. We observed that the Trotterization error depends significantly on the choice of Hamiltonian, and that the choice of encoding can notably affect the number of gates required. Using unary encoding, we demonstrated post-selection as an error mitigation technique. Our results showed a reduction in the simulation error at low to medium noise levels, offsetting an increased gate count.

To implement the dissipative dynamics, we used collisions and resets with auxiliary qubits. We found multiple descriptions of the amplitude damping channel and showed their equivalence. We demonstrated that the noise in the gates itself mimics the dissipative action of the channel we aimed to simulate.

We found that in our parameter regime the Hamiltonian simulation is the limiting factor to the fidelity. We surveyed optimal Trotterization formulas and time-step sizes depending on the level of noise in the system. We found that certain open dissipative rates could greatly increase the fidelity in noisy circuits, and that in the parameter regime that we considered current noise levels make simulations particularly challenging.

Using simulations with reduced-noise models we were able to show that it would be possible to attain much higher fidelities. Furthermore, certain observables could be well represented with larger amounts of noise. Importantly,

the simulation of an open system can be more accurate than unitary evolution, as the open system dynamics could be closer to how a noisy computer is already affecting a state.

In the final chapter we considered a variation of the spin-boson Hamiltonian which conserved the combined excitation number in the harmonic oscillator and the spins, the Jaynes-Cummings model. We showed that a post-selection strategy, similar to the use with unary encoding, can significantly improve the accuracy in the simulation. We noted that the strategy could only be leveraged in the computational basis and observables based on measurements in other bases did not see an improvement.

8.2   Outlook

Our work provides a significant first step to address the simulation of open quantum systems in near-future devices. Using our method, future developments in noise reduction in the hardware, in post-processing error mitigation, and also in reducing the number of gates for unitary evolutions can lead to significant increase in simulation power.

Nevertheless multiple open questions remain. Although collision models can theoretically simulate any interaction with an environment, we constrained the dissipation to the spins, which limited the use of auxiliary qubits or reset gates, and simplified the theoretical description. An interesting avenue for future work would be to arrive at a general method which can efficiently realize a given Lindbladian, even when the implementation of the channel is previously unknown.

Further, it remains unclear whether Trotterization will yield an advantage on NISQ devices. As the simulated system grows so does the depth of the circuit. The mapping of the interaction between the bosons and the spins to qubits in particular required large gate counts, restricting the number of harmonic oscillator levels one can model in practice. Thus utilizing the bosonic degrees of freedoms of the qubit hardware could be a promising alternative.

Appendix A

Conventions and Definitions

Here we list some of the conventions implicitly assumed throughout the work. We use natural units $h = \hbar = 1$.

Where not marked explicitly, subfigures / subpanels are addressed by lowercase letters, ordered first left to right, then top to bottom.

A.1   Operators

Lower indices on operators denote different sites, which we occasionally omit for neighbouring sites $\hat{o}\hat{p} = \hat{o}_i \hat{p}_{i+1} = \hat{o}_i \otimes \hat{p}_{i+1}$.

A.1.1   Spin Operators

For spins we denote $|0\rangle$ as the ground state and $|1\rangle$ as the excited state.

$$|0\rangle = |gs\rangle = |\downarrow\rangle = \begin{pmatrix} 1 \\ 0 \end{pmatrix}, \ \hat{S}^z |0\rangle = -1 |0\rangle \tag{A.1}$$

$$|1\rangle = |ex\rangle = |\uparrow\rangle = \begin{pmatrix} 0 \\ 1 \end{pmatrix}, \ \hat{S}^z |1\rangle = +1 |1\rangle \tag{A.2}$$

We define the spin operators $\hat{S}^x = \hat{\sigma}^x$, $\hat{S}^y = \hat{\sigma}^y$, $\hat{S}^z = -\hat{\sigma}^z$ via the Pauli matrices

$$\hat{\sigma}^x = |\uparrow\rangle \langle\downarrow| + |\downarrow\rangle \langle\uparrow| = \begin{pmatrix} 0 & 1 \\ 1 & 0 \end{pmatrix} \tag{A.3}$$

$$\hat{\sigma}^y = -i |\uparrow\rangle \langle\downarrow| + i |\downarrow\rangle \langle\uparrow| = \begin{pmatrix} 0 & -i \\ i & 0 \end{pmatrix} \tag{A.4}$$

$$\hat{\sigma}^z = |\uparrow\rangle \langle\uparrow| - |\downarrow\rangle \langle\downarrow| = \begin{pmatrix} 1 & 0 \\ 0 & -1 \end{pmatrix} \tag{A.5}$$

We use the spin rising $\hat{\sigma}^+$ and lowering $\hat{\sigma}^-$ operators

$$\hat{\sigma}^+ = |\uparrow\rangle \langle\downarrow| = \frac{1}{2}(\hat{\sigma}^x - i\hat{\sigma}^y) = \begin{pmatrix} 0 & 0 \\ 1 & 0 \end{pmatrix} \tag{A.6}$$

$$\hat{\sigma}^- = |\downarrow\rangle \langle\uparrow| = \frac{1}{2}(\hat{\sigma}^x + i\hat{\sigma}^y) = \begin{pmatrix} 0 & 1 \\ 0 & 0 \end{pmatrix} \tag{A.7}$$

A.1.2 Bosonic Operators

We write bosons in their occupation basis. $|n\rangle$ describes a site occupied by n bosons, or equivalent a harmonic oscillator with n excitations

$$E_n = \omega \hat{a}^\dagger \hat{a} |n\rangle = \omega \hat{n} |n\rangle \tag{A.8}$$

$$= \omega n \tag{A.9}$$

A.2 Little-Endian Convention

Qiskit uses the Little-Endian convention for the ordering of qubits and classical bits. The qubits are labelled from right to left, the most significant (last) bit on the left to the least significant (first) bit on the right.

This changes the structure of tensor products relative to the circuits. A wave-function $|A \otimes B \otimes C\rangle = |ABC\rangle$ is represented by a quantum circuit qc as $\mathrm{qc}_0 = |C\rangle$, $\mathrm{qc}_1 = |B\rangle$, $\mathrm{qc}_2 = |A\rangle$.

Similarly, a multi-qubit gate $U = U_A \otimes U_B \otimes U_C = U_A U_B U_C$ will act as $U_C(\mathrm{qc}_0)$, $U_B(\mathrm{qc}_1)$, $U_A(\mathrm{qc}_2)$.

Since our code is running on Qiskit, we adopt the same convention throughout the thesis. In effect, figures of circuits will be labelled top to bottom (first to last), while matrices and states are labelled from right to left.

A.3 Gate Definitions

Here we give the definitions of gate operations used , including native gates implemented on the quantum computer, and non-native gates which have to be decomposed (transpiled) into native gates first.

A.3.1 Native Gates

The native gates on IBM's devices are {CNOT, ID, RZ, SX, X}.

The CNOT- or controlled-X-gate flips the qubit q_0 depending on qubit q_1

$$CX\ q_0, q_1 = I \otimes |0\rangle\langle 0| + X \otimes |1\rangle\langle 1| = \begin{pmatrix} 1 & 0 & 0 & 0 \\ 0 & 0 & 0 & 1 \\ 0 & 0 & 1 & 0 \\ 0 & 1 & 0 & 0 \end{pmatrix} \tag{A.10}$$

The X-gate is just the Pauli operator $\hat{\sigma}^x$

$$X = \begin{pmatrix} 0 & 1 \\ 1 & 0 \end{pmatrix} \tag{A.11}$$

The square root of the X-gate is given by the $\sqrt{X}$-gate

$$\sqrt{X} = \frac{1}{2}\begin{pmatrix} 1+i & 1-i \\ 1-i & 1+i \end{pmatrix} \tag{A.12}$$

The RZ-gate describes a rotation about the Z-axis.

$$RZ(\lambda) = \exp\left(-i\frac{\lambda}{2}Z\right) = \begin{pmatrix} e^{-i\frac{\lambda}{2}} & 0 \\ 0 & e^{i\frac{\lambda}{2}} \end{pmatrix} \tag{A.13}$$

Since the RZ-gate is diagonal it can be implemented on the hardware virtually, that is at zero error and duration, by utilizing the phase of the microwave pulses [139].

A.3.2 Non-native Gates

The Hadamard-gate changes the basis from the Z-basis $|0\rangle, |1\rangle$ to the x-basis $|+\rangle, |-\rangle$ via a π-rotation about the (X+Z)-axis

$$H = \frac{1}{\sqrt{2}}\begin{pmatrix} 1 & 1 \\ 1 & -1 \end{pmatrix} \tag{A.14}$$

The S-adjoint-gate introduces a $-\pi/4$ phase, and is used together with the Hadamard-gate to rotate to the y-basis $|+i\rangle, |-i\rangle$

$$S^\dagger = \begin{pmatrix} 1 & 0 \\ 0 & -i \end{pmatrix} \tag{A.15}$$

In the CRY-gate, like in the CX-gate, the qubit q_1 controls a rotation around the Y-axis qubit q_0

$$CRY(\theta)\ q_0, q_1 = I \otimes |0\rangle\langle 0| + RY(\theta) \otimes |1\rangle\langle 1| \tag{A.16}$$

$$= \begin{pmatrix} 1 & 0 & 0 & 0 \\ 0 & \cos\frac{\theta}{2} & 0 & -\sin\frac{\theta}{2} \\ 0 & 0 & 1 & 0 \\ 0 & \sin\frac{\theta}{2} & 0 & \cos\frac{\theta}{2} \end{pmatrix} \tag{A.17}$$

A.4 Mathematics

A.4.1 Partial Trace

In chapter 4 we used the partial trace to get the density matrix of the spin from the density matrix of the spin-auxiliary system. To trace out the subsystem B of the density matrix of a combined system $\hat{\rho}_{AB}$, we perform the operation

$$\hat{\rho}_A = \text{Tr}_A [\hat{\rho}_{AB}] \tag{A.18}$$

$$= \begin{pmatrix} 1 & 0 & 0 & 0 \\ 0 & 1 & 0 & 0 \end{pmatrix} \cdot \hat{\rho}_{AB} \cdot \begin{pmatrix} 1 & 0 \\ 0 & 1 \\ 0 & 0 \\ 0 & 0 \end{pmatrix} \tag{A.19}$$

After which we have to renormalize the density matrix, such that $\text{Tr}[\hat{\rho}_A] = 1$.

Appendix B

Encoded Hamiltonians

B.1 Spin-Boson Hamiltonian

After the mapping of the harmonic oscillator to qubits using an integer-to-bit encoding (see Sec. 3.2.1), a given Hamiltonian is written as a sum of Pauli strings h_i. The unitary $e^{\sum_i h_i}$ is then trotterized (Eqs. (3.9, 3.12)).

Here we give the mappeed Hamiltonians used throughout the thesis in terms of their Pauli strings.

B.1.1 Spin-Boson Hamiltonian for Main Results

The main Hamiltonian of interest in this work, and the one used for the results in chapter 6, is the spin-boson Hamiltonian $\hat{H}_{SB}$ of Eq. (2.1). The number of gates required to realize $\hat{H}_{SB}$ with the different encodings on the quantum hardware are in Fig. 5.2. Here we will also give the numbers for the individual gate types.

The mapped Hamiltonian $\hat{H}_{SB} = \sum_i h_i$ for the single spin case using Gray code reads explicitly

$$
\begin{aligned}
\hat{H}_{SB} = &- \sqrt{2}\sigma^x{}_0\sigma^x{}_1\sigma^z{}_2 + \sqrt{2}\sigma^x{}_0\sigma^x{}_1 \\
&+ (1 - \sqrt{3})\sigma^x{}_0\sigma^x{}_2\sigma^z{}_1 + (1 + \sqrt{3})\sigma^x{}_0\sigma^x{}_2 \\
&+ \frac{1}{4}\sigma^x{}_0 - \frac{1}{2}\sigma^z{}_0 - 2\sigma^z{}_1\sigma^z{}_2 - 4\sigma^z{}_1
\end{aligned}
\tag{B.1}
$$

requiring $\{24 \text{ RZ}, 14 \text{ CX}, 11 \text{ SX}, 2 \text{ X}\}$ gates. The two spins case reads

$$
\begin{aligned}
\hat{H}_{SB} = &- \sqrt{2}\sigma^x{}_0\sigma^x{}_1\sigma^z{}_2 + \sqrt{2}\sigma^x{}_0\sigma^x{}_1 \\
&+ (1 - \sqrt{3})\sigma^x{}_0\sigma^x{}_2\sigma^z{}_1 + (1 + \sqrt{3})\sigma^x{}_0\sigma^x{}_2 \\
&+ \frac{1}{4}\sigma^x{}_0 - \sqrt{2}\sigma^x{}_1\sigma^x{}_3\sigma^z{}_2 + \sqrt{2}\sigma^x{}_1\sigma^x{}_3 \\
&+ (1 - \sqrt{3})\sigma^x{}_2\sigma^x{}_3\sigma^z{}_1 + (1 + \sqrt{3})\sigma^x{}_2\sigma^x{}_3 \\
&+ \frac{1}{4}\sigma^x{}_3 - \frac{1}{2}\sigma^z{}_0 - 3\sigma^z{}_1\sigma^z{}_2 - 6\sigma^z{}_1 - \frac{1}{2}\sigma^z{}_3
\end{aligned}
\tag{B.2}
$$

requiring $\{53 \text{ RZ}, 29 \text{ CX}, 30 \text{ SX}, 3 \text{ X}\}$ gates.
Each term constitutes one of the h_i in Eqs. (3.9, 3.12).

B.1.2 Additional Encodings

In chapter 5 we further considered standard binary, unary, and full-unary encoding for $\hat{H}_{SB}$ for one spin, which we list here.
Standard binary, using $\{28 \text{ RZ}, 19 \text{ CX}, 15 \text{ SX}, 0 \text{ X}\}$ gates

$$
\begin{aligned}
\hat{H}_{SB} = &\sqrt{2}\sigma^x{}_0\sigma^x{}_1\sigma^x{}_2 + (1 - \sqrt{3})\sigma^x{}_0\sigma^x{}_2\sigma^z{}_1 + (1 + \sqrt{3})\sigma^x{}_0\sigma^x{}_2 \\
&+ \sqrt{2}\sigma^x{}_0\sigma^y{}_1\sigma^y{}_2 + \frac{1}{4}\sigma^x{}_0 - \frac{1}{2}\sigma^z{}_0 \\
&- 4\sigma^z{}_1 - 2\sigma^z{}_2 + 6
\end{aligned}
\tag{B.3}
$$

Unary, using $\{47 \text{ RZ}, 34 \text{ CX}, 24 \text{ SX}, 2 \text{ X}\}$ gates

$$
\begin{aligned}
\hat{H}_{SB} = &\sigma^x{}_0\sigma^x{}_1\sigma^x{}_2 + \sqrt{2}\sigma^x{}_0\sigma^x{}_2\sigma^x{}_3 + \sqrt{3}\sigma^x{}_0\sigma^x{}_3\sigma^x{}_4 \\
&+ \sigma^x{}_0\sigma^y{}_1\sigma^y{}_2 + \sqrt{2}\sigma^x{}_0\sigma^y{}_2\sigma^y{}_3 + \sqrt{3}\sigma^x{}_0\sigma^y{}_3\sigma^y{}_4 \\
&+ \frac{1}{4}\sigma^x{}_0 - \frac{1}{2}\sigma^z{}_0 - 2\sigma^z{}_2 - 4\sigma^z{}_3 - 6\sigma^z{}_4 + 12
\end{aligned}
\tag{B.4}
$$

Full-unary, using $\{97 \text{ RZ}, 72 \text{ CX}, 55 \text{ SX}, 0 \text{ X}\}$ gates

$$
\begin{aligned}
\hat{H}_{SB} = &\frac{1}{8}\sigma^x{}_0\sigma^x{}_4 + \sigma^x{}_0\sigma^x{}_5 + \sigma^x{}_1\sigma^x{}_4 + \frac{1}{8}\sigma^x{}_1\sigma^x{}_5 + \sqrt{2}\sigma^x{}_1\sigma^x{}_6 \\
&+ \sqrt{2}\sigma^x{}_2\sigma^x{}_5 + \frac{1}{8}\sigma^x{}_2\sigma^x{}_6 + \sqrt{3}\sigma^x{}_2\sigma^x{}_7 + \sqrt{3}\sigma^x{}_3\sigma^x{}_6 + \frac{1}{8}\sigma^x{}_3\sigma^x{}_7 \\
&+ \frac{1}{8}\sigma^y{}_0\sigma^y{}_4 + \sigma^y{}_0\sigma^y{}_5 + \sigma^y{}_1\sigma^y{}_4 + \frac{1}{8}\sigma^y{}_1\sigma^y{}_5 + \sqrt{2}\sigma^y{}_1\sigma^y{}_6 \\
&+ \sqrt{2}\sigma^y{}_2\sigma^y{}_5 + \frac{1}{8}\sigma^y{}_2\sigma^y{}_6 + \sqrt{3}\sigma^y{}_2\sigma^y{}_7 + \sqrt{3}\sigma^y{}_3\sigma^y{}_6 + \frac{1}{8}\sigma^y{}_3\sigma^y{}_7 \\
&+ \frac{1}{4}\sigma^z{}_0 - 1.75\sigma^z{}_1 - 3.75\sigma^z{}_2 - 5.75\sigma^z{}_3 - \frac{1}{4}\sigma^z{}_4 - 2.25\sigma^z{}_5 \\
&- 4.25\sigma^z{}_6 - 6.25\sigma^z{}_7 + 24
\end{aligned}
\tag{B.5}
$$

B.2 Other non-conserving Hamiltonians

In Sec. 5.1.1 we introduced two variations of the spin-boson Hamiltonian, $\hat{H}_{JC-I}$ and $\hat{H}_{Z-I}$. As in the main text, we present the mapped Hamiltonian using standard binary, Gray code, unary, and full-unary for the one spin system.

B.2.1 JC-Interaction

Standard binary, using {50 RZ, 28 CX, 30 SX, 1 X} gates

$$
\begin{aligned}
\hat{H}_{JC-I} =& \sqrt{1/2}\sigma^x{}_0\sigma^x{}_1\sigma^x{}_2 - 0.366\sigma^x{}_0\sigma^x{}_2\sigma^z{}_1 + 1.37\sigma^x{}_0\sigma^x{}_2 \\
& + \sqrt{1/2}\sigma^x{}_0\sigma^y{}_1\sigma^y{}_2 + \frac{1}{4}\sigma^x{}_0 - \sqrt{1/2}\sigma^x{}_1\sigma^y{}_0\sigma^y{}_2 \\
& + \sqrt{1/2}\sigma^x{}_2\sigma^y{}_0\sigma^y{}_1 - 0.366\sigma^y{}_0\sigma^y{}_2\sigma^z{}_1 + 1.37\sigma^y{}_0\sigma^y{}_2 \\
& - \frac{1}{2}\sigma^z{}_0 - 4\sigma^z{}_1 - 2\sigma^z{}_2 + 6
\end{aligned}
\tag{B.6}
$$

Gray code, using using {37 RZ, 29 CX, 20 SX, 0 X} gates

$$
\begin{aligned}
\hat{H}_{JC-I} =& -\sqrt{1/2}\sigma^x{}_0\sigma^x{}_1\sigma^z{}_2 + \sqrt{1/2}\sigma^x{}_0\sigma^x{}_1 - 0.366\sigma^x{}_0\sigma^x{}_2\sigma^z{}_1 \\
& + 1.37\sigma^x{}_0\sigma^x{}_2 + \frac{1}{4}\sigma^x{}_0 - \sqrt{1/2}\sigma^y{}_0\sigma^y{}_1\sigma^z{}_2 + \sqrt{1/2}\sigma^y{}_0\sigma^y{}_1 \\
& + 1.37\sigma^y{}_0\sigma^y{}_2\sigma^z{}_1 - 0.366\sigma^y{}_0\sigma^y{}_2 - \frac{1}{2}\sigma^z{}_0 - 2\sigma^z{}_1\sigma^z{}_2 \\
& - 4\sigma^z{}_1 + 6
\end{aligned}
\tag{B.7}
$$

Unary, using {80 RZ, 56 CX, 51 SX, 4 X} gates

$$
\begin{aligned}
\hat{H}_{JC-I} =& \frac{1}{2}\sigma^x{}_0\sigma^x{}_1\sigma^x{}_2 + \sqrt{1/2}\sigma^x{}_0\sigma^x{}_2\sigma^x{}_3 + \sqrt{3/4}\sigma^x{}_0\sigma^x{}_3\sigma^x{}_4 \\
& + \frac{1}{2}\sigma^x{}_0\sigma^y{}_1\sigma^y{}_2 + \sqrt{1/2}\sigma^x{}_0\sigma^y{}_2\sigma^y{}_3 + \sqrt{3/4}\sigma^x{}_0\sigma^y{}_3\sigma^y{}_4 \\
& + \frac{1}{4}\sigma^x{}_0 + \frac{1}{2}\sigma^x{}_1\sigma^y{}_0\sigma^y{}_2 - \frac{1}{2}\sigma^x{}_2\sigma^y{}_0\sigma^y{}_1 + \sqrt{1/2}\sigma^x{}_2\sigma^y{}_0\sigma^y{}_3 \\
& - \sqrt{1/2}\sigma^x{}_3\sigma^y{}_0\sigma^y{}_2 + \sqrt{3/4}\sigma^x{}_3\sigma^y{}_0\sigma^y{}_4 - \sqrt{3/4}\sigma^x{}_4\sigma^y{}_0\sigma^y{}_3 \\
& - \frac{1}{2}\sigma^z{}_0 - 2\sigma^z{}_2 - 4\sigma^z{}_3 - 6\sigma^z{}_4 + 12
\end{aligned}
\tag{B.8}
$$

Full-unary, using {46 RZ, 24 CX, 22 SX, 0 X} gates

$$
\begin{aligned}
\hat{H}_{JC-I} =& \frac{1}{8}\sigma^x{}_0\sigma^x{}_4 + \sigma^x{}_1\sigma^x{}_4 + \frac{1}{8}\sigma^x{}_1\sigma^x{}_5 + \sqrt{2}\sigma^x{}_2\sigma^x{}_5 + \frac{1}{8}\sigma^x{}_2\sigma^x{}_6 \\
&+ \sqrt{3}\sigma^x{}_3\sigma^x{}_6 + \frac{1}{8}\sigma^x{}_3\sigma^x{}_7 + \frac{1}{8}\sigma^y{}_0\sigma^y{}_4 + \sigma^y{}_1\sigma^y{}_4 + \frac{1}{8}\sigma^y{}_1\sigma^y{}_5 \\
&+ \sqrt{2}\sigma^y{}_2\sigma^y{}_5 + \frac{1}{8}\sigma^y{}_2\sigma^y{}_6 + \sqrt{3}\sigma^y{}_3\sigma^y{}_6 + \frac{1}{8}\sigma^y{}_3\sigma^y{}_7 + \frac{1}{4}\sigma^z{}_0 \\
&- 1.75\sigma^z{}_1 - 3.75\sigma^z{}_2 - 5.75\sigma^z{}_3 - \frac{1}{4}\sigma^z{}_4 - 2.25\sigma^z{}_5 \\
&- 4.25\sigma^z{}_6 - 6.25\sigma^z{}_7 + 24
\end{aligned}
\tag{B.9}
$$

Z-Interaction

Standard binary, using {27 RZ, 19 CX, 14 SX, 2 X} gates

$$
\begin{aligned}
\hat{H}_{Z-I} =& \frac{1}{4}\sigma^x{}_0 - \sqrt{2}\sigma^x{}_1\sigma^x{}_2\sigma^z{}_0 + 0.732\sigma^x{}_2\sigma^z{}_0\sigma^z{}_1 \\
&- (1+\sqrt{3})\sigma^x{}_2\sigma^z{}_0 - \sqrt{2}\sigma^y{}_1\sigma^y{}_2\sigma^z{}_0 - \frac{1}{2}\sigma^z{}_0 \\
&- 4\sigma^z{}_1 - 2\sigma^z{}_2 + 6
\end{aligned}
\tag{B.10}
$$

Gray code, using {23 RZ, 14 CX, 11 SX, 0 X} gates

$$
\begin{aligned}
\hat{H}_{Z-I} =& \frac{1}{4}\sigma^x{}_0 + \sqrt{2}\sigma^x{}_1\sigma^z{}_0\sigma^z{}_2 - \sqrt{2}\sigma^x{}_1\sigma^z{}_0 + \sqrt{3}\sigma^x{}_2\sigma^z{}_0\sigma^z{}_1 \\
&- (1+\sqrt{3})\sigma^x{}_2\sigma^z{}_0 - \frac{1}{2}\sigma^z{}_0 - 2\sigma^z{}_1\sigma^z{}_2 - 4\sigma^z{}_1 + 6
\end{aligned}
\tag{B.11}
$$

Unary, using {50 RZ, 34 CX, 24 SX, 0 X} gates

$$
\begin{aligned}
\hat{H}_{Z-I} =& \frac{1}{4}\sigma^x{}_0 - \sigma^x{}_1\sigma^x{}_2\sigma^z{}_0 - \sqrt{2}\sigma^x{}_2\sigma^x{}_3\sigma^z{}_0 - \sqrt{3}\sigma^x{}_3\sigma^x{}_4\sigma^z{}_0 \\
&- \sigma^y{}_1\sigma^y{}_2\sigma^z{}_0 - \sqrt{2}\sigma^y{}_2\sigma^y{}_3\sigma^z{}_0 - \sqrt{3}\sigma^y{}_3\sigma^y{}_4\sigma^z{}_0 \\
&- \frac{1}{2}\sigma^z{}_0 - 2\sigma^z{}_2 - 4\sigma^z{}_3 - 6\sigma^z{}_4 + 12
\end{aligned}
\tag{B.12}
$$

Full-unary, using {103 RZ, 70 CX, 56 SX, 1 X} gates

$$
\begin{aligned}
\hat{H}_{Z-I} = & -\sigma^x{}_0\sigma^x{}_1 + \frac{1}{8}\sigma^x{}_0\sigma^x{}_4 - \sqrt{2}\sigma^x{}_1\sigma^x{}_2 + \frac{1}{8}\sigma^x{}_1\sigma^x{}_5 - \sqrt{3}\sigma^x{}_2\sigma^x{}_3 \\
& + \frac{1}{8}\sigma^x{}_2\sigma^x{}_6 + \frac{1}{8}\sigma^x{}_3\sigma^x{}_7 + \sigma^x{}_4\sigma^x{}_5 + \sqrt{2}\sigma^x{}_5\sigma^x{}_6 + \sqrt{3}\sigma^x{}_6\sigma^x{}_7 \\
& - \sigma^y{}_0\sigma^y{}_1 + \frac{1}{8}\sigma^y{}_0\sigma^y{}_4 - \sqrt{2}\sigma^y{}_1\sigma^y{}_2 + \frac{1}{8}\sigma^y{}_1\sigma^y{}_5 - \sqrt{3}\sigma^y{}_2\sigma^y{}_3 \\
& + \frac{1}{8}\sigma^y{}_2\sigma^y{}_6 + \frac{1}{8}\sigma^y{}_3\sigma^y{}_7 + \sigma^y{}_4\sigma^y{}_5 + \sqrt{2}\sigma^y{}_5\sigma^y{}_6 + \sqrt{3}\sigma^y{}_6\sigma^y{}_7 \\
& + \frac{1}{4}\sigma^z{}_0 - 1.75\sigma^z{}_1 - 3.75\sigma^z{}_2 - 5.75\sigma^z{}_3 - \frac{1}{4}\sigma^z{}_4 - 2.25\sigma^z{}_5 \\
& - 4.25\sigma^z{}_6 - 6.25\sigma^z{}_7 + 24
\end{aligned}
\tag{B.13}
$$

B.3   Jaynes-Cummings Hamiltonian

In Sec. 7 we considered the Jaynes-Cummings Hamiltonian, which we mapped using standard binary and Gray code.

Gray code, using {97 RZ, 56 CX, 52 SX, 4 X} gates

$$
\begin{aligned}
\hat{H}_{JC} = & -\sqrt{1/2}\sigma^x{}_0\sigma^x{}_1\sigma^z{}_2 + \sqrt{1/2}\sigma^x{}_0\sigma^x{}_1 - 0.366\sigma^x{}_0\sigma^x{}_2\sigma^z{}_1 \\
& + 1.37\sigma^x{}_0\sigma^x{}_2 - \sqrt{1/2}\sigma^x{}_1\sigma^x{}_3\sigma^z{}_2 + \sqrt{1/2}\sigma^x{}_1\sigma^x{}_3 \\
& - 0.366\sigma^x{}_2\sigma^x{}_3\sigma^z{}_1 + 1.37\sigma^x{}_2\sigma^x{}_3 - \sqrt{1/2}\sigma^y{}_0\sigma^y{}_1\sigma^z{}_2 \\
& + \sqrt{1/2}\sigma^y{}_0\sigma^y{}_1 + 1.37\sigma^y{}_0\sigma^y{}_2\sigma^z{}_1 - 0.366\sigma^y{}_0\sigma^y{}_2 \\
& - \sqrt{1/2}\sigma^y{}_1\sigma^y{}_3\sigma^z{}_2 + \sqrt{1/2}\sigma^y{}_1\sigma^y{}_3 + 1.37\sigma^y{}_2\sigma^y{}_3\sigma^z{}_1 \\
& - 0.366\sigma^y{}_2\sigma^y{}_3 - \frac{1}{2}\sigma^z{}_0 - 2\sigma^z{}_1\sigma^z{}_2 \\
& - 4\sigma^z{}_1 - \frac{1}{2}\sigma^z{}_3 + 6
\end{aligned}
\tag{B.14}
$$

Standard binary, using {74 RZ, 56 CX, 44 SX, 1 X} gates

$$
\begin{aligned}
\hat{H}_{JC} =& \sqrt{1/2}\sigma^x{}_0\sigma^x{}_1\sigma^x{}_2 - 0.366\sigma^x{}_0\sigma^x{}_2\sigma^z{}_1 + 1.37\sigma^x{}_0\sigma^x{}_2 \\
& + \sqrt{1/2}\sigma^x{}_0\sigma^y{}_1\sigma^y{}_2 + \sqrt{1/2}\sigma^x{}_1\sigma^x{}_2\sigma^x{}_3 - \sqrt{1/2}\sigma^x{}_1\sigma^y{}_0\sigma^y{}_2 \\
& - \sqrt{1/2}\sigma^x{}_1\sigma^y{}_2\sigma^y{}_3 - 0.366\sigma^x{}_2\sigma^x{}_3\sigma^z{}_1 + 1.37\sigma^x{}_2\sigma^x{}_3 \\
& + \sqrt{1/2}\sigma^x{}_2\sigma^y{}_0\sigma^y{}_1 + \sqrt{1/2}\sigma^x{}_2\sigma^y{}_1\sigma^y{}_3 + \sqrt{1/2}\sigma^x{}_3\sigma^y{}_1\sigma^y{}_2 \\
& - 0.366\sigma^y{}_0\sigma^y{}_2\sigma^z{}_1 + 1.37\sigma^y{}_0\sigma^y{}_2 - 0.366\sigma^y{}_2\sigma^y{}_3\sigma^z{}_1 \\
& + 1.37\sigma^y{}_2\sigma^y{}_3 - \frac{1}{2}\sigma^z{}_0 - 4\sigma^z{}_1 \\
& - 2\sigma^z{}_2 - \frac{1}{2}\sigma^z{}_3 + 6
\end{aligned}
\tag{B.15}
$$

Appendix C

Circuits for one Time-Step

Here we explicitly show some of the circuits that we ran on the quantum computer to achieve our main results.

C.1 Spin-Boson Model

In chapter 6 we presented simulations of the open system dynamics in the spin-boson model using a first-order Trotterization of the closed and open system part.

C.1.1 One Spin System

We first give one time-step to simulate the one spin system, consisting of unitary evolution, dissipation, and reset. As in chapter 6, we consider Gray code and a first-order and a second-order Trotterization of the unitary, respectively pictured in Fig. C.1 and Fig. C.2.

The spins are represented by s_i, the harmonic oscillator modes (4 levels) are encoded on the b_i qubits and the auxiliary qubits are represented by a_i. Lines for the qubits continue over multiple rows. The initial state preparation and measurements are not shown. The gate values reflect the parameters $\epsilon = 0.5$, $\omega = 4$, $\lambda = 2$, $\gamma = 1$, $\Delta t = 1$.

C.1.2 Two Spin System

Fig. C.3 and Fig. C.4 display one time-step of unitary evolution, dissipation, and reset for the two spin system. We use the same parameters as for one spin above.

Figure C.1: One spin spin-boson system using a first-order Trotterization of the unitary. One time-step of unitary evolution, dissipation, and reset (black box), without initial state preparation or measurement. s represents the spin, b_i qubits for 4 levels of the harmonic oscillator, a the auxiliary qubit. Lines for the qubits continue over multiple rows. Parameters are $\epsilon = 0.5$, $\omega = 4$, $\lambda = 2$, $\gamma = 1$, $\Delta t = 1$.
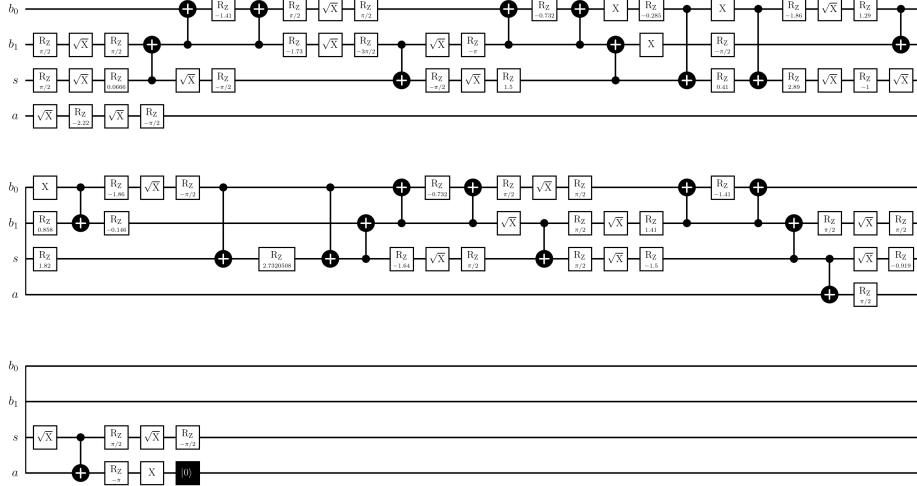
Figure C.2: One spin spin-boson system using a second-order Trotterization of the unitary. One time-step of unitary evolution, dissipation, and reset (black box), without initial state preparation or measurement. s represents the spin, b_i qubits for 4 levels of the harmonic oscillator, a the auxiliary qubit. Lines for the qubits continue over multiple rows. Parameters are $\epsilon = 0.5$, $\omega = 4$, $\lambda = 2$, $\gamma = 1$, $\Delta t = 1$.
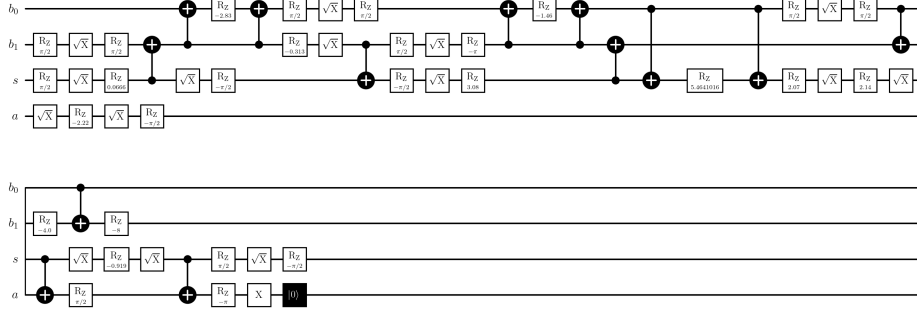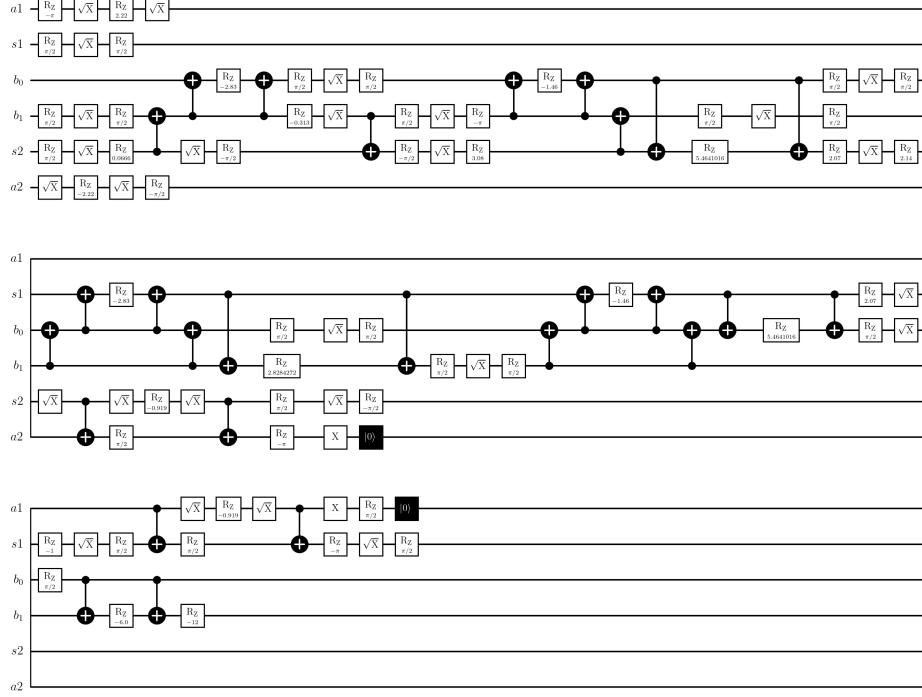
Figure C.3: Two spin spin-boson system using a first-order Trotterization of the unitary. One time-step of unitary evolution, dissipation, and reset (black box), without initial state preparation or measurement. s_i represent the spins, b_i qubits for 4 levels of the harmonic oscillator, a_i the auxiliary qubits. Lines for the qubits continue over multiple rows. Parameters are $\epsilon = 0.5$, $\omega = 4$, $\lambda = 2$, $\gamma = 1$, $\Delta t = 1$.

C.2 Jaynes-Cummings Model

We described a closed and number conserving Jaynes-Cummings model in chapter 7 with two spins. The circuit for one time-step using a first-order Trotterization of the unitary is depicted in Fig. C.5, while the second-order Trotterization is shown in Fig. C.2. Both figures use standard binary as an encoding do not include the preparation of the initial state or the final measurements.
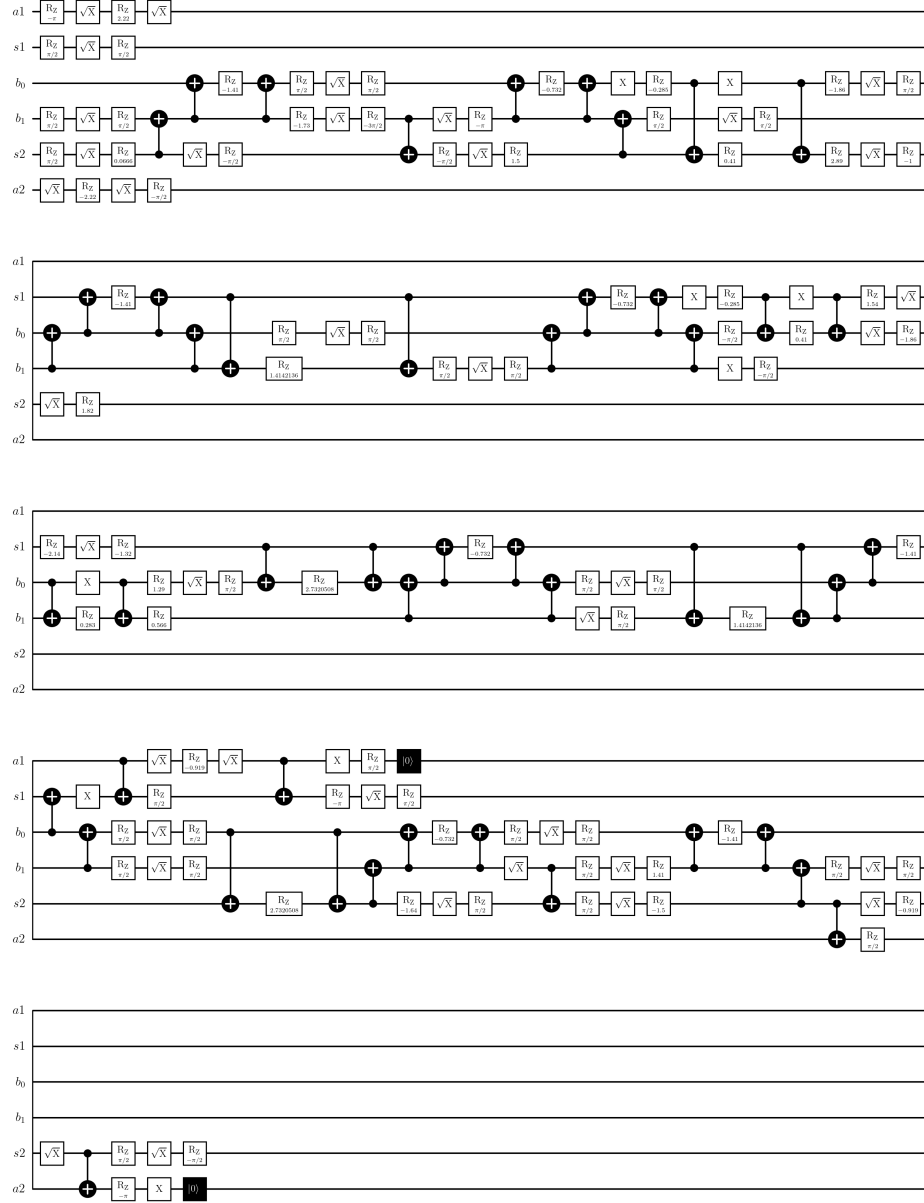
Figure C.4: Two spin spin-boson system using a second-order Trotterization of the unitary.

Figure C.5: One time-step of the two spin Jaynes-Cummings system using a first-order Trotterization of the unitary. s represents the spin, b_i qubits for 4 levels of the harmonic oscillator. Lines for the qubits continue over multiple rows. Parameters are $\epsilon = 0.5$, $\omega = 4$, $\lambda = 2$, $\Delta t = 1$.

Figure C.6: One time-step of the two spin Jaynes-Cummings system using second-order Trotterization.

Bibliography

[1] P. W. Shor, "Polynomial-time algorithms for prime factorization and discrete logarithms on a quantum computer," *Proceedings 35th Annual Symposium on Foundations of Computer Science*, 1994.

[2] L. K. Grover, "A fast quantum mechanical algorithm for database search," *Proceedings of the Twenty-Eighth Annual ACM Symposium on Theory of Computing*, 1996.

[3] D. Deutsch and R. Jozsa, "Rapid solution of problems by quantum computation," *Proceedings of the Royal Society of London. Series A: Mathematical and Physical Sciences*, vol. 439, pp. 553–558, Dec. 1992.

[4] R. Cleve, A. Ekert, C. Macchiavello, and M. Mosca, "Quantum algorithms revisited," *Proceedings of the Royal Society of London. Series A: Mathematical, Physical and Engineering Sciences*, 1998.

[5] R. P. Feynman, "Simulating physics with computers," *International Journal of Theoretical Physics*, vol. 21, pp. 467–488, June 1982.

[6] S. Lloyd, "Universal quantum simulators," *Science*, vol. 273, pp. 1073–1078, aug 1996.

[7] M. Motta and J. Rice, "Emerging quantum computing algorithms for quantum chemistry," *WIREs Computational Molecular Science*, vol. 12, May 2022.

[8] U. Schollwöck, "The density-matrix renormalization group in the age of matrix product states," *Ann. Phys.*, vol. 326, no. 1, pp. 96–192, 2011.

[9] U. Schollwöck, "The density-matrix renormalization group," *Rev. Mod. Phys.*, vol. 77, pp. 259–315, Apr. 2005.

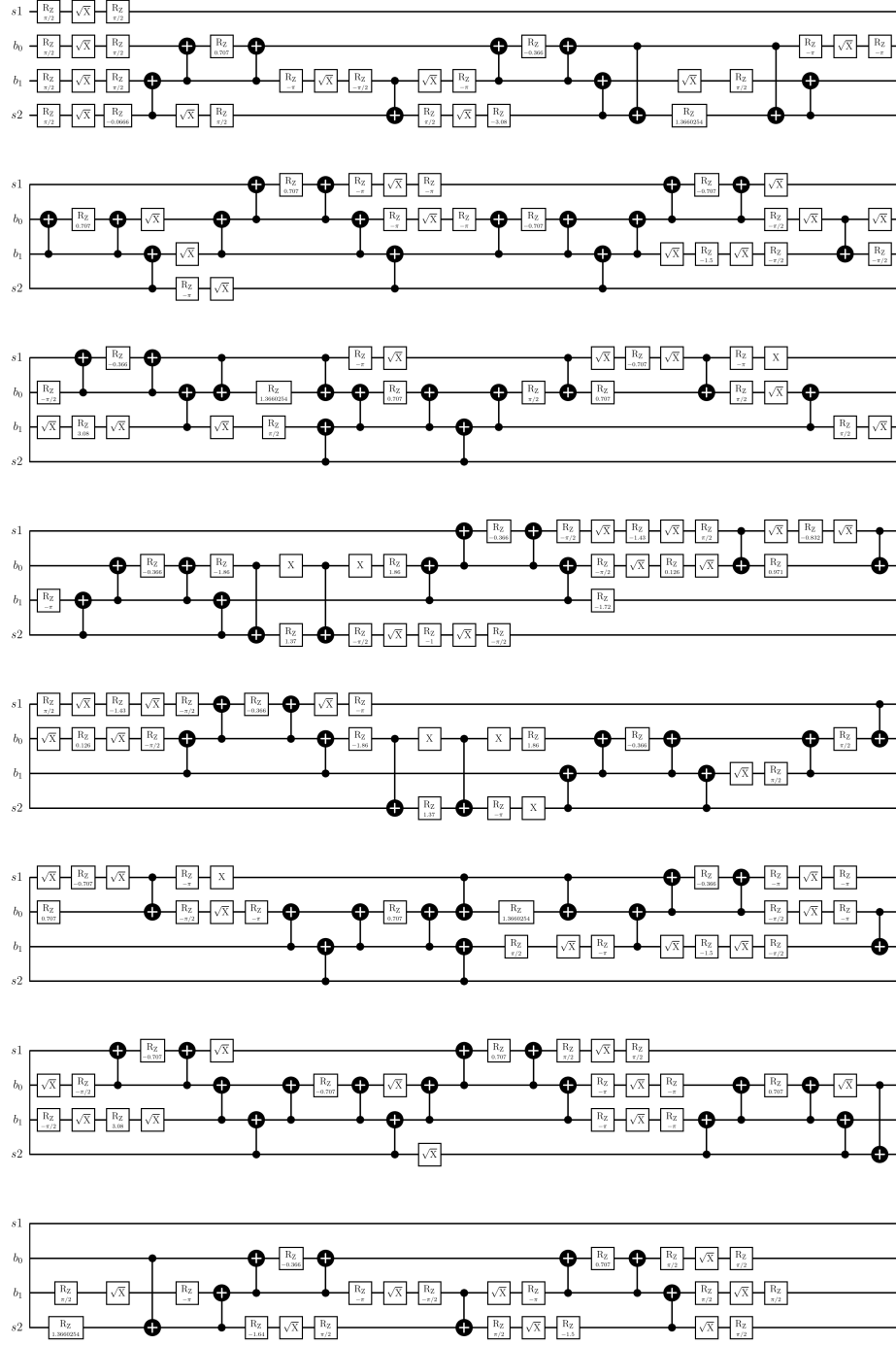[10] S. Paeckel, T. Köhler, A. Swoboda, S. R. Manmana, U. Schollwöck, and C. Hubig, "Time-evolution methods for matrix-product states," *Annals Phys.*, vol. 411, p. 167998, 2019.

[11] I. Georgescu, S. Ashhab, and F. Nori, "Quantum simulation," *Reviews of Modern Physics*, vol. 86, pp. 153–185, Mar. 2014.

[12] J. Koch, T. M. Yu, J. Gambetta, A. A. Houck, D. I. Schuster, J. Majer, A. Blais, M. H. Devoret, S. M. Girvin, and R. J. Schoelkopf, "Charge-insensitive qubit design derived from the cooper pair box," *Physical Review A*, vol. 76, p. 042319, oct 2007.

[13] P. Krantz, M. Kjaergaard, F. Yan, T. P. Orlando, S. Gustavsson, and W. D. Oliver, "A quantum engineer's guide to superconducting qubits," *Applied Physics Reviews*, vol. 6, p. 021318, jun 2019.

[14] H. Liu, G. H. Low, D. S. Steiger, T. Häner, M. Reiher, and M. Troyer, "Prospects of quantum computing for molecular sciences," *Materials Theory*, vol. 6, Mar. 2022.

[15] J. Preskill, "Quantum computing in the NISQ era and beyond," *Quantum*, vol. 2, p. 79, Aug. 2018.

[16] K. Bharti, A. Cervera-Lierta, T. H. Kyaw, T. Haug, S. Alperin-Lea, A. Anand, M. De-groote, H. Heimonen, J. S. Kottmann, T. Menke, W.-K. Mok, S. Sim, L.-C. Kwek, and A. Aspuru-Guzik, "Noisy intermediate-scale quantum algorithms," *Reviews of Modern Physics*, vol. 94, p. 015004, feb 2022.

[17] A. Peruzzo, J. McClean, P. Shadbolt, M.-H. Yung, X.-Q. Zhou, P. J. Love, A. Aspuru-Guzik, and J. L. O'Brien, "A variational eigenvalue solver on a photonic quantum processor," *Nature Communications*, vol. 5, July 2014.

[18] J. R. McClean, J. Romero, R. Babbush, and A. Aspuru-Guzik, "The theory of variational hybrid quantum-classical algorithms," *New Journal of Physics*, vol. 18, p. 023023, Feb. 2016.

[19] J. Romero, R. Babbush, J. R. McClean, C. Hempel, P. J. Love, and A. Aspuru-Guzik, "Strategies for quantum computing molecular energies using the unitary coupled cluster ansatz," *Quantum Science and Technology*, vol. 4, p. 014008, Oct. 2018.

[20] E. Farhi, J. Goldstone, and S. Gutmann, "A quantum approximate optimization algorithm," 2014.

[21] R. Erbanni, K. Bharti, L.-C. Kwek, and D. Poletti, "Nisq algorithm for the matrix elements of a generic observable," 2022.

[22] Y. Li and S. C. Benjamin, "Efficient Variational Quantum Simulator Incorporating Active Error Minimization," *Physical Review X*, vol. 7, p. 021050, June 2017.

[23] K. Temme, S. Bravyi, and J. M. Gambetta, "Error mitigation for short-depth quantum circuits," *Physical Review Letters*, vol. 119, p. 180509, nov 2017.

[24] S. Endo, Z. Cai, S. C. Benjamin, and X. Yuan, "Hybrid quantum-classical algorithms and quantum error mitigation," *Journal of the Physical Society of Japan*, vol. 90, p. 032001, mar 2021.

[25] L. Bittel and M. Kliesch, "Training variational quantum algorithms is np-hard," *Phys. Rev. Lett.*, vol. 127, p. 120502, Sept. 2021.

[26] A. J. Leggett, S. Chakravarty, A. T. Dorsey, M. P. A. Fisher, A. Garg, and W. Zwerger, "Dynamics of the dissipative two-state system," *Reviews of Modern Physics*, vol. 59, pp. 1–85, jan 1987.

[27] Q. Xie, H. Zhong, M. T. Batchelor, and C. Lee, "The quantum rabi model: solution and dynamics," *Journal of Physics A: Mathematical and Theoretical*, vol. 50, p. 113001, feb 2017.

[28] U. Weiss, *Quantum dissipative systems*. WORLD SCIENTIFIC, nov 2011.

[29] D. Xu and K. Schulten, "Coupling of protein motion to electron transfer in a photosynthetic reaction center: investigating the low temperature behavior in the framework of the spin—boson model," *Chemical Physics*, vol. 182, pp. 91–117, may 1994.

[30] T. Renger and R. A. Marcus, "On the relation of protein dynamics and exciton relaxation in pigment–protein complexes: An estimation of the spectral density and a theory for the calculation of optical spectra," *The Journal of Chemical Physics*, vol. 116, pp. 9997–10019, jun 2002.

[31] G. R. Fleming and M. Cho, "Chromophore solvent dynamics," *Annual Review of Physical Chemistry*, vol. 47, pp. 109–134, oct 1996.

[32] J. D. Whitfield, J. Biamonte, and A. Aspuru-Guzik, "Simulation of Electronic Structure Hamiltonians Using Quantum Computers," *Molecular Physics*, vol. 109, pp. 735–750, Mar. 2011.

[33] N. Wiebe, D. W. Berry, P. Høyer, and B. C. Sanders, "Simulating quantum dynamics on a quantum computer," *Journal of Physics A: Mathematical and Theoretical*, vol. 44, p. 445308, oct 2011.

[34] F. Tacchino, A. Chiesa, S. Carretta, and D. Gerace, "Quantum computers as universal quantum simulators: State-of-the-art and perspectives," *Advanced Quantum Technologies*, vol. 3, p. 1900052, dec 2019.

[35] B. Jaderberg, A. Eisfeld, D. Jaksch, and S. Mostame, "Recompilation-enhanced simulation of electron–phonon dynamics on IBM quantum computers," *New Journal of Physics*, vol. 24, p. 093017, sep 2022.

[36] L. Lamata, A. Mezzacapo, J. Casanova, and E. Solano, "Efficient quantum simulation of fermionic and bosonic models in trapped ions," *EPJ Quantum Technology*, vol. 1, pp. 1–13, Dec. 2014.

[37] S. Maniscalco, J. Piilo, F. Intravaia, F. Petruccione, and A. Messina, "Simulating quantum Brownian motion with single trapped ions," *Physical Review A*, vol. 69, p. 052101, May 2004.

[38] C. J. Myatt, B. E. King, Q. A. Turchette, C. A. Sackett, D. Kielpinski, W. M. Itano, C. Monroe, and D. J. Wineland, "Decoherence of quantum superpositions through coupling to engineered reservoirs," *Nature*, vol. 403, pp. 269–273, Jan. 2000.

[39] J. T. Barreiro, M. Müller, P. Schindler, D. Nigg, T. Monz, M. Chwalla, M. Hennrich, C. F. Roos, P. Zoller, and R. Blatt, "An Open-System Quantum Simulator with Trapped Ions," *Nature*, vol. 470, pp. 486–491, Feb. 2011.

[40] P. Schindler, M. Müller, D. Nigg, J. T. Barreiro, E. A. Martinez, M. Hennrich, T. Monz, S. Diehl, P. Zoller, and R. Blatt, "Quantum simulation of dynamical maps with trapped ions," *Nature Physics*, vol. 9, pp. 361–367, June 2013.

[41] S. Mostame, P. Rebentrost, A. Eisfeld, A. J. Kerman, D. I. Tsomokos, and A. Aspuru-Guzik, "Quantum simulator of an open quantum system using superconducting qubits: exciton transport in photosynthetic complexes," *New Journal of Physics*, vol. 14, p. 105013, Oct. 2012.

[42] T. Xin, S.-J. Wei, J. S. Pedernales, E. Solano, and G.-L. Long, "Quantum simulation of quantum channels in nuclear magnetic resonance," *Physical Review A*, vol. 96, p. 062303, Dec. 2017.

[43] H. Lu, C. Liu, D.-S. Wang, L.-K. Chen, Z.-D. Li, X.-C. Yao, L. Li, N.-L. Liu, C.-Z. Peng, B. C. Sanders, Y.-A. Chen, and J.-W. Pan, "Experimental quantum channel simulation," *Physical Review A*, vol. 95, p. 042310, Apr. 2017.

[44] A. Cuevas, A. Geraldi, C. Liorni, L. D. Bonavena, A. De Pasquale, F. Sciarrino, V. Giovannetti, and P. Mataloni, "All-optical implementation of collision-based evolutions of open quantum systems," *Scientific Reports*, vol. 9, p. 3205, Mar. 2019.

[45] A. Di Paolo, P. K. Barkoutsos, I. Tavernelli, and A. Blais, "Variational Quantum Simulation of Ultrastrong Light-Matter Coupling," *Physical Review Research*, vol. 2, p. 033364, Sept. 2020.

[46] A. Miessen, P. J. Ollitrault, and I. Tavernelli, "Quantum algorithms for quantum dynamics: A performance study on the spin-boson model," *Physical Review Research*, vol. 3, p. 043212, Dec. 2021.

[47] N. Fitzpatrick, H. Apel, and D. M. Ramo, "Evaluating low-depth quantum algorithms for time evolution on fermion-boson systems," 2021.

[48] H. Kamakari, S.-N. Sun, M. Motta, and A. J. Minnich, "Digital quantum simulation of open quantum systems using quantum imaginary time evolution," *PRX Quantum*, vol. 3, p. 010320, Feb. 2022.

[49] S. McArdle, T. Jones, S. Endo, Y. Li, S. C. Benjamin, and X. Yuan, "Variational ansatz-based quantum simulation of imaginary time evolution," *npj Quantum Information*, vol. 5, pp. 1–6, Sept. 2019.

[50] S. Endo, J. Sun, Y. Li, S. Benjamin, and X. Yuan, "Variational quantum simulation of general processes," *Physical Review Letters*, vol. 125, p. 010501, June 2020.

[51] N. Yoshioka, Y. O. Nakagawa, K. Mitarai, and K. Fujii, "Variational quantum algorithm for nonequilibrium steady states," *Phys. Rev. Research*, vol. 2, p. 043289, Nov. 2020.

[52] H.-Y. Liu, T.-P. Sun, Y.-C. Wu, and G.-P. Guo, "Variational Quantum Algorithms for the Steady States of Open Quantum Systems," *Chinese Physics Letters*, vol. 38, p. 080301, Sept. 2021.

[53] K. Bharti and T. Haug, "Quantum-assisted simulator," *Phys. Rev. A*, vol. 104, p. 042418, Oct 2021.

[54] Z. Hu, R. Xia, and S. Kais, "A quantum algorithm for evolving open quantum dynamics on quantum computing devices," *Scientific Reports*, vol. 10, p. 3301, Dec. 2020.

[55] A. W. Schlimgen, K. Head-Marsden, L. M. Sager, P. Narang, and D. A. Mazziotti, "Quantum Simulation of Open Quantum Systems Using a Unitary Decomposition of Operators," *Physical Review Letters*, vol. 127, p. 270503, Dec. 2021.

[56] P. Udayakumar and P. Kumar-Eslami, "Kraus operator formalism for quantum multiplexer operations for arbitrary two-qubit mixed states," *Quantum Information Processing*, vol. 18, p. 361, Oct. 2019.

[57] M. A. Nielsen and I. L. Chuang, "Quantum Computation and Quantum Information: 10th Anniversary Edition," Dec. 2010.

[58] G. García-Pérez, M. A. C. Rossi, and S. Maniscalco, "IBM Q Experience as a versatile experimental testbed for simulating open quantum systems," *npj Quantum Information*, vol. 6, pp. 1–10, Jan. 2020.

[59] S.-J. Wei, D. Ruan, and G.-L. Long, "Duality quantum algorithm efficiently simulates open quantum systems," *Scientific Reports*, vol. 6, p. 30727, July 2016.

[60] R. Cleve and C. Wang, "Efficient quantum algorithms for simulating lindblad evolution," *arXiv:1612.09512*, 2016.

[61] M. Jo and M. Kim, "Simulating open quantum many-body systems using optimised circuits in digital quantum simulation," *arXiv:2203.14295*, 2022.

[62] M. G. Algaba, M. Ponce-Martinez, C. Munuera-Javaloy, V. Pina-Canelles, M. Thapa, B. G. Taketani, M. Leib, I. de Vega, J. Casanova, and H. Heimonen, "Co-design quantum simulation of nanoscale nmr," 2022.

[63] A. Burger, L. C. Kwek, and D. Poletti, "Digital quantum simulation of the spin-boson model under open system dynamics," 2022.

[64] I. I. Rabi, "On the process of space quantization," *Physical Review*, vol. 49, pp. 324–328, feb 1936.

[65] I. I. Rabi, "Space quantization in a gyrating magnetic field," *Physical Review*, vol. 51, pp. 652–654, apr 1937.

[66] F. Bloch and A. Siegert, "Magnetic resonance for nonrotating fields," *Physical Review*, vol. 57, pp. 522–527, mar 1940.

[67] E. Jaynes and F. Cummings, "Comparison of quantum and semiclassical radiation theories with application to the beam maser," *Proceedings of the IEEE*, vol. 51, no. 1, pp. 89–109, 1963.

[68] F. W. Cummings, "Reminiscing about thesis work with E T Jaynes at Stanford in the 1950s," *Journal of Physics B: Atomic, Molecular and Optical Physics*, vol. 46, p. 220202, nov 2013.

[69] L. Garziano, A. Ridolfo, S. De Liberato, and S. Savasta, "Cavity qed beyond rotating wave approximation: Photon bunching from the emission of individual qubits," 2017.

[70] P. Forn-Díaz, J. Lisenfeld, D. Marcos, J. J. García-Ripoll, E. Solano, C. J. P. M. Harmans, and J. E. Mooij, "Observation of the bloch-siegert shift in a qubit-oscillator system in the ultrastrong coupling regime," *Physical Review Letters*, vol. 105, p. 237001, nov 2010.

[71] T. Niemczyk, F. Deppe, H. Huebl, E. P. Menzel, F. Hocke, M. J. Schwarz, J. J. Garcia-Ripoll, D. Zueco, T. Hümmer, E. Solano, A. Marx, and R. Gross, "Circuit quantum electrodynamics in the ultrastrong-coupling regime," *Nature Physics*, vol. 6, pp. 772–776, jul 2010.

[72] J. Braumüller, M. Marthaler, A. Schneider, A. Stehli, H. Rotzinger, M. Weides, and A. V. Ustinov, "Analog quantum simulation of the rabi model in the ultra-strong coupling regime," *Nature Communications*, vol. 8, oct 2017.

[73] P. Forn-Díaz, J. J. García-Ripoll, B. Peropadre, J.-L. Orgiazzi, M. A. Yurtalan, R. Belyansky, C. M. Wilson, and A. Lupascu, "Ultrastrong coupling of a single artificial atom to an electromagnetic continuum in the nonperturbative regime," *Nature Physics*, vol. 13, pp. 39–43, oct 2016.

[74] F. Yoshihara, T. Fuse, S. Ashhab, K. Kakuyanagi, S. Saito, and K. Semba, "Superconducting qubit–oscillator circuit beyond the ultrastrong-coupling regime," *Nature Physics*, vol. 13, pp. 44–47, oct 2016.

[75] N. K. Langford, R. Sagastizabal, M. Kounalakis, C. Dickel, A. Bruno, F. Luthi, D. J. Thoen, A. Endo, and L. DiCarlo, "Experimentally simulating the dynamics of quantum light and matter at deep-strong coupling," *Nature Communications*, vol. 8, nov 2017.

[76] D. Lv, S. An, Z. Liu, J.-N. Zhang, J. S. Pedernales, L. Lamata, E. Solano, and K. Kim, "Quantum simulation of the quantum rabi model in a trapped ion," *Physical Review X*, vol. 8, p. 021027, apr 2018.

[77] A. Crespi, S. Longhi, and R. Osellame, "Photonic realization of the quantum rabi model," *Physical Review Letters*, vol. 108, p. 163601, apr 2012.

[78] Y. Todorov, A. M. Andrews, I. Sagnes, R. Colombelli, P. Klang, G. Strasser, and C. Sirtori, "Strong light-matter coupling in subwavelength metal-dielectric microcavities at terahertz frequencies," *Physical Review Letters*, vol. 102, p. 186402, may 2009.

[79] G. Günter, A. A. Anappara, J. Hees, A. Sell, G. Biasiol, L. Sorba, S. D. Liberato, C. Ciuti, A. Tredicucci, A. Leitenstorfer, and R. Huber, "Sub-cycle switch-on of ultrastrong light–matter interaction," *Nature*, vol. 458, pp. 178–181, mar 2009.

[80] G. Lindblad, "On the generators of quantum dynamical semigroups," *Communications in Mathematical Physics*, vol. 48, pp. 119–130, June 1976.

[81] V. Gorini, "Completely positive dynamical semigroups of n-level systems," *Journal of Mathematical Physics*, vol. 17, no. 5, p. 821, 1976.

[82] H. Ritsch, P. Domokos, F. Brennecke, and T. Esslinger, "Cold atoms in cavity-generated dynamical optical potentials," *Reviews of Modern Physics*, vol. 85, pp. 553–601, apr 2013.

[83] A. Reiserer and G. Rempe, "Cavity-based quantum networks with single atoms and optical photons," *Reviews of Modern Physics*, vol. 87, pp. 1379–1418, dec 2015.

[84] C. Fabre, V. Sandoghdar, N. Treps, and L. F. Cugliandolo, eds., *Quantum Optics and Nanophotonics*. Oxford University PressOxford, may 2017.

[85] F. Ciccarello, S. Lorenzo, V. Giovannetti, and G. M. Palma, "Quantum collision models: open system dynamics from repeated interactions," *Physics Reports*, vol. 954, pp. 1–70, Apr. 2022.

[86] D. Karevski and T. Platini, "Quantum nonequilibrium steady states induced by repeated interactions," *Physical Review Letters*, vol. 102, p. 207207, may 2009.

[87] S. B. Bravyi and A. Y. Kitaev, "Fermionic Quantum Computation," *Annals of Physics*, vol. 298, pp. 210–226, May 2002.

[88] L. Clinton, J. Bausch, and T. Cubitt, "Hamiltonian simulation algorithms for near-term quantum hardware," *Nature Communications*, vol. 12, aug 2021.

[89] M. Chiew and S. Strelchuk, "Optimal fermion-qubit mappings," 2021.

[90] R. D. Somma, G. Ortiz, E. H. Knill, and J. Gubernatis, "Quantum simulations of physics problems," in *Quantum Information and Computation*, vol. 5105, pp. 96–103, SPIE, Aug. 2003.

[91] C. D. Batista and G. Ortiz, "Algebraic approach to interacting quantum systems," *Advances in Physics*, vol. 53, pp. 1–82, Jan. 2004.

[92] L.-A. Wu and D. A. Lidar, "Qubits as parafermions," *Journal of Mathematical Physics*, vol. 43, pp. 4506–4525, Sept. 2002.

[93] A. Macridin, P. Spentzouris, J. Amundson, and R. Harnik, "Digital quantum computation of fermion-boson interacting systems," *Physical Review A*, vol. 98, p. 042312, Oct. 2018.

[94] O. Di Matteo, A. McCoy, P. Gysbers, T. Miyagi, R. M. Woloshyn, and P. Navrátil, "Improving Hamiltonian encodings with the Gray code," *Physical Review A*, vol. 103, p. 042405, Apr. 2021.

[95] N. P. D. Sawaya, T. Menke, T. H. Kyaw, S. Johri, A. Aspuru-Guzik, and G. G. Guerreschi, "Resource-efficient digital quantum simulation of d-level systems for photonic, vibrational, and spin-s Hamiltonians," *npj Quantum Information*, vol. 6, p. 49, Dec. 2020.

[96] N. Hatano and M. Suzuki, "Finding exponential product formulas of higher orders," in *Quantum Annealing and Other Optimization Methods*, pp. 37–68, Springer Berlin Heidelberg, nov 2005.

[97] D. W. Berry, G. Ahokas, R. Cleve, and B. C. Sanders, "Efficient quantum algorithms for simulating sparse hamiltonians," *Communications in Mathematical Physics*, vol. 270, pp. 359–371, dec 2006.

[98] G. A. et al., "Qiskit: An open-source framework for quantum computing," 2021.

[99] B. Drury and P. Love, "Constructive quantum shannon decomposition from cartan involutions," *Journal of Physics A: Mathematical and Theoretical*, vol. 41, p. 395305, sep 2008.

[100] R. Iten, R. Colbeck, I. Kukuljan, J. Home, and M. Christandl, "Quantum Circuits for Isometries," *Physical Review A*, vol. 93, p. 032318, Mar. 2016.

[101] E. Knill, "Approximation by Quantum Circuits," Aug. 1995.

[102] R. Iten, O. Reardon-Smith, E. Malvetti, L. Mondada, G. Pauvert, E. Redmond, R. S. Kohli, and R. Colbeck, "Introduction to universalqcompiler," 2019.

[103] E. Campbell, "Random compiler for fast hamiltonian simulation," *Physical Review Letters*, vol. 123, p. 070503, aug 2019.

[104] M. Hagan and N. Wiebe, "Composite quantum simulations," 2022.

[105] D. W. Berry, A. M. Childs, R. Cleve, R. Kothari, and R. D. Somma, "Simulating hamiltonian dynamics with a truncated taylor series," *Physical Review Letters*, vol. 114, p. 090502, mar 2015.

[106] A. M. Childs, D. Maslov, Y. Nam, N. J. Ross, and Y. Su, "Toward the first quantum simulation with quantum speedup," *Proceedings of the National Academy of Sciences*, vol. 115, pp. 9456–9461, sep 2018.

[107] G. H. Low and I. L. Chuang, "Hamiltonian Simulation by Qubitization," *Quantum*, vol. 3, p. 163, July 2019.

[108] T. F. Mörstedt, A. Viitanen, V. Vadimov, V. Sevriuk, M. Partanen, E. Hyyppä, G. Catelani, M. Silveri, K. Y. Tan, and M. Möttönen, "Recent developments in quantum-circuit refrigeration," *Annalen der Physik*, vol. 534, p. 2100543, may 2022.

[109] K. Y. Tan, M. Partanen, R. E. Lake, J. Govenius, S. Masuda, and M. Möttönen, "Quantum-circuit refrigerator," *Nature Communications*, vol. 8, may 2017.

[110] A. J., A. Adedoyin, J. Ambrosiano, P. Anisimov, W. Casper, G. Chennupati, C. Coffrin, H. Djidjev, D. Gunter, S. Karra, N. Lemons, S. Lin, A. Malyzhenkov, D. Mascarenas, S. Mniszewski, B. Nadiga, D. O'Malley, D. Oyen, S. Pakin, L. Prasad, R. Roberts, P. Romero, N. Santhi, N. Sinitsyn, P. J. Swart, J. G. Wendelberger,

B. Yoon, R. Zamora, W. Zhu, S. Eidenbenz, A. Bärtschi, P. J. Coles, M. Vuffray, and A. Y. Lokhov, "Quantum algorithm implementations for beginners," *ACM Transactions on Quantum Computing*, 2018.

[111] J. Johansson, P. Nation, and F. Nori, "QuTiP 2: A python framework for the dynamics of open quantum systems," *Computer Physics Communications*, vol. 184, pp. 1234–1240, Apr. 2013.

[112] R. Jozsa, "Fidelity for mixed quantum states," *Journal of Modern Optics*, vol. 41, pp. 2315–2323, dec 1994.

[113] H. D. Ursell, "The evaluation of gibbs' phase-integral for imperfect gases," *Mathematical Proceedings of the Cambridge Philosophical Society*, vol. 23, pp. 685–697, apr 1927.

[114] J. K. Percus, "Correlation inequalities for ising spin lattices," *Communications in Mathematical Physics*, vol. 40, pp. 283–308, oct 1975.

[115] S. B. Shlosman, "Signs of the ising model ursell functions," *Communications in Mathematical Physics*, vol. 102, pp. 679–686, dec 1986.

[116] S. Krinner, N. Lacroix, A. Remm, A. D. Paolo, E. Genois, C. Leroux, C. Hellings, S. Lazar, F. Swiadek, J. Herrmann, G. J. Norris, C. K. Andersen, M. Müller, A. Blais, C. Eichler, and A. Wallraff, "Realizing repeated quantum error correction in a distance-three surface code," *Nature*, vol. 605, pp. 669–674, may 2022.

[117] R. e. a. Acharya, "Suppressing quantum errors by scaling a surface code logical qubit," 2022.

[118] N. Sundaresan, T. J. Yoder, Y. Kim, M. Li, E. H. Chen, G. Harper, T. Thorbeck, A. W. Cross, A. D. Córcoles, and M. Takita, "Matching and maximum likelihood decoding of a multi-round subsystem quantum error correction experiment," 2022.

[119] S. Bravyi, S. Sheldon, A. Kandala, D. C. Mckay, and J. M. Gambetta, "Mitigating measurement errors in multiqubit experiments," *Physical Review A*, vol. 103, p. 042605, Apr. 2021.

[120] E. van den Berg, Z. K. Minev, and K. Temme, "Model-free readout-error mitigation for quantum expectation values," *Physical Review A*, vol. 105, p. 032620, mar 2022.

[121] A. Kandala, K. Temme, A. D. Córcoles, A. Mezzacapo, J. M. Chow, and J. M. Gambetta, "Error mitigation extends the computational reach of a noisy quantum processor," *Nature*, vol. 567, pp. 491–495, mar 2019.

[122] B. Jaderberg, A. Agarwal, K. Leonhardt, M. Kiffner, and D. Jaksch, "Minimum hardware requirements for hybrid quantum–classical DMFT," *Quantum Science and Technology*, vol. 5, p. 034015, jun 2020.

[123] M. Ostaszewski, E. Grant, and M. Benedetti, "Structure optimization for parameterized quantum circuits," *Quantum*, vol. 5, p. 391, Jan. 2021.

[124] T. Jones and S. C. Benjamin, "Robust quantum compilation and circuit optimisation via energy minimisation," *Quantum*, vol. 6, p. 628, jan 2022.

[125] S. Khatri, R. LaRose, A. Poremba, L. Cincio, A. T. Sornborger, and P. J. Coles, "Quantum-assisted quantum compiling," *Quantum*, vol. 3, p. 140, may 2019.

[126] P. Czarnik, A. Arrasmith, P. J. Coles, and L. Cincio, "Error mitigation with clifford quantum-circuit data," *Quantum*, vol. 5, p. 592, nov 2021.

[127] J. Sun, X. Yuan, T. Tsunoda, V. Vedral, S. C. Benjamin, and S. Endo, "Mitigating realistic noise in practical noisy intermediate-scale quantum devices," *Physical Review Applied*, vol. 15, p. 034026, mar 2021.

[128] S. Zhang, Y. Lu, K. Zhang, W. Chen, Y. Li, J.-N. Zhang, and K. Kim, "Error-mitigated quantum gates exceeding physical fidelities in a trapped-ion system," *Nature Communications*, vol. 11, jan 2020.

[129] K. Georgopoulos, C. Emary, and P. Zuliani, "Modeling and simulating the noisy behavior of near-term quantum computers," *Physical Review A*, vol. 104, p. 062432, dec 2021.

[130] IBM, "Qiskit dokumentation," 2022.

[131] IBM, "Ibmq devices," 2022.

[132] G. T. Landi, "Quantum information and quantum noise." University of Sao Paulo, July 2018.

[133] M.-D. Choi, "Completely positive linear maps on complex matrices," *Linear Algebra and its Applications*, vol. 10, pp. 285–290, jun 1975.

[134] D. M. Tong, L. C. Kwek, C. H. Oh, J.-L. Chen, and L. Ma, "Operator-sum representation of time-dependent density operators and its applications," *Physical Review A*, vol. 69, p. 054102, may 2004.

[135] H. Nakazato, Y. Hida, K. Yuasa, B. Militello, A. Napoli, and A. Messina, "Solution of the Lindblad Equation in the Kraus Representation," *Physical Review A*, vol. 74, p. 062113, Dec. 2006.

[136] A. Fujiwara, "Estimation of a generalized amplitude-damping channel," *Physical Review A*, vol. 70, p. 012317, jul 2004.

[137] W. F. Stinespring, "Positive functions on c ∗ -algebras," *Proceedings of the American Mathematical Society*, vol. 6, p. 211, apr 1955.

[138] D.-S. Wang, D. W. Berry, M. C. de Oliveira, and B. C. Sanders, "Solovay-Kitaev Decomposition Strategy for Single-Qubit Channels," *Physical Review Letters*, vol. 111, p. 130504, Sept. 2013.

[139] D. C. McKay, C. J. Wood, S. Sheldon, J. M. Chow, and J. M. Gambetta, "Efficient z-gates for quantum computing," *Physical Review A*, vol. 96, p. 022330, aug 2017.

[140] D. Poulin, A. Kitaev, D. S. Steiger, M. B. Hastings, and M. Troyer, "Quantum algorithm for spectral measurement with a lower gate count," *Physical Review Letters*, vol. 121, p. 010501, jul 2018.

[141] M. Steudtner and S. Wehner, "Estimating exact energies in quantum simulation without Toffoli gates," *Physical Review A*, vol. 101, p. 052329, may 2020.

[142] S. Ramos-Calderer, A. Pérez-Salinas, D. García-Martín, C. Bravo-Prieto, J. Cortada, J. Planagumà, and J. I. Latorre, "Quantum unary approach to option pricing," *Physical Review A*, vol. 103, p. 032414, mar 2021.

104

[143] R. Miller, T. E. Northup, K. M. Birnbaum, A. Boca, A. D. Boozer, and H. J. Kimble, "Trapped atoms in cavity QED: coupling quantized light and matter," *Journal of Physics B: Atomic, Molecular and Optical Physics*, vol. 38, pp. S551–S565, apr 2005.

[144] H. Walther, B. T. H. Varcoe, B.-G. Englert, and T. Becker, "Cavity quantum electrodynamics," *Reports on Progress in Physics*, vol. 69, pp. 1325–1382, apr 2006.

[145] J. M. Raimond, M. Brune, and S. Haroche, "Manipulating quantum entanglement with atoms and photons in a cavity," *Reviews of Modern Physics*, vol. 73, pp. 565–582, aug 2001.

[146] D. Leibfried, R. Blatt, C. Monroe, and D. Wineland, "Quantum dynamics of single trapped ions," *Reviews of Modern Physics*, vol. 75, pp. 281–324, mar 2003.

[147] J. S. Pedernales, I. Lizuain, S. Felicetti, G. Romero, L. Lamata, and E. Solano, "Quantum rabi model with trapped ions," *Scientific Reports*, vol. 5, oct 2015.

[148] R. Hanson, L. P. Kouwenhoven, J. R. Petta, S. Tarucha, and L. M. K. Vandersypen, "Spins in few-electron quantum dots," *Reviews of Modern Physics*, vol. 79, pp. 1217–1265, oct 2007.

[149] A. Wallraff, D. I. Schuster, A. Blais, L. Frunzio, R.-S. Huang, J. Majer, S. Kumar, S. M. Girvin, and R. J. Schoelkopf, "Strong coupling of a single photon to a superconducting qubit using circuit quantum electrodynamics," *Nature*, vol. 431, pp. 162–167, sep 2004.

[150] M. H. Devoret and R. J. Schoelkopf, "Superconducting circuits for quantum information: An outlook," *Science*, vol. 339, pp. 1169–1174, mar 2013.

Declaration of Authorship

I hereby confirm, that I wrote this Master Thesis un-
aided and that all the sources and resources I used are
the ones stated above.

Singapore, November 30th, 2022

. . . .
Andreas Burger